Universitat Autònoma de Barcelona

Managing light in optoelectronic devices with resonant optical nanostructures

Pau Molet Bachs

Managing light in optoelectronic devices with resonant optical nanostructures

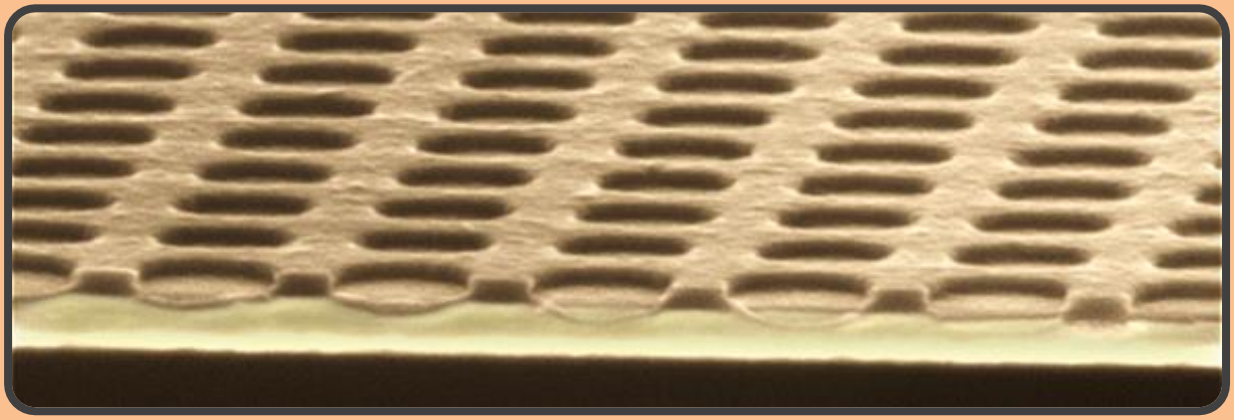

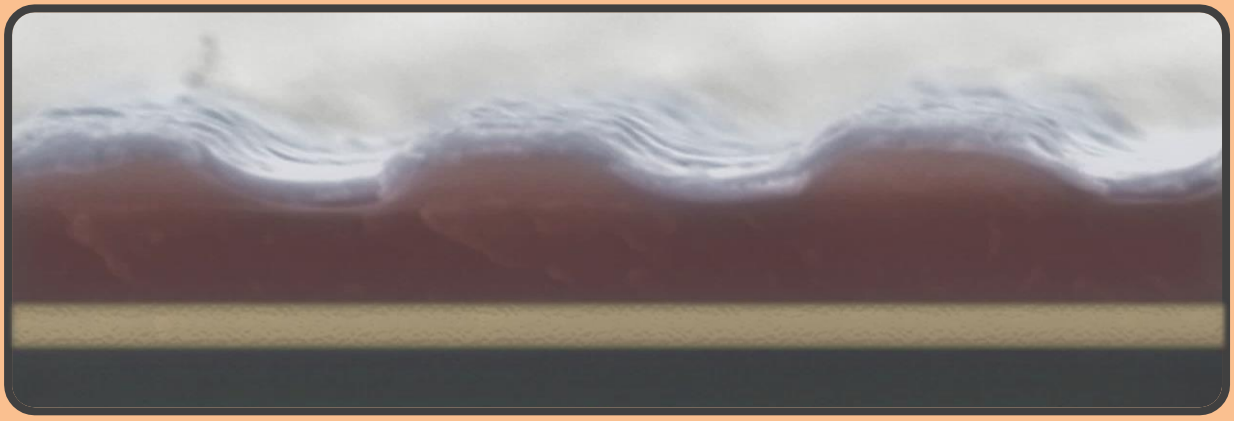

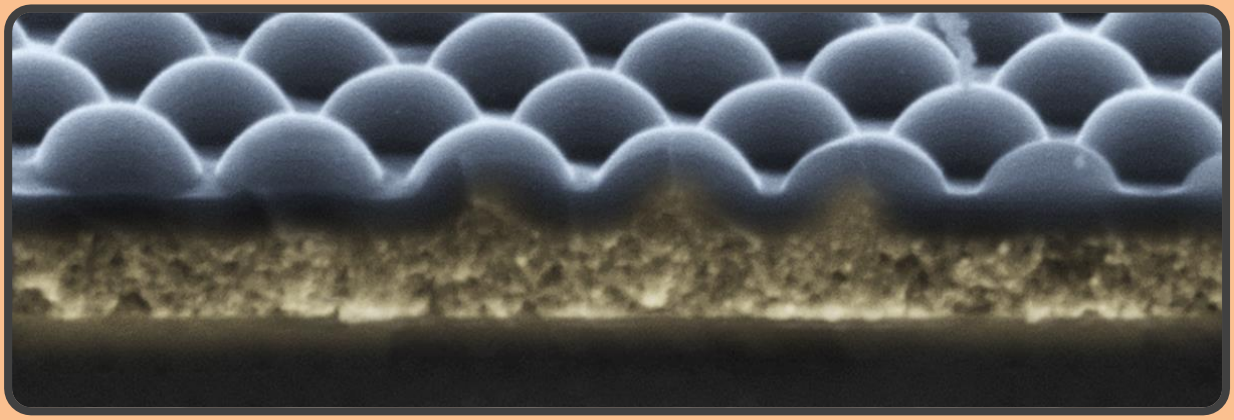

Pau Molet

UAB
Universitat Autònoma de Barcelona

ICMAB

Universitat Autònoma de Barcelona

Thesis submitted for the Doctoral Degree from

UNIVERSITAT AUTÒNOMA DE BARCELONA

PhD Program in Materials Science

Managing light in optoelectronic devices with resonant optical nanostructures

Pau Molet Bachs

Under the supervision of:

Agustín Mihi (Director) **Mariano Campoy-Quiles (Tutor)**

Institut de Ciència de Materials de Barcelona

(ICMAB-CSIC)

2021

ICMAB

CSIC
CONSEJO SUPERIOR DE INVESTIGACIONES CIENTÍFICAS

Table of contents

List of abbreviations

a-Ge - Amorphous germanium

AFM - Atomic force microscopy

AL - Active layer

ARC - Antireflection coating

CVD - Chemical vapour deposition

BHJ - Bulk heterojunction

CMOS - Complementary metal oxide semiconductor

CQD - Colloidal quantum dots

CTS - Charge transfer state

ED - Electric dipole

EDT- 1,2-Ethanedithiol

EM - Electromagnetic

EQE - External quantum efficiency

ETL - Electron transport layer

FDTD - Finite domain time difference

FF - Filling factor

FPC - Fabry-Perot cavity

FPR - Fabry-Perot resonance

FTIR - Fourier transform infrared spectroscopy

FWHM - Full-width half-maximum

GaAs- Gallium arsenide

$GdVO_4$ - Gadolinium vanadate

GM - Guided modes

HOMO - Highest occupied molecular orbital

hPDMS - Hard PDMS

InGaAs - Indium gallium arsenide

ITO - Indium tin oxide

IQE - Internal quantum efficiency

J_{sc} - Short circuit current

L - Lattice parameter

LBIC - Light beam induced photocurrent

LDOS - Local density of optical states

LED - Light emitting diode

LUMO - Lowest unoccupied molecular orbital

MBE - Molecular beam epitaxy

MD - Magnetic dipole

MoO_3 - Molybdenum trioxide

m-TiO_2 – Mesoporous titania

NIL - Nanoimprint lithography

NIR - Near infrared

OPDs - Organic photodetectors

PBDTTT-E-T - Copolymer of benzo[1,2-b:4,5-b']dithio-phene (BDT) and thieno[3,4-b]thiophene (TT)

PBTTT - Poly[2,5-bis(3-tetradecylthiophen-2-yl)thieno[3,2-b]thiophene]

PbS - Lead sulfide

$PC_{60}BM$ - Phenyl-C61-butyric acid methyl ester

$PC_{70}BM$ - Phenyl C71 butyric acid methyl ester

PCE - Power conversion efficiency

PDMS - Polydimethylsiloxane

PEC - Perfect electric conductor

PET - Polyethylene terephtalate

PhC - Photonic crystal

P3HT - Poly(3-hexylthiophene-2,5-diyl)

PL - Photoluminescence

PLQY - Photoluminescence quantum yield

PV - Photovoltaic

QGM - Quasi-guided modes

RAs - Rayleigh-Wood's anomalies

RE - Rare-earth

RHEED - Reflection high-energy electron diffraction

RIE - Reactive ion etching

RWG - Resonant waveguide gratings

SCLC - Space charge limited current

SEM - Scanning electron microscopy

SERS - Surface enhanced Raman spectroscopy

sNIL - Solvent assisted nanoimprinting lithography

sPDMS - Soft PDMS

SPP - Surface plasmon polaritons

TE – Transversal electric

TEM - Transmission electron microscopy

TiO_2- Titanium dioxide, titania

TM – Transversal magnetic

tNIL - Thermal nanoimprinting lithography

TRTC- Two resonance tapping cavity

UV – Ultraviolet

UV-NIL - Ultraviolet assisted nanoimprinting lithography

VIS – Visible light

V_{oc} – Open circuit voltage

Abstract

One of the main challenges in light management at the nanoscale is the transition from the laboratory to real applications. Despite the great potential shown by photonic architectures to optically improve the performance of many devices, transitioning into marketable devices is often hampered by the low-throughput and expensive nanofabrication techniques involved. This thesis is devoted to the design and development of subwavelength light managing strategies to improve light harvesting or out-coupling in solar cells, photodetectors and light emitters while using scalable nanostructuration methodologies such as soft nanoimprint lithography (NIL). This technique has been proven to achieve resolutions down to few tens of nanometers with high fidelity in large areas, being compatible with roll-to-roll processing. It is also versatile regarding the materials where it can be used, non-invasive, and can be seamlessly introduced in the devices fabrication scheme. With the aid of this technique, we explore a variety of photonic architectures and the different types of resonances sustained, from Brewster modes to Mie resonances, in order to enhance the light-matter interaction with the active layer of the device.

First, we develop a strategy to achieve broadband optimal absorption in ultra-thin semiconductor materials (less than 100 nm thick) for all energies above their bandgap. The interplay of strong interference thin film resonances and photonic crystal modes sustained by a high refractive index nanostructure on a gold film renders the system with a 81% total absorption over a broad spectral range (from 400 to 1500 nm).

Second, we combine soft NIL and chemical vapor deposition to obtain an array of silicon hemispheres on top of a high refractive index dielectric waveguide. We study the Mie resonances supported by the substrate, how these hybridize with the guided modes of the waveguide and how their interaction influences the electromagnetic near field of the metasurface. We further explore the tunability of such resonances with the design parameters of the structure and we demonstrate a potential application of it as a substrate for enhanced photoluminescence.

In the third part of the thesis, we focus on the implementation of 2D photonic structures within the active layer of three different devices to improve performance. In particular we enhance the near infrared (NIR) photon harvesting efficiency in a ***colloidal quantum dot solar cell*** *(PbS-CQD)* and in ***organic photodetectors*** *(P3HT: $PC_{60}BM$ and PBTTT: $PC_{70}BM$)* and improve the light out coupling from a ***nanophosphor layer*** *($GdVO_4:Eu^{3+}$ nanocrystals)*. We developed photonic systems tailored for each device and provided the complete optical and electronic

characterization for each case. The nanostructuration with a 2D periodic arrangement renders the active layers with resonant waveguide properties enhancing its light trapping properties in the targeted spectral ranges, hence demonstrating the possibility to implement photonic schemes within actual devices.

Agraïments

En primer lloc, vull agrair aquest treball al meu director de tesi Agustín Mihi. Espero que per molts alumnes que tinguis en el futur sempre els puguis transmetre les energies, les ganes i el interès per fer ciència que m'has transmès a mi. Gracies per cuidar de mi i sempre pensar en el millor pel meu futur.

En segon lloc, els meus més sincers agraïments i admiració pel Dr. Juan Luis Garcia-Pomar, que ha estat com un segon tutor durant bona part de la tesi. I que d'important és tenir un bon teòric al grup. Gràcies per a ser pacient in no enviar-me a pastar fang amb tots els meus dubtes, incloses les vegades que "te vendía". La ciència necessita més gent com tu.

També és necessari agrair a tots els companys de laboratori que aquesta etapa doctoral hagi estat una joia "TOP Class!" Especialment al pesao del Martí. Espero que la vida ens permeti fer molt més recorregut junts. També gracies per haver-me fet famós allà on anaves, espero que algun dia el "Putu Pau" arribi a ser *trending tópic*. A la mafia italiana de la Camila i el Cristiano per alegrar la vida a l'oficina i en els molts viatges. Que mai se us acabi la vitalitat i les ganes de gaudir de la vida. A la Mayte, per acceptar sempre amb un somriure els meus diners, les meves bromes pesades i els meus projectils d'alumini. A l'Osnat, per ser el meu *sensei* en escalada i el nostre guia mexicano. Al Leonardo, que tot i haver arribat el darrer, potser m'ha ensenyat més coses que tota la resta. Al Quique, per ser el més *salao* del grup, i en conjunt amb l'Adrián, haver-me suportat en els meus primers partits de pàdel. Aixímateix al Miquel Casademont, perquè malgrat mai guanyem un partit, no has perdut la confiança en mi. També es mereix una menció especial la teva dedicació per a fer porta-substrats a mida per a les meves necessitats, gràcies. Gràcies al Luis Pérez, per ser el meu fan n°1, que sàpigues que jo sóc el teu fan n°1 també, espero que les teves brillants idees i la manera que tens de veure la ciència et portin una ERC en breus. Al, Jose Jurado, per ser el més yanki del grup, i al Jose Mendoza per compartir els dinarets al solete. Al Nico per resoldre'm els dubtes teòrics durant aquest últim any, presencial i telemàticament. Al David Vila, gràcies per haver intentat, i aconseguit durant un temps, ser el meu *gym buddy*. Gràcies també als sèniors del grup, l'Alejandro, el Mariano, el Sebas, el Pablo Vaccaro i el Miquel Garriga per haver-me ajudat i aconsellat en molts moments de la tesi, amb especial menció a la Isabel per haver-me introduït al grup, ara ja farà sis o set anys ben bons. Gràcies a tota la resta d'Oompa Loompas del grup de Nanopto per haver compartit amb mi aquests anys de tesi, amb especial dedicatòria al papà Oompa Loompa Dr. Bernhard Dorling, per

que sense tu el laboratori seria un drama. També vull agrair aquesta tesi a la gent que tot i no ser del grup, per mi en formen part, com són la Cristineto, la Bego i la Fendy.

També vull donar les gracies a les persones que m'han ajudat durant la meva estància a Toronto, especialment al Dr. Se-Woong Baek i al Dr. F. Pelayo García de Arquer, i al Prof. Ted Sargent per deixar-me fer la estada al seu grup. També a tots aquells amb els que he col·laborat externament, com l'Elena Cabello, el Dr. Gabriel Lozano i el Prof. Hernán Míguez del ICMS i la Dra. Luz-Karimé, el Dr. Nicollo Caselli, el Dr. Álvaro Blanco i el Prof. Cefe López del ICMM, per fer que les col·laboracions hagin estat sempre senzilles i agradables.

Fora de l'àmbit professional, les persones a qui més tinc a agrair per aquesta tesi, i la resta de la meva vida en general, són els meus pares, pel seu suport incondicional en tot el que faig i estimar-me com ho feu. Espero que amb aquesta tesi estigueu tan orgullosos de mi com jo ho estic de vosaltres.

A la Inés, per entendre i suportar-me i estar cada dia al costat meu durant, sobretot durant els dies més farregosos d'escriptura de la tesi. Espero en breus poder fer el mateix esforç per a tu.

Als amics més incondicionals, l'Alexis i el Gonzalo, que la vida sempre ens mantingui en contacte.

Moltes gràcies a tots.

Motivation

The ability to harness and control light has pushed the progress of the human society. Fire torches provided extended light hours to the incipient *Homo sapiens*, the invention of the incandescent bulb in the XIX century granted light in confined spaces and, nowadays, incredibly powerful telescopes unveil the composition of far distance galaxies and optical tweezers enable to move single molecules using light. The development of new ways to manage and interact with light has always been driven by the need to produce more efficient optical devices and fueled by new ways to control the composition and structure of the materials used.

Developing compact and highly efficient optical devices is currently the main goal of the fields of optics and optoelectronics. The increasing ubiquity of microdevices, integrated in the so-called "*Internet of things*", pushes the effort towards more efficient, smaller and more robust optical systems. However, when scaling down photonic devices, there is a turning point in which a change of paradigm has to be made. As the size of the components gets close to the size of the wavelength of the light, this cannot be longer treated efficiently with the classical ray optics theories and an electromagnetic wave approach has to be used. This change of paradigm renders some classical light managing strategies obsolete, but also enables a whole new way to interact with light and a plethora of possible new applications. Nowadays, thanks to the enormous advances of nanotechnology, we are able to study and give use to light coupling with nanostructured materials. This has led to countless applications in the fields of light harvesting, imaging, sensing, telecommunications and lightning among others.

One clear example of this change of paradigm can be found in light harvesting technologies such as solar cells and photodetectors. In these, light trapping strategies that confine the light in the active medium are used in order to maximize the absorption within the minimum amount of photoactive material. In macrometric technologies such as crystalline silicon based solar cells, with thicknesses around 300µm, classical light trapping technologies such as micrometric surface texturization are used (**Figure Ia, c**). These have been widely optimized, almost reaching the classical limit of light trapping. However, in emerging optoelectronic devices the dimensions of the active material are well below the micrometric scale. Reducing the thickness also allows the use of more expensive materials, new nanomaterials and nanocomposites at a reasonable cost for daily basis applications. In these cases, the light trapping schemes cannot be based in traditional ray optics strategies. These have to rely in the phenomena such as wave guiding, diffraction scattering and others, that derive from the electromagnetic wave treatment of light

(**Figure Ib, d**). The scientific community has developed sub-micrometric structures and patterns with nanofabrication techniques such as optical lithography, electron beam lithography or nanoimprint lithography that opened the door to the field of nanophotonics.

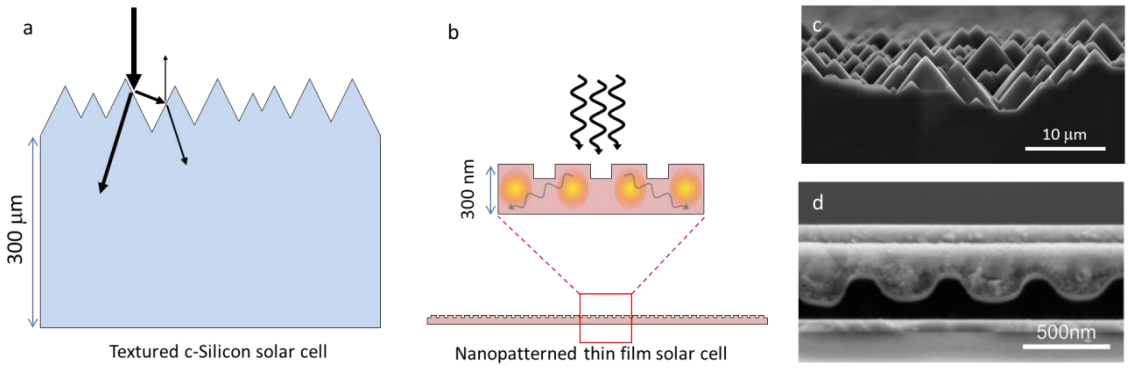

Figure I. *(**a**) Scheme of a textured crystalline silicon solar cell and its multiple reflection light trapping system. (**b**) Scheme of the light trapping system of a thin film nanopatterned solar cell. (**c**) SEM of the micrometric textures in the silicon solar cell and of (**d**) nanopatterned PbS quantum dot solar cell.*[1]

The design and implementation of these new photonic architectures that interact with light at the nanoscale is crucial for the development of efficient state of art compact devices. However, the implementation of promising photonic structures is often hindered by either a low reproducibility or a low scalability of the fabrication process. Therefore, a lot of effort has recently been invested in developing new strategies that render efficient light managing with fabrication processes that are reliable and scalable, which is essential for real applications and industrialization.

Hence, the scope of this thesis will be to develop nanostructured devices for light management using scalable nanostructuring methods. We will mainly use *soft nanoimprint lithography* (NIL) as structuration method, a technique capable to nanostructure a wide range of materials with high fidelity, rapidity, cleanroom-free and at a low cost.[2–4] NIL will be used to fabricate our own photonic designs for light managing, including superabsorbers, metamaterials, light harvesting devices and light emitting platforms, always trying to keep an applicative point of view. We will provide the key aspects for their correct design, such as the main photonic aspects to take into account, the proper materials and features to use, as well as the fabrication methodologies and the characterization of the optically enhanced devices.

Chapter 1

1. Introduction

Since ancient times, light-matter interaction has been fundamental for life. Light is an energy source for plants, serves as versatile camouflage for octopuses and chameleons, and is used as a way to trick prey by anglerfishes in the deep sea. By using fire torches at night, or mixing different pigments to create new colors, the human race began exploiting light for night illumination, artistic purposes, heat and defense. It was only a matter of time to discover and develop the potential of the light-matter interaction. Nowadays, hundreds of applications use light. We have not only been capable to harness the visible light (VIS), but we have squeezed the entire electromagnetic (EM) spectrum from radio waves to gamma rays to find new applications.

For a time, optical lenses and macroscopically sized optical elements have been the cornerstone for optical devices. Although advances in optics with this approach have given lots of technological advances in telecommunications, energy harvesting, audiovisuals technologies, astronomy, lightning and much more, a large sum of applications were still to be discovered. The development of nanofabrication techniques in the past half century has brought up a new way to manipulate light.[5] Thanks to nanophotonics, interacting with light as a wave is possible, unveiling a plethora of new advances in imaging,[6] sensing,[7] lightning[8] and energy harvesting.[9] Nowadays, the development of new photonic devices to harness light at the nanoscale level is one of the most vibrant areas of science.

In order to exploit light for a specific application three fundamental aspects of the light-matter interaction have to be taken into consideration:

1. The electromagnetic wave: which region of the light spectrum are we targeting.
2. Identify the optimum material: the applications of this material, its optical response in the specific spectral range and how it can be processed.
3. The desired optical response that we want to achieve: this will determine the type of optical effect that we need.

In this chapter we introduce how we can design the optical response of a system based on simple photonic resonances and how it would affect the light-matter interaction. We start with the fundamentals of light-matter interaction. Then, we describe the photonic resonances used in

this thesis and the fundamentals behind them. Finally, we discuss some state-of-the-art structures and materials used towards the efficient managing of light and the main challenges still present.

1.1. Fundamentals of light

The treatment of light as an electromagnetic phenomenon was developed by the Scottish physicist and mathematician James Clerk Maxwell in the 1860s. He described the way fluctuating electric and magnetic fields propagating in a medium generate the electromagnetic radiation.[10] He brought together the concepts of light, electricity and magnetism under four equations, in what would be later called the "*second unification of physics*". Nowadays we use a modified version of these same four *Maxwell's equations* (**eq.1-4**) to describe the spatial and temporal propagation of an electromagnetic wave within a material:

$$\nabla \cdot \vec{D} = \rho \tag{1}$$

$$\nabla \cdot \vec{B} = 0 \tag{2}$$

$$\nabla \times \vec{E} = -\frac{\partial \vec{B}}{\partial t} \tag{3}$$

$$\nabla \times \vec{H} = \frac{\partial \vec{D}}{\partial t} + \vec{J} \tag{4}$$

Where $\vec{D}$ is the electric displacement, $\vec{B}$ is the magnetic induction, $\vec{E}$ the electric field, $\vec{H}$ the magnetic field, ρ the free-charge density and $\vec{J}$ the current density. Both the electric displacement $\vec{D}$ and the magnetic induction $\vec{B}$ are constituted by two components: one contribution comes from the electromagnetic wave in vacuum and the other comes from the polarization ($\vec{P}$) and magnetization ($\vec{M}$) in the material, respectively. In linear and isotropic mediums, the constitutive relations are written as:

$$\vec{D} = \varepsilon_0 \vec{E} + \vec{P} = \varepsilon_0 \varepsilon \vec{E} \tag{5}$$

$$\vec{B} = \mu_0 \vec{H} + \vec{M} = \mu_0 \mu \vec{H} \tag{6}$$

Where ε_0 is the vacuum electric permittivity constant and μ_0 the vacuum magnetic permeability constant. The final response can therefore be expressed by the relative electric permittivity ε and relative magnetic permeability μ. These are specific of each material and depend on the

frequency of the electromagnetic wave. The ε and μ are also unitless and complex, where the real part accounts for the strength of the polarization/magnetization and the imaginary part accounts for the thermal losses or optical gain in the material.

$$\varepsilon = \varepsilon' + i\varepsilon'' \tag{7}$$

$$\mu = \mu' + i\mu'' \tag{8}$$

These two magnitudes are related to the response of the medium to the electric and magnetic fields and from them we can infer two important parameters that describe the response of a medium to an electromagnetic wave: the refractive index *n* and the wave impedance *z.*

$$n = \sqrt{\varepsilon\mu} \tag{9}$$

$$z = \sqrt{\frac{\mu}{\varepsilon}} \tag{10}$$

The refractive index refers to the speed of light in the medium (*c*) relative to the speed of light in vacuum (c_0). The wave impedance (z) refers to the resistance that the material offers to the wave propagation, also relative to the vacuum impedance. These values characterize the light-matter interactions. In this sense, it is essential to know these parameters of the materials that we plan on using in our optical devices. They indicate us the suitability of the selected material for applications either if we need high or low absorptions, light confinement, strong reflection, high transmission or other optical characteristics.

1.2. Optical properties of materials

The optical properties of a material determine its interaction with light and depend on its electric permittivity and magnetic permeability. However, while the electrons of the materials, related to the polarization, can couple to uv-vis frequency, their spins, related to the magnetization, couple with the microwaves. Thus, in the wavelength range (VIS and NIR) and materials that we are going to work with, the relative permeability can be taken as μ= 1, meaning that the magnetization of the materials can almost be neglected. Natural materials exhibit negligible magnetism at optical frequencies, since the direct effects of magnetic optical fields are much weaker than the electric ones. On the other hand, the behavior of the electric permittivity will be quite different depending on the type of material and will characterize the

optical response. Thus, the refractive index will be written as $n = \sqrt{\varepsilon}$. Although in this work we employ sub-micrometric structures, within the size range of the fabricated features, the dielectric constants can still be approximated to the ones of the bulk. As for other properties, when categorizing the materials for its optical properties, in this doctoral work we focus on two main groups: metals and dielectrics.

1.2.1. Optical properties of metals

The presence of free electrons in metals is the main factor that influences their optical properties, rendering them with their characteristic metallic luster. As they present a negative value of the real part of the electric permittivity ($Re[\varepsilon_m] < 0$ (**Figure 1**)), the material will be polarized at the reverse direction of the electric field. Therefore, the field is not allowed in the metal and expelled outside, reflected, giving them their characteristic shininess. Upon illumination, the plasma of electrons follows the field, cancelling it completely. However, if the frequency of the impinging light is higher than the characteristic plasma frequency of the metal (ω_p) -usually in the ultraviolet (UV) region- the electrons fail to follow the electromagnetic field oscillation. In this case, the metal loses its reflectivity, allowing the electromagnetic radiation to permeate into the bulk, although generally with high damping.

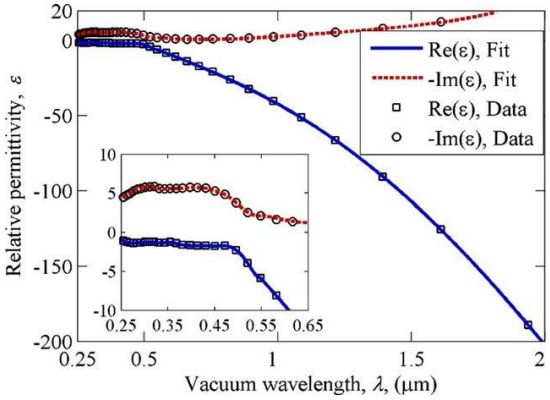

Figure 1. *The real and imaginary parts of the relative permittivity of gold are plotted as a function of the wavelength from 250 to 2000 nm. The inset shows in greater detail the material dispersion in the visible and UV ranges.*[11]

In the projects developed in this thesis metals are mainly used as a reflecting media. In some cases we will also take advantage of the non-ideal reflectivity of some metals and the photonic resonances that may occur in the metal-dielectric interface, which will be explained in the following sections.

1.2.2. Optical properties of dielectrics and semiconductors

The dielectric and semiconductor materials, contrarily to the aforementioned metals, have the electrons bounded to the atoms. Therefore, they are electrical insulators, or almost, in case of the dielectric semiconductors. However, they do polarize; the cloud of electrons shifts its position relative to the atomic lattice as a result of an impinging EM field. This relates with a positive electric permittivity, real or complex depending on the absorption losses. This gives values of refractive index $n = \sqrt{\varepsilon} > 1$. Regarding the refractive index, for this thesis and in terms of photonic applications, we can distinguish two types of dielectrics materials: low, and high refractive index materials.

1.2.2.1. Low refractive index materials

Low refractive index materials, generally dielectrics, are those with $1 < n < 2$. Within this group we can find the vast majority of polymers, resists, biomaterials and porous materials (**Figure 2**). Contrarily to high refractive index dielectrics, the majority of low refractive index materials are transparent, with almost constant values of n in the visible and NIR. In photonic devices, these are often used as propagating media, as lossless substrates, as antireflection coatings and as main material in optical components such as lenses.

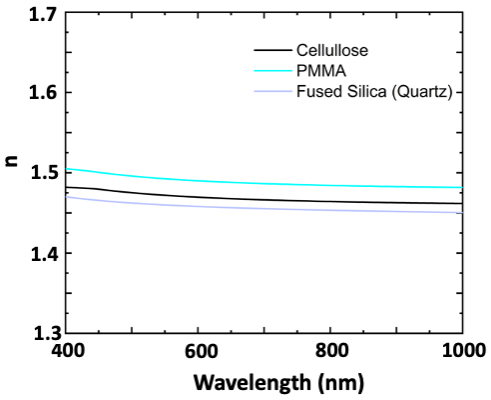

Figure 2. *Refractive indexes of transparent materials such as cellulose (black line), the most abundant biopolymer on earth, polymethyl methacrilate (PMMA)(blue line), a photoresist widely used in electronics, and fused silica (grey line) used in optical lenses and optical components.*

1.2.2.2. High refractive index materials

High refractive index materials are those with $n > 2$, comprising mostly semiconductors. This implies that the light travels in the medium significantly slower than in vacuum. Therefore high index materials are excellent candidates to obtain strong light-matter interaction, light confinement and light trapping. Transparent high refractive index materials, with no absorption in the visible range, are quite scarce. Amongst them we can find wide band gap semiconductors such as titanium dioxide (TiO_2) and silicon nitride (Si_3N_4); and dielectrics such as the carbon diamond (**Figure 3a**). However, their refractive index do not reach values of $n > 3$, which can be obtained with lower band gap semiconductors such as silicon, germanium, gallium arsenide (GaAs) and indium gallium arsenide (InGaAs)(**Figure 3b**). This comes at the cost of a non-negligible imaginary part of the refractive index k in the visible range, responsible for light absorption (**Figure 3c**). These characteristics makes them appealing for applications where strong absorptions are needed, such as photovoltaics[12,13] and photodetection.[14,15] Although they have strong absorption in the visible, they have been proven also to be good candidates for applications in the NIR and IR where low losses are required. These high index materials can present strong light confinements and high scattering cross sections comparable to their metallic counterparts, with lower optical losses. This makes them appealing materials for the building blocks of nanoantennas[16], photonic crystals[17] and metamaterials.[18]

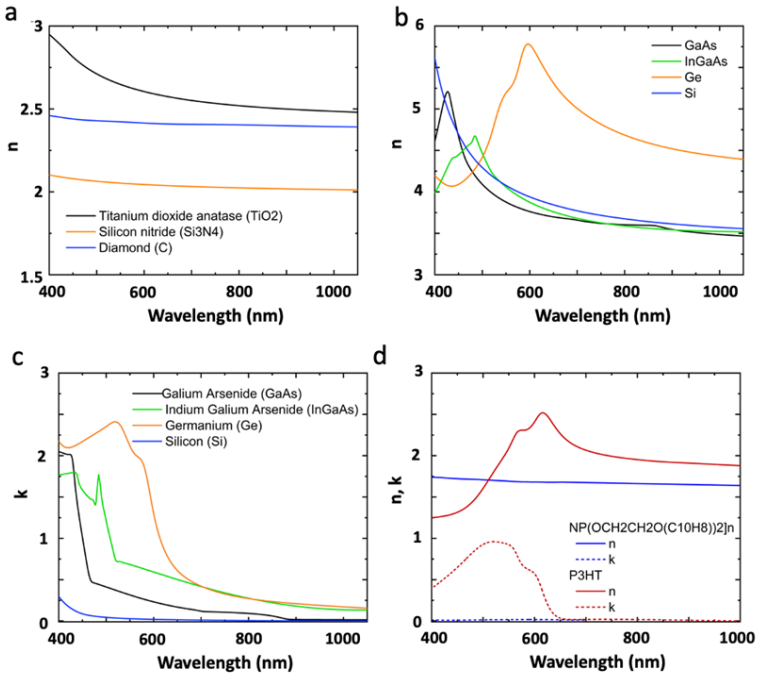

Figure 3. *Refractive indexes of (**a**) transparent dielectrics, (**b**, **c**) absorbing semiconductors, (**d**) polymers.*

A special case are the “high refractive index polymers”: these are the transparent polymers with refractive index above 1.6 (**Figure 3d**).[19,20] This nomenclature is due to the difficulty to obtain fairly transparent polymers with high refractive indexes. Absorptive polymers with $n \approx 2$ are more abundant and generally used in solar cells[21] and photodetection.[22] “High refractive index transparent polymers” are often used in antireflecting coatings of light-emitting diodes (LEDs).[23]

In particular, high refractive materials have been used in this thesis to take advantage of the high confinement properties and the strength of the resonances that they offer.

1.3. A brief classification of photonic resonances

In this section we describe the main tools, the photonic resonances, that can be used to manipulate light at the nanoscale. These tools offer a new way to manage light, moving away from the macroscopic ray optics classical treatment of the light and its associated limitations. We focus on resonances that allow us to confine and modulate light at the sub-wavelength scale, unveiling a wide range of new properties and enabling the miniaturization of optoelectronic devices.

A photonic resonance, also called photonic mode, is a reinforcement or prolongation of an electromagnetic wave by the constructive interference of smaller electromagnetic waves. Photonic resonances are used to manage, control light, and to maximize its interaction with a medium. As introduced in the last section, the type of material or combination of them is essential to understand the optical response of a system. However, their spatial distribution, geometry and structure are crucial to obtain strong photonic resonances to manipulate light. Among all the photonic resonances that may be produced in the light-matter interaction, in this section we will briefly describe those most relevant to this thesis.

1.3.1. The thin film interference resonance

1.3.1.1. Origin

The thin film interference photonic resonance arises from the interference between the reflected EM waves from the upper and lower boundaries of a thin film (**Figure 4**). If the difference between the optical paths (ΔOP) of the waves reflected in the first and second

interfaces of the thin film is equivalent to an integer number of the impinged wavelength ($\Delta OP = m\lambda$), the resulting reflected wave will be maximum. In the other hand, if $\Delta OP = (2m+1)\frac{\lambda}{2}$, the resulting interference will be destructive. When calculating the optical path mismatch we also must take into account that light gets an extra half-wavelength phase shift when reflected from a higher refractive index medium. For instance, in a system as pictured in **Figure 4,** composed by two semi-infinite mediums, M1 and M3, with refractive indexes n_1 and n_3, surrounding a planar layer of a material M2 with a higher refractive index n_2, we can derive from Snell's law, the following relations (**eq.11, 12**):

$$2n_2 d\cos\theta_2 = \left(m - \frac{1}{2}\right)\lambda_1 \tag{11}$$

$$2n_2 d\cos\theta_2 = m\lambda_2 \tag{12}$$

The relation in **eq. 11** describes how to obtain constructive interference in the reflected field (and destructive interference for transmitted field) for the specific wavelength λ_1 with a given material thickness d, where m is an integer number. θ_2 accounts for the angle of refraction, which is also the reflection angle in the lower boundary between M2 and M3. In the other hand, **eq.12** generates destructive reflectance interference and constructive transmittance interference for specific λ_2.

Note that if one of the refractive index of the two surrounding media, either n_1 or n_3, is larger than n_2, the presented relations describe the opposite interference effects due to the extra half-wavelength phase shift mismatch produced by the light reflected from a higher index medium. Therefore, satisfying **eq. 11** would generate a destructive reflectance interference, and **eq.12** a constructive reflectance interference.

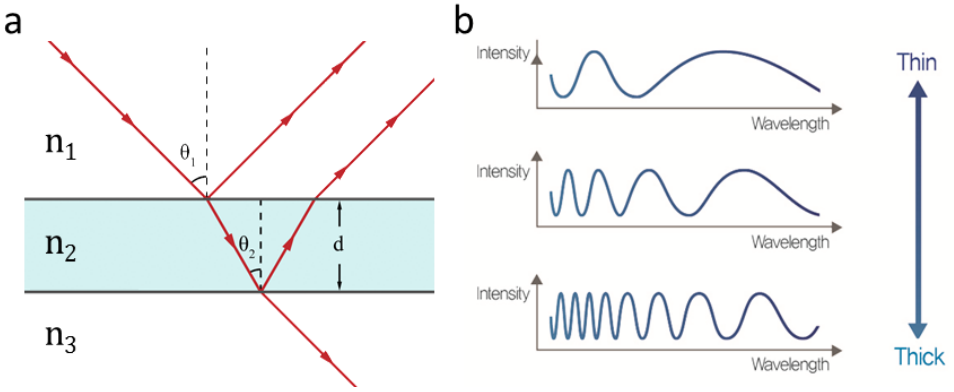

Figure 4. *(**a**) Scheme of the studied multilayer system. (**b**) The interference pattern of the intensity of the reflected light as a function of the thickness of the film.*

1.3.1.2. Characteristics

The nature of the interference depends only on the refraction indexes of the layers involved, the film thickness, and the incident angle of the impinging light. As the thin film gets thicker or the refractive index of the film increases, an enlargement of the optical path will occur and the interference resonances get spectrally narrower, as depicted in **Figure 4b**. It is also important to take into account that optical losses such as absorption in the material, scattering due to roughness in the interfaces, or grain boundaries, will damp such interferences.

This simple design has provided outstanding applications in various optoelectronic fields. It is often referred to as a Fabry-Perot resonant cavity (FPC) after Charles Fabry and Alfred Perot, who invented an interferometer using this type of resonance back in 1899.[24] In a Fabry-Perot interferometer one of the two interfaces has a high reflectance (**Figure 5a**). Generally partially reflective mirrors are used. The more reflective the interfaces, the sharper the Fabry-Perot resonances (FPR) obtained (**Figure 5b**). When one of the two interfaces is a metal the system is called a Gires-Tournois interferometer[25], which is further discussed in **chapter 3.**

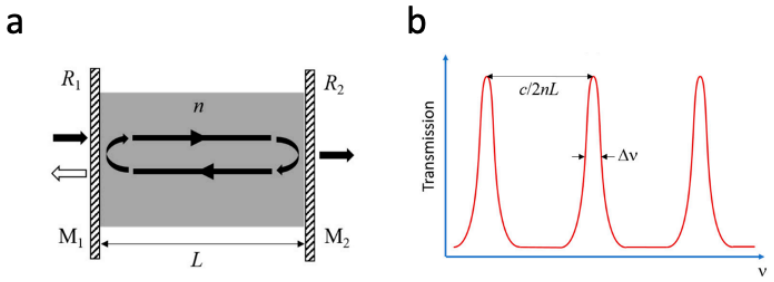

Figure 5. *(**a**) Schematic of a Fabry-Perot resonator consisting of parallel mirrors M 1 and M 2 with reflectances of R 1 and R 2 , respectively, surrounding a cavity medium of refractive index n and thickness L. Light introduced from one side undergoes multiple reflections, leading to partial transmission from the other side; (**b**) typical transmission of a planar FPC depicting frequency spacing (i.e., the FSR) of adjacent longitudinal modes and the full-width at half-maximum (Δv) of an individual modal peak.*[26]

1.3.1.3. Uses and applications

The thin film resonance has been used for a wide range of applications in the photonic community: as optical cavities for lasers[27], dichroic filters[28], telecommunication multiplexers[29], optical wavemeters[30], spectrophotometers[31], to measure layer thicknesses by

interferometry,[32] as a source of structural colour,[33] for light harvesting in solar cells[34] and photodetectors[35] and even nowadays are used in gravitational wave detectors.[36] For instance, a simple FPC metal/active layer (AL)/metal cavity design has been used to fabricate photodetectors based on weak subgap absorption of intermolecular charge-transfer states of organic polymer blends (**Figure 6a and b**). This enables a highly wavelength selective, near-infrared photoresponse with a spectral resolution down to 14 nm. The direct dependence of the resonant wavelength with the thickness allows for the fabrication of a miniaturized spectrophotometer by generating a device with an active layer gradient thickness (**Figure 6c and d**).

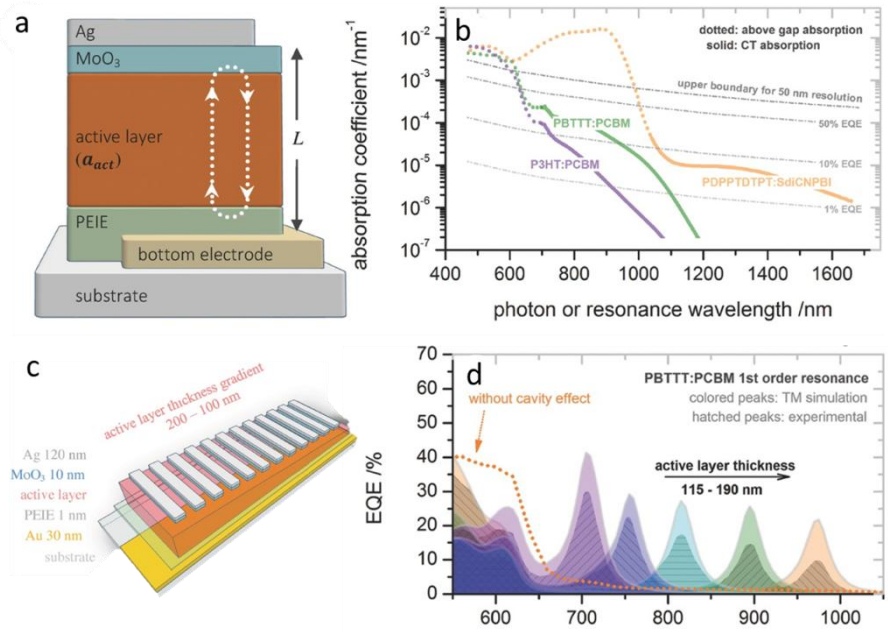

Figure 6. *(**a**) Schematic device architecture of a resonant-cavity-enhanced organic photodetector. The resonance wavelength is tuned by varying the thickness of the active layer. (**b**) Absorption coefficients of P3HT:PCBM 1:1 (weight ratio), PBTTT:PCBM 1:4, and PDPPTDTPT:SdiCNPBI 1:1. (**c**) Miniature NIR spectrometer with a thickness-wedged PBTTT:PCBM (1:4) layer in a metal–metal cavity. The spectrometer is based on a single-wedged active layer, resulting in different resonance wavelengths for each individual detecting pixel. (**d**) Performance of the photodetector in a metal–metal cavity structure. Measured (hatched peaks) external quantum efficiencies (EQE) and simulation (colored peaks) predicted EQE (assuming an internal quantum efficiency of 100%) for devices with an active layer thicknesses varied between 115 and 190 nm.*[35]

There have been efforts to go a step further where one can create a system that sustains not only one, but two different FPR-like resonances to enhance the efficiency of solar cells.[9] This can be achieved by engineering the amount of layers in a solar cell and a fine adjustment of their corresponding thicknesses (**Figure 7a and b**). This resonance scheme has been called two-resonance tapping cavity (TRTC) and has been proven effective to enhance the short circuit current (J_{sc}) of 2mA/cm^2 in highly efficient organic solar cells, with no detrimental effect on other figures of merit such as the filling factor (FF) or the open circuit voltage (V_{oc}) (**Figure 7c and d**).[9]

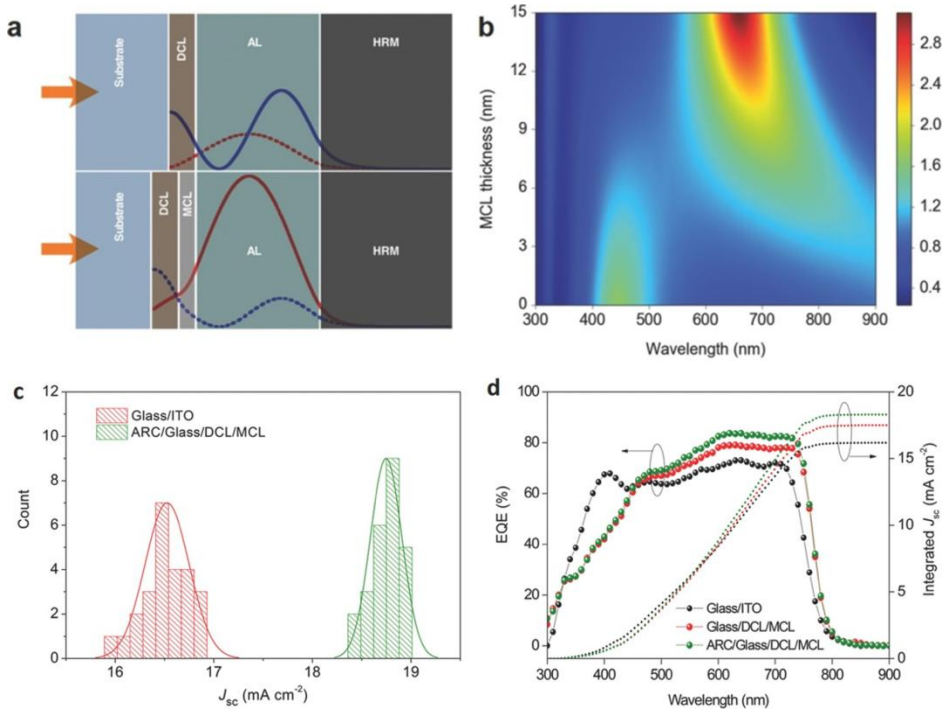

Figure 7. *(**a**) Schematic diagram of cavities formed by an active layer (AL) dispersion less layer sandwiched in between a dielectric cavity layer (DCL) and the backreflector (HRM) (top), and by an AL sandwiched in between a DCL/metal cavity layer (MCL) and the backreflector (bottom). Blue and red curves correspond to field intensity distributions at 440 and 655 nm, respectively. The resonant field intensities are shown as solid lines, while the non-resonant ones are shown as dashed. (**b**) Dependence of field amplitude in a dispersion less active layer with the MCL thickness. (**c**) Jsc distribution for 25 devices without (red bars) and with (green bars) the designed TRTC. The solid lines represent the Gaussian distribution fittings. (**d**) Experimentally measured EQE and integrated Jsc from EQE curves for a cell with the TRTC (green), with the TRTC and an extra antireflection coating (red), and without the TRTC.*[9]

1.3.2. Mie Resonances

1.3.2.1. Origin

Mie resonances, named after the German physicist Gustav Mie (1868-1957), account for the EM field spatial distribution of a plane wave of light impinging on a spherical body with diameter similar to or larger than the wavelength of the light. The Mie solution to the Maxwell's equations in these systems is composed of a series of spherical harmonics with electric and magnetic components (Mie coefficients a_m and b_m). The equation that describes the scattering coefficient (**eq.13**) reads as:

$$Q_{sca} = \frac{2}{k^2 r^2} \sum_{m=1}^{\infty} (2n+1)(|a_m|^2 + |b_m|^2) \qquad (13)$$

Where *k* is the wavevector outside the particle; n the refractive index of the material; *r* is the radius of the sphere; *m* is the order of the present modes and a_m and b_m are the electric and magnetic Mie coefficients composed of Bessel and Hankel spherical functions.

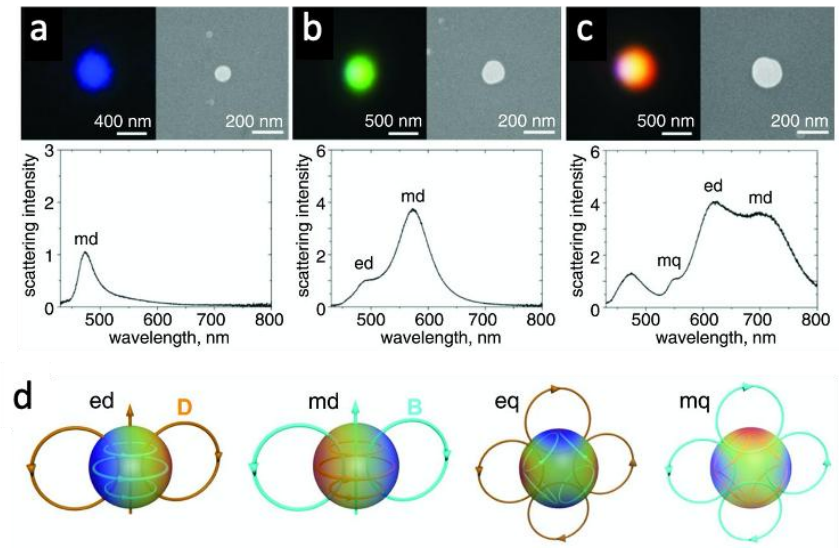

Figure 8. *(**a** - **c**) Dark-field optical microscope images (top left), scanning electron microscope (SEM) images (top right), and dark-field scattering spectra (bottom) of spherical Si nanoparticles with approximate diameters of 100 nm (**a**), 140 nm (**b**), and 180 nm (**c**). (**d**) Illustration of electric and magnetic field structures for different electric and magnetic resonances supported by a spherical dielectric particle.*[37]

For a spherical resonator with radius *r* and refractive index *n*, the lowest-order peak, responsible for the scattering at higher wavelengths, corresponds to the magnetic dipole (MD) mode. This

can be seen in **Figure 8a**, where only the magnetic dipole mode is supported by the 100 nm dielectric sphere. This magnetic dipolar resonance, with coefficient b_1 appears at the approximate wavelengths of:

$$\lambda = 2nr \tag{14}$$

In **Figure 8a-c** we can observe that the following modes that appear as we increase the radius of the sphere are the electric dipole (ED) modes with coefficient a_1, and the quadrupolar magnetic and electric modes with coefficients b_2 and a_2.

1.3.2.2. Characteristics

The representative EM field's schemes for these resonances are depicted in **Figure 8d**. In the magnetic dipole resonance, the circulation of the electric field induces a magnetic dipole moment. In the electric dipole resonances, the tables are turned, a circulation in the magnetic field produces an electric dipole. Higher modes, such as quadrupolar modes, tend to be more complex to characterize and may have different variants, generally with lower scattering intensities than the dipolar modes, as can be seen in **Figure 8c**. The higher scattering intensity, the more feasible characterization and the more straightforward tunability of the magnetic and electric dipolar modes will make them of central importance in this doctoral work, above higher order modes.

Even though Mie theory was initially developed for spherical particles, it is extended also to multilayered spheres and arrays of spheres. Also, other geometries of particles such as rods, discs and hemispheres can sustain Mie like modes (**Figure 9**). Moreover, by modifying the geometry of the particle, we can tailor the Mie resonances. For instance, one can maximize or suppress one specific mode resonance, or obtain zero backward scattering overlapping the ED and MD, reaching the so called Kerker effect.[38]

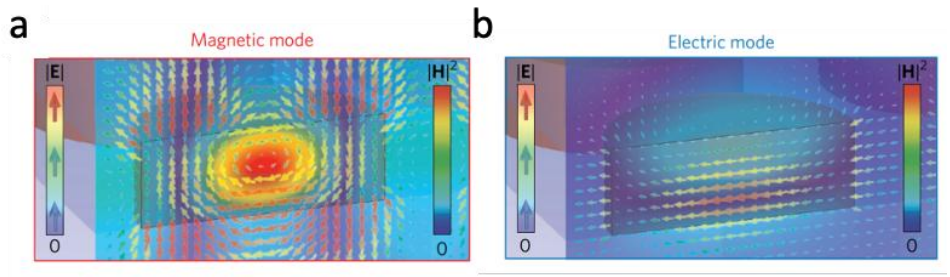

Figure 9. *(**a**) MD and (**b**) ED mode profiles of the dipolar modes of a silicon nanodisk.*[39] *|E| is the modulus of the electric field and $|H|^2$ is the square modulus of the magnetic field.*

One area that raises a lot of interest in the scientific community and that will be exploited in **chapter 4** is the study of the sub-micrometric spheres of silicon and other high dielectric index materials. These materials sustain both strong electric and magnetic responses in their Mie modes and have smaller losses compared with their metallic counterparts. They are of special interest as their Mie resonances offer the possibility to achieve strong optical magnetic resonances in the VIS and NIR regime, something not achievable with metallic spheres nor with natural bulk materials.

In addition, one can couple the Mie resonances of two or more nanoparticles when they are brought close to each other in dimers and clusters (**Figure 10**). The EM induced resonances of coupled nanoparticles can be derived from the generalized Mie theory. Coupled nanoparticles can sustain resonances with strong near field intensity in the gaps present in between the nanoparticles, generating the so-called hotspots. The coupling of plasmonic metallic nanoparticles can produce electric hotspots with higher field enhancements than their dielectric counterparts, easily reaching 100-fold enhancements.[40,41] Interestingly, high refractive index dielectric dimers and clusters can support resonances not only with electric hotspots[42,43] but also with magnetic hotspots (**Figure 9**)[44,45] reaching a 100-fold magnetic field intensity increase.[46]

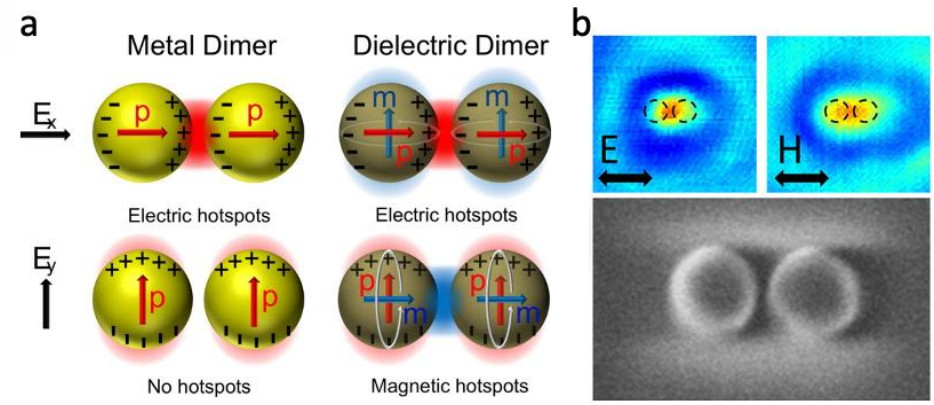

Figure 10. *(**a**) Comparison of metallic (plasmonic) and dielectric nanodimers. Plasmonic dimers (left) only have electric dipoles that couple under a single polarization while dielectric dimers have both electric dipoles and magnetic dipoles that couple under the orthogonal polarizations. (**b**) Magnetic and electric near-field enhancement in a nanogap between two silicon nanocylinders and SEM characterization (height, 150 nm; diameter, 140 nm; gap, 30 nm).*[46]

1.3.2.3. Uses and applications

The ability to concentrate far-field incoming light in small volumes with strong near-fields, have rendered Mie resonances useful as nanoantennas in applications such as sensing and light emission.[16,47] The main characteristic of Mie resonances exploited for light emission applications is the possibility to increase the local density of optical states (LDOS) of the system by the enhancement of the near-field.[42] As shown in **Figure 11,** this often leads to increased light emission;[48] but also modulated directivity[49] and tunability of the emission wavelength[50] can be designed and engineered with the proper nanoantenna array.

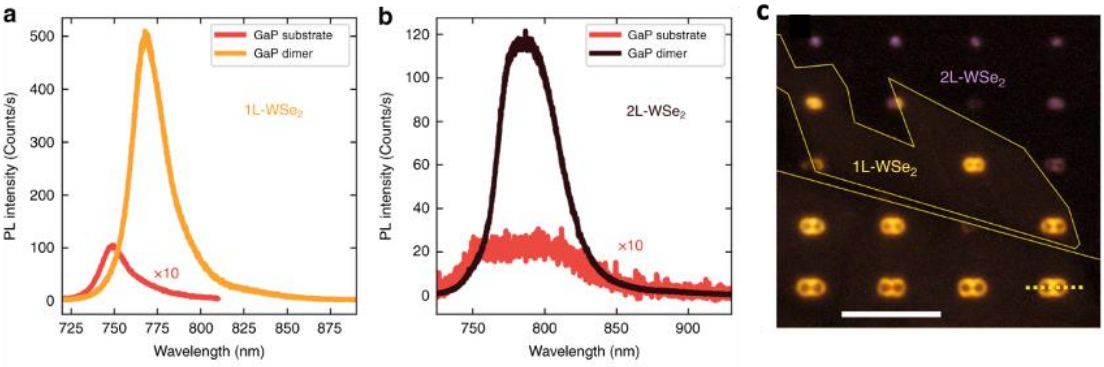

Figure 11. *Photoluminescence enhancement of a monolayer (1L) and bilayer (2L) of WSe_2 coupled to gallium phosphide nanoantennas. (**a**),(**b**) PL spectra for 1L-WSe_2 (orange) and 2L-WSe_2 (black) placed on top of gallium phosphide nanoantennas with r = 300 and 100 nm, respectively. Spectra in red are measured on 1L- (**a**) and 2L-WSe_2 (**b**) placed on the planar GaP. Their intensity is multiplied by 10. (**c**) Optical microscopic image showing PL from dimer nanoantennas array covered with 1L- and 2L-WSe_2 illuminated with unpolarised white light. Scale bar is 10 µm. The yellow lines show the boundaries between 1L- and 2L-WSe_2. PL from 1L (2L) sample is shown as false yellow (purple) in the image.*[48]

Originally, plenty of attention was drawn to metallic nanoantennas using plasmonic resonances to concentrate light and obtain large values of near field intensity. However, in this thesis we will focus our attention more in dielectric nanoantennas as an alternative to metallic structures to try to avoid the already mentioned plasmonic inherent losses and other deleterious effects such as quenching and heating. Magnetic hotspots also generate an increase in the LDOS, with effect in the magnetic transition rates of emitters, deriving in an enhanced Purcell factor.[51] There has been also a rising interest in using high dielectric refractive index Mie particles as building blocks for metamaterials, especially for magnetic metamaterials in the telecom and near infrared frequencies.[18,37]

1.3.3. Diffracted Modes

1.3.3.1. Origin

Diffraction occurs when a wavefront impinges onto an object or an aperture and the waves bend around the edges of the object (or the aperture), converting the latter in an effective secondary source. This phenomenon is not exclusive of electromagnetic waves and can be easily seen in water, as in the harbour presented in **Figure 12a**. The diffracted wave interferes and interacts with the original wavefront, creating a diffraction pattern characteristic to the object.

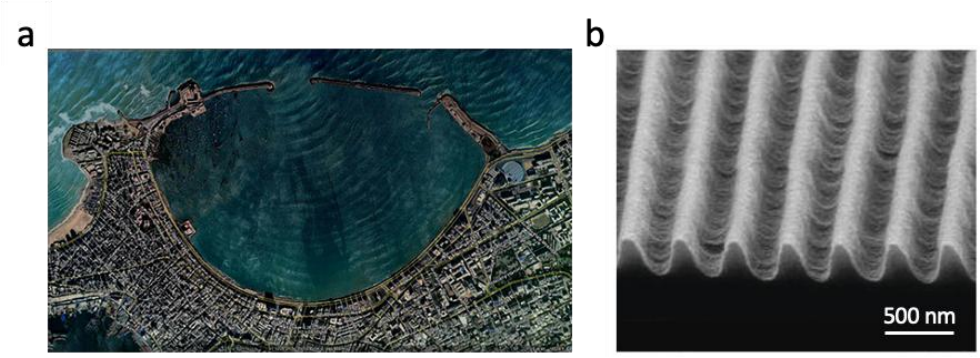

Figure 12. *(**a**) Diffraction of water waves in a harbour*[52]*. (**b**) Scanning electron microscopy of a diffraction grating.*[53]

In this thesis, we will focus on the diffraction of light produced by a periodic arrangement of objects, the so-called diffraction gratings (**Figure 12b**). The periodicity of the scatterers or secondary emitters may produce a constructive (or destructive) interference of secondary waves. The resonant modes, the diffraction modes, highly depend on the wavelength and both the incident and the diffracted angles. These diffraction modes produced by a one-dimensional grating must satisfy the following relation (**eq.15**):

$$m\lambda_0 = n\Lambda(\sin\alpha + \sin\beta_m) \qquad (15)$$

Where m is the diffraction order (an integer number); n, the refractive index of the media; Λ, the lattice parameter of the grating; α, the incidence angle and β, the diffracted angle (**Figure 13b**). This relation is closely related to Bragg's Law, which honors Lawrence Bragg and his father William Henry Bragg, who discovered in 1913 that crystalline solids produce interference patterns when illuminated with X-rays. The phenomenon that they were observing was the diffraction of X-rays by the atomic crystalline lattice. An example for light impinging in a normal

incidence (α =90°) is presented in **Figure 13a**. A constructive interference, a diffraction mode, occurs when the mismatch of the optical path (ΔOP) between the different scatterers - a multiple of $\Lambda \sin \beta$ -, is equivalent to a multiple of the wavelength ($m\lambda$). For each wavelength, there are several specific angles where these conditions are satisfied, which are the different diffraction orders (m) (**Figure 13b**).

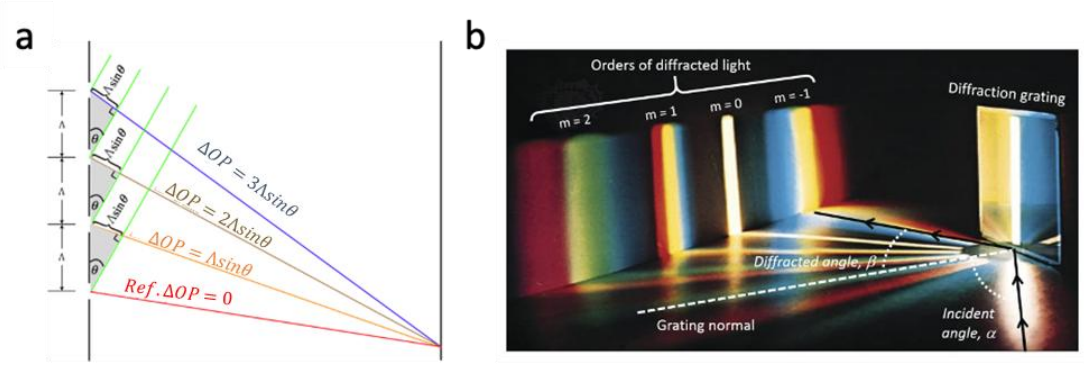

Figure 13. *(**a**) Scheme of the optical path in a four slit diffraction grating with the mismatch obtained between the different slits .*[54] *(**b**) Polychromatic light diffracted by a grating.*[53]

1.3.3.2. Characteristics

The main characteristic of the diffractive modes of a grating is their angular dispersion, the difference of diffractive angle per wavelength. With a fixed incidence angle α, we can obtain the angular dispersion *D* (**eq.16**) by differentiating the grating equation (**eq. 15**) by the wavelength λ:

$$D = \frac{\partial \beta}{\partial \lambda} = \frac{m}{\mathrm{n}\Lambda \cos(\beta_m)} \qquad (16)$$

We can observe that for a given diffraction order *m*, the angular dispersion *D* increases as the lattice parameter Λ goes smaller. This parameter is essential as in spectral analysis; resolution is measured as the capacity of the device to separate two spectral lines that are spectrally close. High quality gratings can achieve spectrally sub-nanometric sharp resonances.[55]

We can spatially locate the diffraction modes depending on the media where they propagate: diffraction modes in reflection, in transmission, and in the plane of the grating. The latter ones are also known as Rayleigh-Wood's anomalies (RAs) and will be explained in more detail in **chapter 5**. Despite these three modes emerge from the same phenomena, and can be simultaneously excited, it is important to control which of them is the dominant one in order to fit it in a specific application.

Also, which will be of key relevance in this thesis, the diffraction modes of a grating provide light with extra momentum parallel (G_m, **eq.18**) to the grating surface (**Figure 14a**).

$$k_{||} = k_{||0} \pm G_m \tag{17}$$

Where:

$$G_m = \frac{2\pi m_x}{\Lambda} \tag{18}$$

The extra $k_{||}$ will depend on the lattice parameter and the diffraction order. Note that the wavelength at which the diffraction occurs depends on the refractive index of the propagating medium of the diffraction mode, as $k = n\frac{2\pi}{\lambda}$. This extra $k_{||}$ will enable light to couple to resonances that could not be accessed due to a momentum mismatch, such as surface plasmon polaritons (SPP) and thin film guided modes (GM), which will be explained in the following sections (**Figure 14b**).

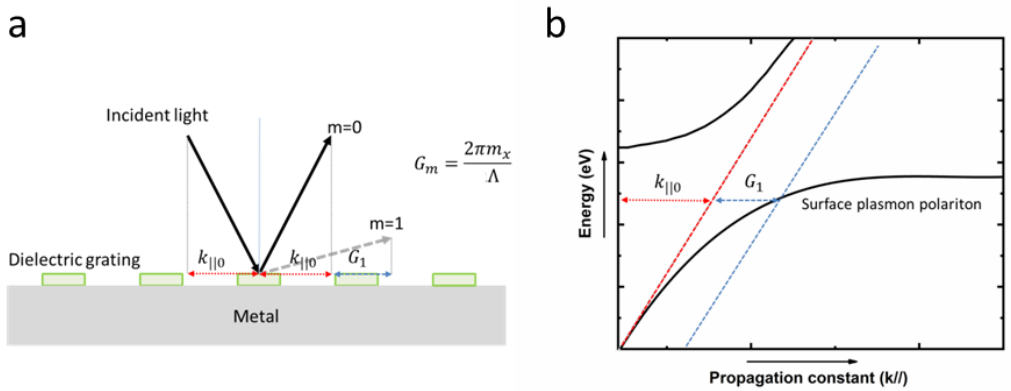

Figure 14. *(**a**) Scheme diagram of the excitation of SPP of a metal with a dielectric diffraction grating. (**b**) Dispersion diagram illustrating the extra parallel momentum provided by the grating generating the phase matching condition.*

1.3.3.3. Uses and applications

Diffraction modes have been widely used to manipulate light in optoelectronics as they render the ability pin point specific targeted wavelengths with high resolution.[55] They are fundamental in applications such as spectroscopy[56] and telecommunications[57] to spatially separate the different wavelengths of the light. Also, diffraction gratings have been used in light harvesting technologies such as solar cells[1,58], photodetection[59] and photocatalisis[60] as they allow the impinging light to couple to longer optical paths inside the active material, rendering in more

efficient devices (**Figure 15**). As already mentioned, diffraction gratings are widely used in applications where it is needed to couple light to electromagnetic modes (photonic and plasmonic), non-accessible from air due to a momentum mismatch.[61,62]

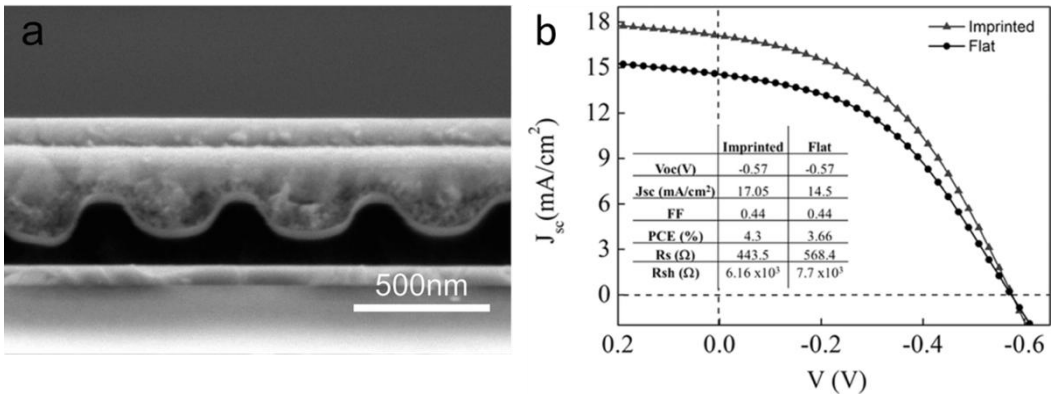

Figure 15. *(**a**) Scanning electron micrograph of a PbS-ZnO heterojunction solar cell on an imprinted 2D diffraction grating electrode. (**b**) Intensity–Voltage characteristics for the champion imprinted (triangles) and flat (dots) devices. The different figures of merit extracted from these curves are presented in the inset table: Open circuit Voltage (V_{oc}), short-circuit Current Density (J_{sc}), fill factor (FF), Power Conversion Efficiency (η) and series and shunt resistivity (R_s and R_{sh}).*

1.3.4. Guided Mode resonances

Guided modes (GM) are propagating modes whose electromagnetic field is confined in a substrate (the waveguide) and exponentially decays at the media surrounding it. The most commonly known guided modes are those found in the optical fibers, where generally a higher dielectric index n_{core} material is surrounded by a cladding one of lower index n_{clad} (**Figure 16**). The light coupled into the core can be totally internally reflected and confined in the core when the internal reflection angle θ_r surpasses the critical angle. We can easily use Snell's law (**eq.19**) to calculate this angle:

$$n_{core}\sin\theta_r = n_{clad}\sin\theta_t \tag{19}$$

$$n_{core}\sin\theta_r = n_{clad}\sin(90) \tag{20}$$

$$\theta_r = \arcsin\frac{n_{clad}}{n_{core}} \tag{21}$$

The limit angle to obtain no transmitted light is found by setting the transmitted light refraction angle $\theta_t = 90$ (**eq.20**, **21**), where the refraction is perpendicular to the interface. This approach is also applicable to planar waveguides, where a waveguide medium with refractive index n_w is surrounded by mediums with lower refractive indexes n_1 and n_2.

1.3.4.1. Characteristics

The essential characteristic of guided modes is that they are non-radiative in the outside media; they are confined into the waveguide medium. In the absence of losses, this means that one optical signal can propagate indefinitely through the waveguide with minimal disruption.

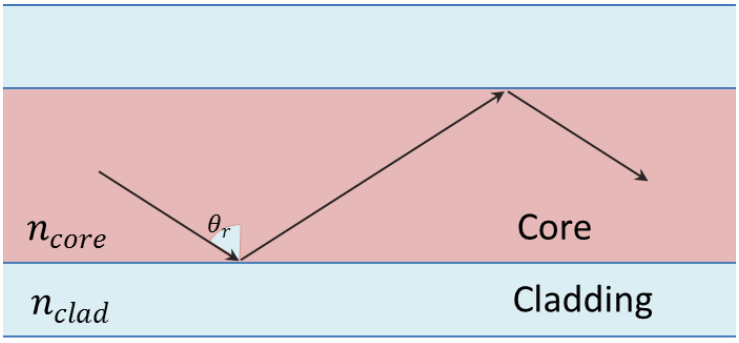

Figure 16. *Scheme of a guided mode in an optical fiber.*

Another important characteristic is that they cannot be accessed from air, according to the previously used Snell's law. If the in-coupling to these modes would be possible from the air, then, by reciprocity, so would be the out-coupling, meaning that they would not be guided modes. As shown in **Figure 17**, the light impinging directly from air (light cone), does not have enough propagation constant, momentum parallel to the interface, to couple to the guided modes of the 2D waveguide (blue and green lines). To compensate the momentum mismatch and access the GM, a prism coupler or a diffraction grating coupler can be used (**Figure 17 c and b** respectively). A prism coupler consists on a high refractive index glass prism, often rutile, separated from the waveguide layer (and the underlaying lower refractive index substrate), by a tunneling layer, generally of air or a low refractive index material. The evanescent wave of the light impinged through the prism can tunnel the air gap and couple to the guided modes of the waveguide. Thanks to the higher refractive index of the prism, the directed light has enough parallel momentum to couple to the guided modes of the waveguide. On the other hand, and as explained in the previous section, diffraction gratings grant the light with extra parallel momentum which enables it to phase match the required momentum to couple to the GM. We

must point out though, that, while we create a way to in couple light into the waveguide, we are also enabling the out-coupling of the guided light back into the environment and, therefore, these modes become quasi-guided modes (QGM).

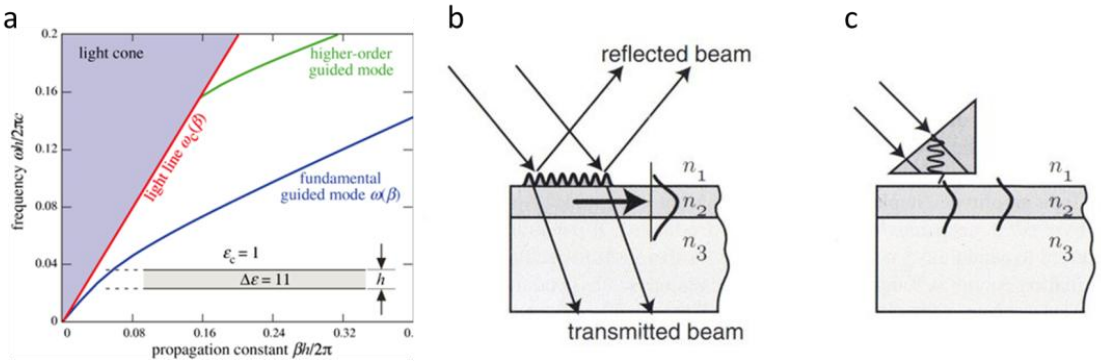

Figure 17. *(**a**) Example dispersion relation of a simple 2D dielectric waveguide in air (inset), showing the light cone, the light line, the fundamental (cutoff-free) guided mode, and a higher-order guided mode with a cutoff.*[63] *(**b**) Schematic showing light coupling to guided modes through a diffraction grating coupler and (**c**) a high refractive index prism.*

1.3.4.2. Uses and applications

Guided modes are extensively used in telecommunication systems to transmit signals.[64,65] The transmission of NIR light-encoded information through the optical fibers offers much lower signal losses than the electric-encoded information transmission provided by metallic wires. In addition, optical fibers offer higher data transfer rates and are and are less sensitive to electromagnetic interferences, which is a problem in wired systems. Also, the ability to transfer unperturbed light of optical fibers is used in illumination and imaging.

The coupling to guided modes, thus confining the light into a desired medium, also provides with strong light-matter interaction. In the context of this thesis, the ability of guided modes to "*trap*" the light and maximize its optical path inside the active medium of solar cells and photodetectors will be a key element in obtaining high efficiency devices, as all reflected and non-absorbed light is detrimental to the performance of the device. Macroscopic surface textures have been used to maximize the light trapping in crystalline silicon solar cells, with thicknesses around 300 microns. However, this strategy is not suitable for thin devices, whose thickness is comparable or smaller to the thickness of the proposed macroscopic textures; around 1-5 microns. A more convenient approach, among others, is to design the solar cell in a

way that the active layer acts as waveguide. Thus, light coupled to the guided modes can be fully absorbed. In **Figure 18a,** it is presented a 1 micron thick thin film c-Si solar cell over a perfect backreflector with a nanostructure on top composed of a periodic array of nanowires.[66] This design will enable to couple the light to guided modes (or QGM), rendering the solar cell with higher absorptions. Looking at the electric field distribution at specific resonant wavelengths (**Figure 18b**) can help understanding the nature of the coupling mechanism to the GM and some other common resonances used for light trapping that have been used along this thesis (**Figure 18 c-f**). Each resonance, labeled from 1-4, can be identified by its absorption angle dependency and its electromagnetic field distribution.

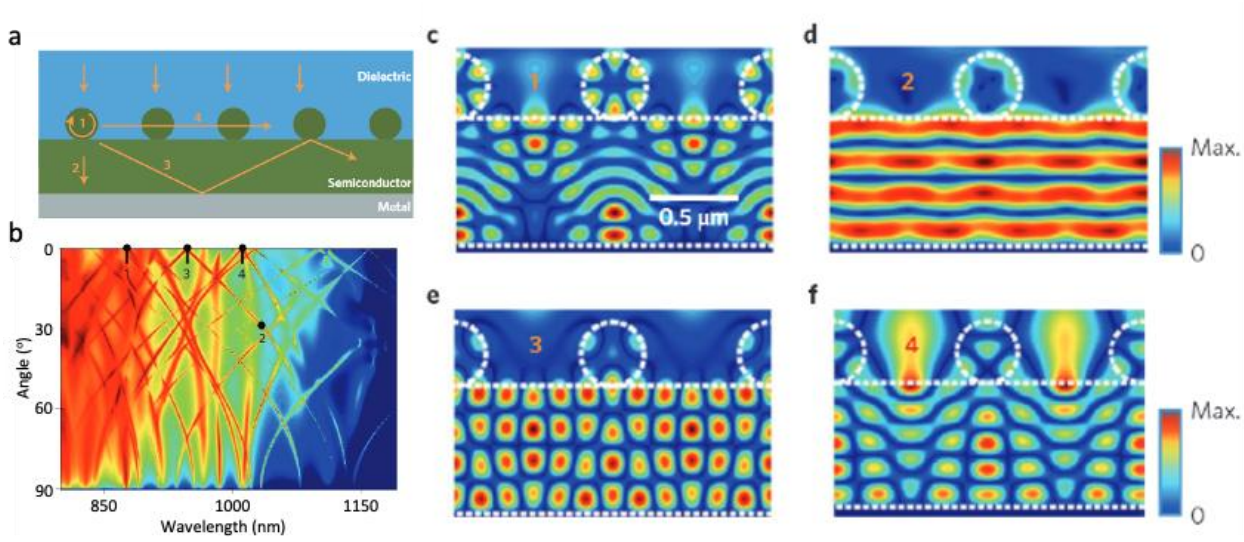

Figure 18. *Absorption enhancement of a thin solar cell with a nanostructured layer. (a) Scheme of the solar cell and the optical resonances involved. (b) Simulated absorption depending on the angular incidence and wavelength. Electric field intensity distribution for: (c) Mie-Guided resonance excited at λ= 881 nm; (d) Fabry-Perot resonance present at λ= 1031 nm and 28°; (e) guided mode excited at λ= 946 nm; (f) Diffracted quasi-guided mode excited at λ= 1011 nm.* [66]

The first studied mode (1) corresponds to a Mie resonance which enables a coupling to a guided mode, excited at $\lambda = 880$ nm. The Mie resonance can be characterized from the strong electric field distribution inside the nanowire, in this case with hexapolar symmetry (**Figure 18c**). This Mie resonance makes the nanowire an efficient scatterer to couple light into the silicon layer which will act as a waveguide. Therefore, this mode becomes a hybridized Mie-guided mode, with enhanced optical light path suitable for light harvesting. The second mode (2, **Figure 18d**) represents a Fabry-Perot resonance confined in the silicon film. As explained before, this

resonance strongly depends on the reflectivity on the interfaces of the thin film, in this case the backreflector and the silicon-air interface. Also, the wavelength at which it is originated depends on the optical thickness of the layer. The third and fourth modes (**Figure 18e and f**) correspond to angle-dependent modes derived from the diffraction produced by the nanowire array. In **Figure 18e** we can see how the array acts as a diffraction grating, ensuring phase match of the incident light to the guided mode of the silicon waveguide. In the fourth mode (4, **Figure 18f**), the diffraction mode does not present the same efficiency coupling to the silicon waveguide as the light is diffracted parallel to the surface, being quite possibly a RA.[56,67] However, some of the light is finally coupled to the interior of the active layer, providing enhanced absorption (2, **Figure 18b**). This kind of resonances and nanostructured layers has allowed to enhance the efficiencies of thin film and third generation solar cells.[1,9,68] In this thesis, we will use them to increase the efficiency in both solar cells and photodetectors in the near-infrared (NIR) spectrum.

1.3.5. Metal/dielectric interface resonances

1.3.5.1. Origin

In here we will detail the different resonances that may arise in the interface between a metal, which presents free electrons, and a dielectric, with bound electrons. The characteristics of the resonances will strongly depend on the wavelength. This is due to the fact that the permittivity of the metal, as introduced in **chapter 1.2.1**, presents different behaviors depending on the spectral range. The resulting interface resonances are also classified as surface or bound modes, in the sense that they inherently need the interface; they cannot exist in the free space. In all the cases that we explain, the impinging light has transversal magnetic polarization (TM), as according to Maxwell's equations, there are no metal/dielectric transversal electric polarization (TE) surface modes. For the existence of such surface modes, continuity of the momentum parallel to the surface (**eq.22**) of the light at the both sides of the interface must be satisfied (**Figure 19**):

$$k_{xd} = k_{xm} = k_{//} \qquad (22)$$

Where k_{xd} and k_{xm} are the parallel momentums of the light in the dielectric and in the metal respectively, and $k_{//}$ the propagation constant of the surface mode.

Imposing the previous condition, the propagation constant of the surface mode and the perpendicular momentum of the light (to the interface) of each media (k_{zd} (**eq.24**) and k_{zm} (**eq.25**)), will depend on the wavenumber k_0 and the relative permittivities of both the metal (ε_m) and dielectric (ε_d), following the next dispersion relation:

$$k_{//} = k_0 \sqrt{\frac{\varepsilon_m \varepsilon_d}{\varepsilon_m + \varepsilon_d}} \tag{23}$$

$$k_{\mathrm{zd}} = k_0 \sqrt{\frac{\varepsilon_d^2}{\varepsilon_m + \varepsilon_d}} \tag{24}$$

$$k_{\mathrm{zm}} = k_0 \sqrt{\frac{\varepsilon_m^2}{\varepsilon_m + \varepsilon_d}} \tag{25}$$

Analyzing the dispersion relation of a dielectric/metal interface (**eq. 23-25**), we can distinguish three differentiated types of electromagnetic resonances depending on the permittivities of both the metal and the dielectric. We will first have an insight on these resonances in the case of an ideal metal with only real permittivity and no losses (**Figure 20**), and then we will introduce losses into the metal, representing a more real system (**Figure 21**).[69]

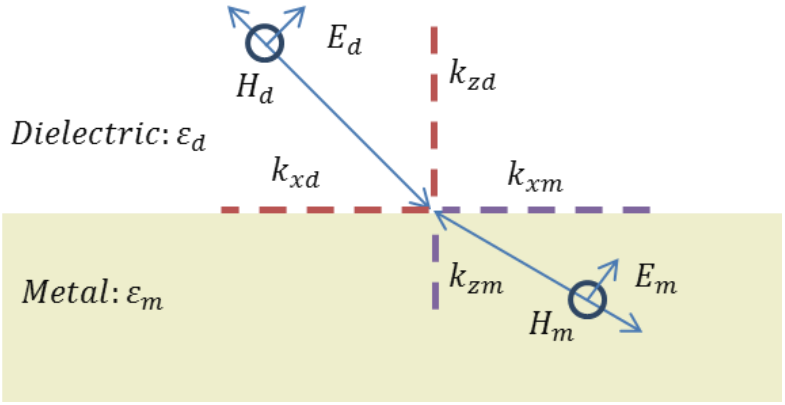

Figure 19. *Schematic illustration of the dielectric/metal interface studied. A transversal magnetic polarization (TM) electromagnetic wave impinges from a dielectric with permittivity ε_d into a metal with permittivity ε_m. The momentums of the light parallel (k_x) and perpendicular (k_z) to the interface in both media are also depicted.*

Ideal metal with $Im(\varepsilon_m) = 0$.

In this case, we are dealing with a metal with no losses (**Figure 20**). From the presented **equations 22 –25** we can derive that:

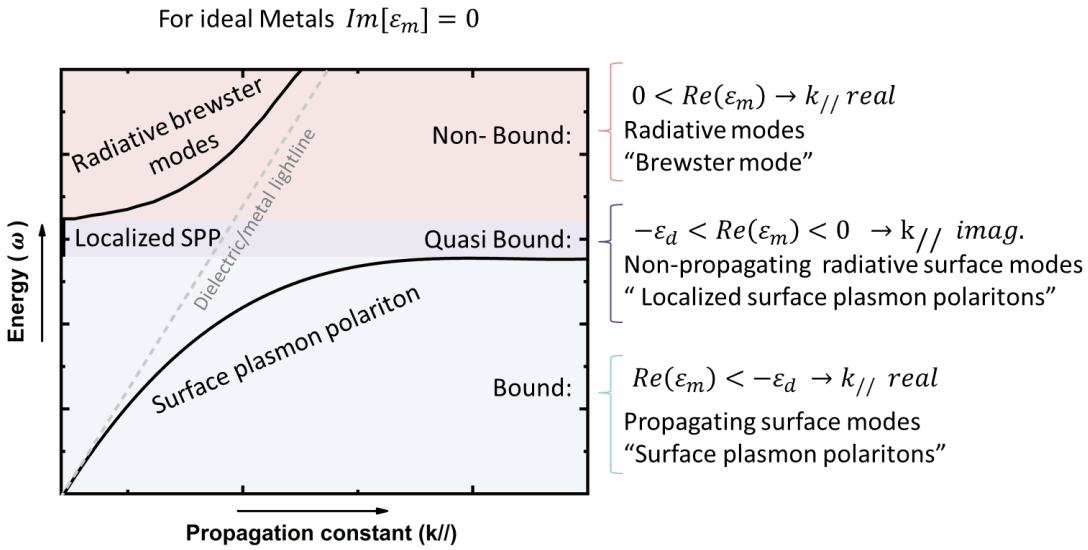

Figure 20. *Dispersion relation and summary of the electromagnetic modes present in the metal-dielectric interface for an ideal case in lossless media.*

- If $0 < Re(\varepsilon_m)$: above the plasma frequency (introduced in **chapter 1.2.1**), at high frequencies, the metal has the real part of the permittivity positive, and behaves like a dielectric. Both the propagation constant and the k_z are real. These are called Brewster[70,71] modes, and in the case of an ideal metal are not bound but radiative (**Figure 20** top).
- When $-\varepsilon_d < Re(\varepsilon_m) < 0$: just below the plasma frequency, the solution for the electromagnetic equation derives in a propagation constant imaginary (**eq.23**), which means that the modes do not propagate at all, they are localized. These modes are called to be in a quasi-bound regime as they are indeed surface modes, but with k_{zd} real (**eq.24**), they can be coupled from outside (**Figure 20** mid).
- If $Re(\varepsilon_m) < -\varepsilon_d$: the propagation constant turns to be real again, meaning that the mode indeed propagates (**eq.23**). This is the case of the well-known propagating surface plasmon polaritons. These modes are hybrid photon-electron excitations that travel in the interface, with exponential decay in the perpendicular direction to the interface. Because k_z is imaginary in both media, they are non-radiative (**eq.24-25**). This hybridization is composed of an electromagnetic wave present in the dielectric that is coupled with a longitudinal charge density of the metallic surface (**Figure 20** bottom).

Real metals with $Im(\varepsilon_m) \neq 0$.

Real metals, such as gold or silver, present losses and therefore $Im(\varepsilon_m) \neq 0$. In this case, the resulting modes for each condition are slightly modified (**Figure 21**). Thus:

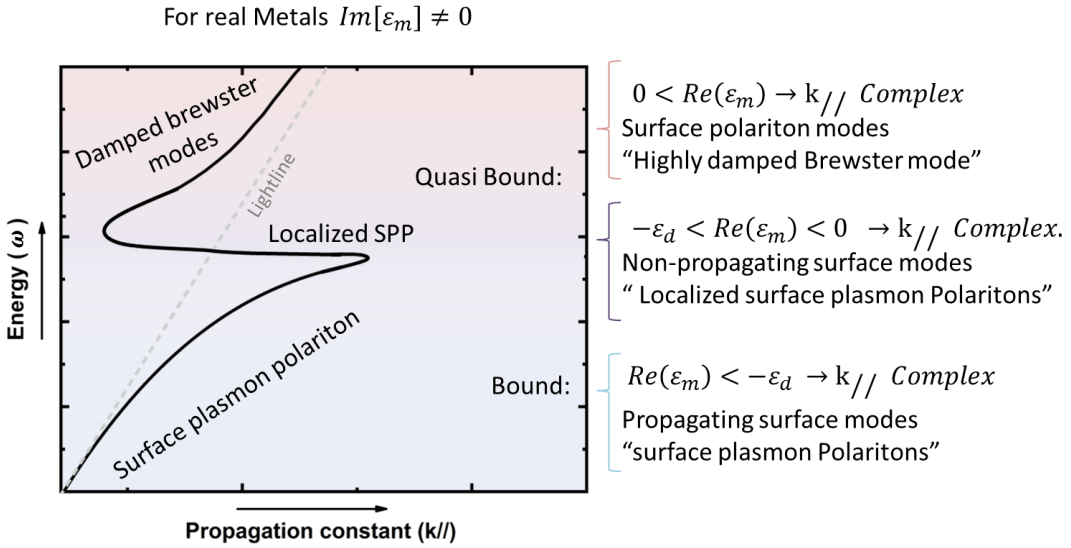

Figure 21. *Dispersion relation and summary of the electromagnetic modes present in the metal-dielectric interface for a system with losses.*

- If $0 < Re(\varepsilon_m)$: despite being above the plasma frequency, the metal does not act as a lossless dielectric. Therefore, the propagation constant becomes complex and the wave in the dielectric region becomes also evanescent (**eq.23-25**). In the case of strong losses, the Brewster mode turns to be a surface quasi-bound mode, a surface polariton, with a high damping (**Figure 21** top).
- When $-\varepsilon_d < Re(\varepsilon_m) < 0$: with losses, the localized SPPs acquire complex k_z in both media and become non-radiative, or pseudo-propagating if the losses are small (**Figure 21** mid).
- If $Re(\varepsilon_m) < -\varepsilon_d$: with the addition of losses, the propagation constant becomes complex. Therefore, the propagation lengths of the SPPs are limited; they become pseudo-propagating (**Figure 21** bottom).

1.3.5.2. Characteristics

From these three types of electromagnetic modes described in the metal/dielectric interfaces, the SPPs, when $Re(\varepsilon_m) < -\varepsilon_d$, are arguably the most interesting case for plasmonics. These are photon-plasmon excitations that travel along the interface with exponential decay in the perpendicular direction (**Figure 22a**). In the case of ideal metals, the SPP could theoretically propagate indefinitely in the surface along the parallel direction. However, in real metals with losses, the propagation lengths are limited. Interestingly, the SPP can be more propagating or more localized depending on the wavelength. At lower frequencies, the dispersion curve is closer to the light line, with higher group velocity, resulting in lower localization and more propagating behavior, reaching propagation lengths as large as 0.3 mm for gold and silver (NIR range) (**Figure 22b**). On the other hand, at higher frequencies the velocity group is lower, resulting in more confined fields and a less propagation behavior of the wave, with propagation lengths below 100 microns (VIS range) (**Figure 22b**).

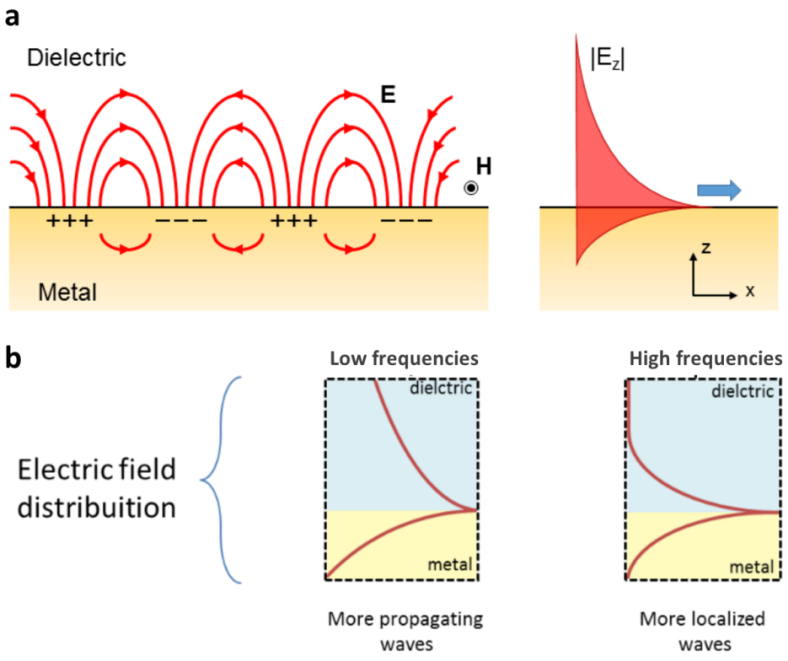

Figure 22. *(**a** left) Combined electromagnetic and charge density waves of surface plasmon polaritons propagating at the metal-dielectric interface. (**a** right) Decay of the perpendicular electric field intensity inside the dielectric and the metal. (**b**) Electric field distribution of surface wave inside the dielectric and metals depending at high and low frequencies (inside SPP range).*

Therefore, the SPP can efficiently confine and squeeze the electromagnetic field beyond the diffraction limits. As presented in the dispersion relations, the SPPs, commonly with the guided

modes, are non-accessible from air due to a propagation constant mismatch. To excite the SPPs, additional $K_{//}$ is provided with a prism coupler, either using the Otto or Kretchmann configuration, or a diffraction grating, among others.

The modes in the quasi-bound range with $-\varepsilon_d < Re(\varepsilon_m)$ have different characteristics. These modes can be accessed from air as they are inside the light cone. As introduced in **section 1.2.1**, as the frequency goes higher, the electric field can penetrate the metal. With the presence of losses, the propagation constant becomes complex (**eq.23**) and the wave in the dielectric becomes evanescent as well, as k_{zd} becomes complex (**eq.24**).

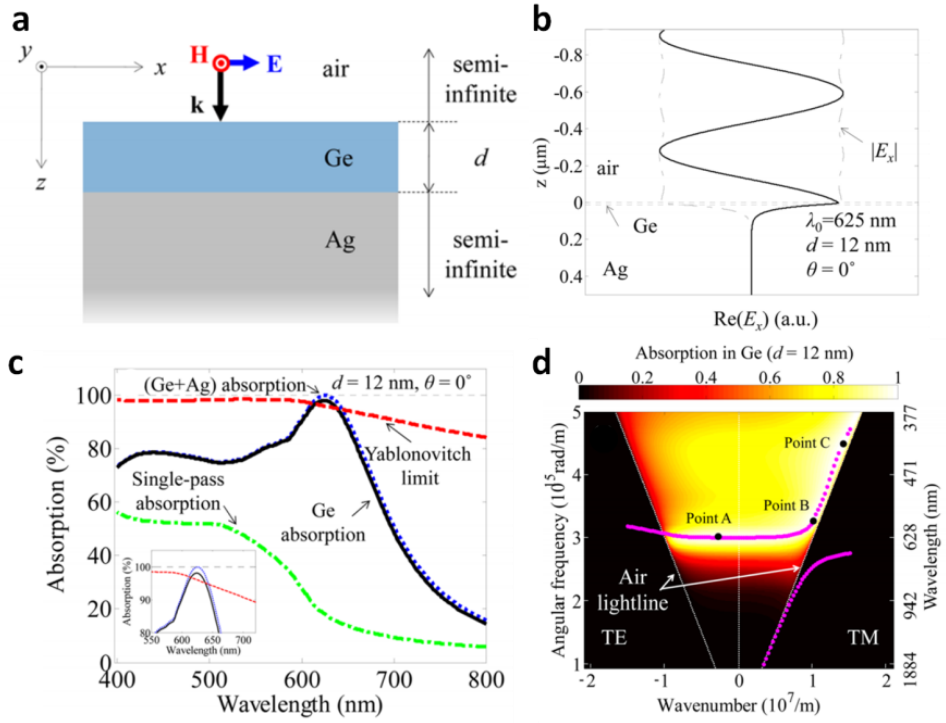

Figure 23. *(**a**) Schematic diagram of air/Ge(12 nm)/Ag Gires-Tournois interferometer. (**b**) Transverse electric field (x-component) distribution for the air/ Ge(12 nm)/Ag case with λ_0 = 625 nm. Solid line: Re(Ex); dash-dotted line: |Ex|. (**c**) Absorption spectrum for the normal incidence. Dashed red line: Yablonovitch limit; dotted blue line: absorption in Ge (semiconductor) and Ag (metal); solid black line: absorption in Ge; and dash-dotted green line: single-pass absorption. (**d**) Absorption in the Ge (12 nm) layer (in the color map) with the mode dispersion. In the solid magenta line we can observe both the SPP branch at low frequencies and the flat damped Brewster modes at higher frequencies.*[72]

Research studies of the groups of Federico Capasso[33] and Mark Brongdersma[72] recently showed that this non-ideal behavior of the metals at visible frequencies, in the quasi-bound range, combined with the deposition of a thin film of a high refractive index material atop (i.e. germanium), can lead to strong thin film interference effects with thicknesses lower than the ones predicted in **chapter 1.3.1** (**Figure 23a, c**). Differently to an ideal metal or perfect electric conductor (PEC), the electric field can slightly penetrate the metal (**Figure 23b**), generating a phase shift superior to π and leading to destructive interferences of almost unity absorption will lower thicknesses than in regular Gires-Tournois interferometers.[25] The strong losses of the germanium layer allowed to couple to surface Brewster modes, which are usually leaky but become surface quasi bound modes in the presence of strong losses; with a flat dispersion curve, which accounts for an almost omnidirectional absorption (**Figure 23d**). This type of electromagnetic modes will be further discussed in **chapter 3**.

1.3.5.3. Uses and applications

SPPs have been widely studied and used in a broad spectrum of applications, such as surface enhanced Raman spectroscopy (SERS)[73], metamaterials[74], solar cell harvesting[75], enhancing nonlinear processes[76], photocatalysis[77] and other fields where a near field enhancement is needed. In this thesis though, we will also take advantage of the Brewster modes present in the quasi bound regime. If designed properly, they can be of use in characterization applications[78] and in super absorbent thin films[72] with promising future in light harvesting technologies.

In this thesis we develop nanostructured devices for light managing, including superabsorbers, metasurfaces, light harvesting devices and light emitting platforms that exploit the resonances introduced in this section. We do so always trying to keep an applicative point of view, using scalable nanostructuring methods that are provided in the next chapter.

Chapter 2:

2. Experimental section

In this chapter I describe the most relevant techniques used in this thesis. Specific recipes are given in each chapter for each material.

2.1. Deposition methods

2.1.1. Spin coating

This simple and yet powerful deposition procedure has been widely used in this thesis to obtain thin films onto flat substrates. In this technique, a small amount of a fluid material is initially casted in the center of a flat substrate. The substrate is then set to rotate to spread the coating material uniformly. The centrifugal force spreads the casted fluid and removes the excess material through the edges of the substrate. The final thickness of the obtained thin film depends mainly on the spinning velocity applied and the viscosity of the casted material. Depending on the spinning time applied, we can evaporate all the solvent resulting in a dry film or have a yet viscous film. Obtaining a viscous film has been the preferred option on many of the spin coating procedures employed along this work because it facilitates the nanopatterning of thin films of known thickness of the casted material through solvent assisted nanoimprint lithography, which will be explained in the following sections. In this thesis we used a SPS POLOS 150i spin coater to obtain thin films of a wide range of resists, pastes and polymers onto glass and silicon substrates.

2.1.2. Thermal evaporation

In thermal evaporation, a solid source material is thermally evaporated inside a vacuum chamber (10^{-6} Pa) ejecting molecules of the source material that travel towards the substrate. These condensate and re-solidify onto the substrate surface where they nucleate and coalesce creating a film of the material. This deposition is mainly used in this work to evaporate metal layers, either to generate electric contacts, efficient diffraction gratings and plasmonic substrates.

2.1.3. Molecular beam epitaxy of germanium films

Molecular beam epitaxy (MBE) is a deposition technique similar to the before explained thermal evaporation in which the molecules of a source material are evaporated and deposited onto a substrate after crossing a vacuum chamber. The essential differential aspects are a higher vacuum quality, at least of 10^{-8}Pa, and a low deposition rate. Often, this technique is complemented with a RHEED system (reflection high-energy electron diffraction) which enables the control of the thicknesses up to the monolayer level. This control on the deposition conditions and the growth rate leads to the possibility of achieving epitaxial growth, a key factor in many semiconductor devices.[79] In this work MBE has been used to evaporate Germanium over a gold film with great control over the thickness, to match the designed specifications, in a project where controlling the thickness of the semiconductor was of essential relevance, as we will see in **chapter 3**.

2.1.4. Chemical vapor deposition of silicon

The chemical vapor deposition (CVD) is a fabrication method employed to obtain conformal high quality coatings, mainly of semiconductors. In a reactive chamber initially under vacuum, the substrate is exposed to the precursors in vapor state of the materials that have to be deposited. These react with the surface of the substrate and are deposited, being chemically linked with the surface. The essential feature of this technique for which it has been employed in this thesis is for the isotropy of its deposition.[80] Both thermal evaporation and MBE are highly directional deposition methods, which are perfect for some experiments conducted, but in some cases we needed the conformal deposition offered by chemical deposition methods such as CVD. More specifically we conducted low pressure and low temperature CVD of silicon using Si_2H_6 as the precursor in **chapter 4**. With this method we are able to obtain silicon hemispheres on top of a pillar array, something not possible with directional deposition methods. This work was carried out at the ICMM in collaboration with Prof. Cefe López and Prof. Álvaro Blanco.

2.2. Nanoimprint lithography (NIL)

2.2.1. Introduction to NIL

The working principle of nanoimprint lithography stands over a concept widely used in other type of lithographies and manufacturing techniques: transfer the features of a previously

patterned mold to a desired substrate by applying pressure.[81] This easy concept, feasibly performed by a toddler shaping its colored plasticine has been optimized up to the point to obtain nanometric features with high fidelity. It is from the simplicity of the procedure that its main advantages arise. On the one hand, the mechanical nature of the process offers the possibility to cut the costs to a minimum, compared with other high resolution techniques which depend on complex optical setups and guided electron beams. This leads to a drastic increase in the scalability of this technique. On the other hand, the same mold can be re-used several times. These two characteristics make it appealing for industrial application, because it allows the nanopattern of large surfaces to be repeated seamlessly. This technique has been optimized to the point of being compatible with roll-to-roll methodologies, where a continuous pattern is imprinted by a rotating mold over a flat surface. Another advantage of NIL is that it is not diffraction limited like optical lithographies. With a proper designed mold and substrate, resolutions down to few nanometers can be achieved, similar to much more complex and expensive nanofabrication techniques.[82] Finally, the nanoimprint lithography is a versatile technique in a sense that has a wide range of materials that can be patterned.[83] They do not require to be radiation sensitive, nanometrically flat nor of a specific composition. As we will observe along this work, it mostly requires a substrate that is viscous in a certain point in time, when it is patterned, and that can be hardened or solidified afterwards to keep the acquired features. This makes it a promising technology for the direct patterning of essential layers in the fabrication of devices with almost no disruption of the fabrication scheme. In most of the cases there is no need to add extra specific resists or sacrificial layers neither to transfer the features with etching techniques. Avoiding these additional steps often leads to a less aggressive implementation of the structures, rendering better performances of the final devices. These qualities have lead NIL to be used not only in semiconductors but also in flexible organic devices, biocompatible materials and other unconventional materials[84–87], rendering applications in solar cells[1], metamaterials[88], nanofluidics[89] and nanoelectronics.[90]

Since the NIL technology arose in 1995 by the hand of Stephen Chou et al.[91], numerous are the variations of this versatile technique that have been developed to fit specific materials or necessities. The two major aspects that have been diversified and optimized are the composition of the original molds and the implementation methodology of the nanoimprinting. Next we detail the type of molds and methodologies that we have used along the development of this work.

2.2.2. Nanoimprinting methods

2.2.2.1. Thermal nanoimprinting lithography (tNIL)

This is the original technique developed by Chou et al in 1995.[91] Its main procedure scheme is similar to that used for patterning old wax stamps. First, a thermoplastic material is heated above its glass transition temperature. This reduces drastically its storage modulus, in other words, makes it viscous and malleable. Therefore this material can be easily patterned by pressing it with the structured mold (**Figure 1a**). Often, when the imprinted material gets viscous enough, no additional pressure other than the own weight of the mold is needed. After the imprinting step the sample is cooled down to regain its stiffness. The demolding is done when the imprinted material is cold enough, below the glass transition temperature. When the mold is lifted, it leaves the negative features on the patterned material (**Figure 1c, d**). One must point out that the correct development of this last step has been found to be crucial to reproduce faithfully the features. A carelessly lift-off of the mold often leads to disruption of the imprinted nanometric features.

Thermal NIL, also known as "hot embossing", is optimum for the patterning of thermoplastic materials such as many resists, organic polymers, biocompatible materials and biomolecules; with glass transitions around 100°C.

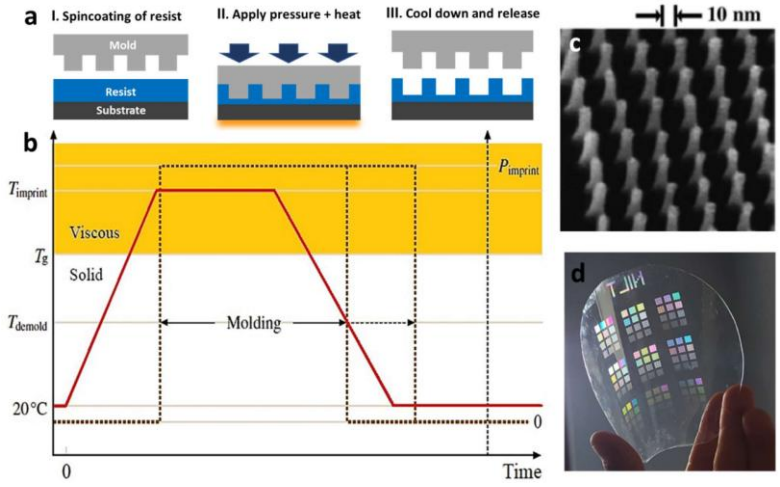

Figure 1. *Schematic of thermal nanoimprinting process and some examples. (**a**) Steps and elements involved in the tNIL proccess. (**b**) Schematic of pressure, temperature and state of the imprinted material during a the process. (**c**) SEM of 10 nm pillars array in PMMA.*[82] *(**d**) Wafer scale patterned TOPAS films.*

2.2.2.2. Solvent assisted nanoimprinting lithography (sNIL)

The solvent assisted nanoimprinting, as the name implies, requires a solvent for the patterning of the material. The solvent brings viscosity to the material layer previous to the nanoimprinting with the mold. The mold is pressured while the layer of the material is still wet and viscous, so it can adopt the negative features of the stamp. With or without the aid of external heat, the solvent is evaporated. Therefore, the nanopatterned material re-hardens with the desired features. Subsequently the mold is carefully removed.

This nanoimprinting procedure is often combined with solution process techniques like spin coating or blade coating, as these techniques offer the possibility to obtain the material layer still humid, prior to complete drying. The humidification of the material can also sometimes be obtained by simple drop casting of the proper solvent into the layer before imprinting. This technique is especially useful with materials which are really difficult to process when dry, but easily malleable when still wet, such as inorganic pastes.

2.2.2.3. UV-nanoimprinting lithography (UV-NIL)

This procedure is quite similar to the previous two, but makes use of a photosensitive material. After the imprinting, the material is hardened by the exposition to UV light causing polymerization (**Figure 2**). This requires that at least one of the sides of the sample + mold system to be transparent to these wavelengths (typically UV). Hence, a mold made of quartz or transparent silicone is used. The advantage of this approach is that it can avoid the formation of cracks that may arise due to the possible thermal expansion in the tNIL and during the drying in sNIL. It also comes quite handy when a nanostructure must be transferred at room temperature because of thermal sensitivity of the material.

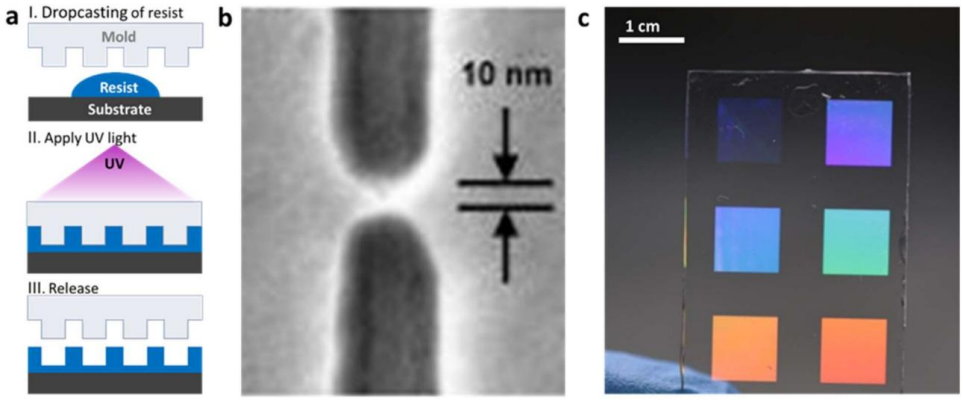

Figure 2. *Schematic of UV-NIL process and some reproduced examples. (**a**) Process steps and elements involved. (**b**) High resolution 10 nm features.*[92] *(**c**) Centimeter scale nanometric patterns fabricated in Ormostamp (a UV photocurable resist) on glass.*

2.2.3. Type of nanoimprinting molds

2.2.3.1. Hard molds

The "hard" nanoimprint lithography uses rigid molds made of materials such as silicon and quartz, with inherent large young modulus, usually in the order of GPa. This molds offer a super high resolution down to few nanometers, but it comes at a cost.[82] Due to the lack of flexibility of the molds, bubbles might get trapped between the mold and the substrates. To expel the bubbles from this interface, usually high pressures are used. With high pressures and rigid molds, any submicron impurity present may seriously damage and break both the substrate and the mold. That is why this technique is often performed under clean room conditions. Additionally, with hard molds, the demolding process becomes more critical and often requires additional tools or additional steps.

In this work we will not use the hard molds to nanoimprint materials in the final substrates. We will use patterned silicon wafers as initial masters from which we will generate the soft and hybrid molds that will be explained in the next section.

Fabrication procedure

The original patterned silicon wafers, or masters, were purchased from nanofabrication specialized companies, in this case EULITHA (Switzerland) and NAITEC (Spain). These masters are fabricated through electron beam lithography, interference lithography and deep UV lithography. This original master can be replicated with nanoimprinting many times, enabling the production of hundreds of replicas, which at their time can be used for hundreds of replicas more. The fabrication of the master is a one-time step that provides the initial cornerstone for the later industrial scalability. In this work we have obtained arrays of holes in silicon substrates with lattices ranging from 200 to 2000 nanometers in $1cm^2$ areas each (**Figure 3a**).

To get the silicon master ready to be replicated, the first step is to silanize it with an anti-sticking layer of perfluorooctyl-trichlorosilane. This antisticking layer prevents the adhesion of the silicones and resists during the replication, avoiding the rupture of the fragile silicon master during the demolding. The silicon masters are left in a vacuum chamber for 30 minutes with 5μl of the 1H,1H,2H,2H- perfluorooctyl-trichlorosilane (97% merk). In this process, the evaporated silane molecules covalently bond to the silicon surface. Ideally, only one single layer of perflorooctyl-trichlorosilane is deposited onto the silicon surface. To remove the excess of silane, the substrates are rinsed with acetone and heated to 150°C for half hour. This is a crucial

step because too much deposition of silane ends up smoothing the features of the master, but an incomplete coverage of the silicon surface may cause the silicones and resists to stick permanently, ruining the pattern.

By making a hard mold negative replica of an original master, one can obtain a master to replicate the negative features (**Figure 3b**). This will be replicated with Ormostamp resist (Microresist technology), a photocurable polymer with high young modulus (650MPa) suitable to replicate fine structures with high aspect ratio and excellent mechanical stability. Therefore, we will obtain a hard mold or master with the negative pattern, which will give place to soft molds with the original features, which can be used to pattern the negative pattern in the final devices (**Figure 3c and f**).

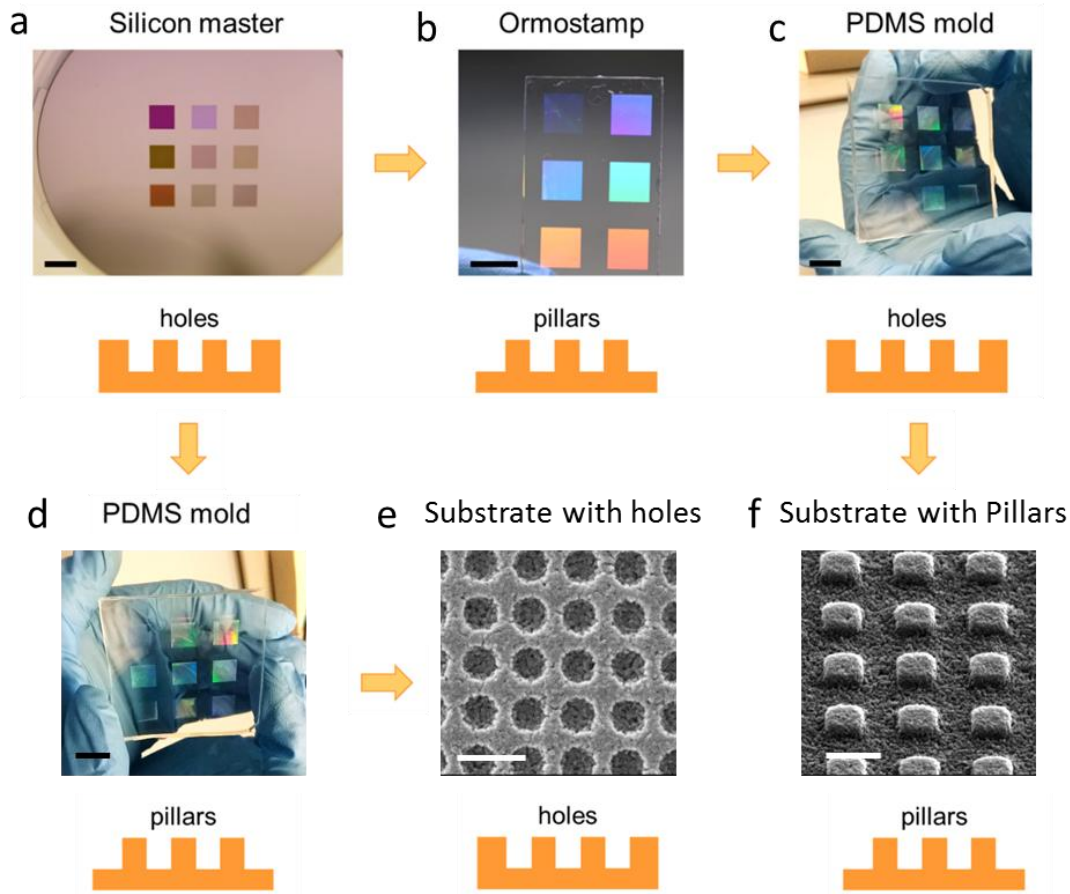

Figure 3. *Scheme of the replication process from the original silicon master with holes (**a**). One can replicate to another hard mold of Ormostamp (**b**) to obtain a PDMS mold with holes (**c**) to imprint pillars in the final substrate (**f**); or directly obtain a PDMS mold with pillars (**d**) to imprint holes in the substrates (**e**). Scale bars are set to 1cm in macroscopic images and 1μm in SEM images.*

To obtain the negative masters we use a type of hard UV-NIL approach as explained in **chapter 2.2.2.3**. A drop of Ormostamp, a photosensitive resist, is droped onto the already silanized silicon master. Then, a previously cleaned glass slide is gently pressed on top making sure no bubble is trapped inside. Once the photoresist is spread over the substrate it is UV cured for 5 minutes to cross link and harden. In this way, we obtain the negative hard mold. To demold the Ormostamp master, we place it in a hot plate increasing its temperature up to 160°C and it eventually detaches from the silicon master. This is due to a difference in the thermal expansion of the two materials. Again, to use this newly produced Ormostamp master, we have first to silanize it as explained before. In this case, though, we will rinse it with isopropanol, as acetone has been found to induce the detachment of the photoresist layer from the glass.

2.2.3.2. Soft Molds

The soft molds, used for the so called, soft nanoimprinting[2], are mainly made of silicone elastomers such as polydimethylsiloxane (PDMS) or plastic materials such as polyethylene terephtalate (PET). These molds, flexible and usually with poor chemical interaction, can overcome the majority of the issues that arise when using hard molds. Their flexibility provides a better surface contact and lower chances to harm the substrate. This enables nanoimprinting curved and irregular surfaces.[3] It also means that soft NIL has a higher tolerance to impurities and imperfections present in the substrate and/or the molds, rendering the possibility to work outside cleanroom facilities, lowering production costs. At the same time, the poor chemical interaction with the substrates and the possibility to bend the mold for the extraction makes demolding process easier. These characteristics make the whole process much more scalable and more roll-to-roll compatible, one key feature for the industrial implementation. However, since the young modulus is low (around 2MPa), the aspect ratios that can be achieved are limited. Beyond specific aspect ratios for a material, the structure collapses, becoming unusable.

The soft molds have been only used in this thesis to reproduce patterns with lattice parameters above 700nm, with holes of 300nm. As the aspect ratios of the structures used was around 1, smaller lattice parameters might have led to structural collapse. They were made of polydimethylsiloxane, Sylgard 184, also called soft PDMS (sPDMS), a thermo curable transparent flexible silicone.

Fabrication procedure

The soft PDMS used in this thesis was purchased from Dow Corning. First, a 10:1 mixture of the prepolymer and curing agent are mixed vigorously and left degassing for approximately an hour (the degassing time depends on the amount of material). Then the mixture is gently poured onto the master, either silicon or Ormostamp, and left degassing under vacuum for another hour, to ensure a complete filling of the structures. Next, we cure the polymer by heating it to 100°C for another hour. Once the sPDMS is cured, we detach it carefully from the master.

2.2.3.3. Hybrid molds

The hybrid molds were developed as an intermediate solution between hard molds and soft molds, trying to preserve the best qualities of each one. In a hybrid mold, a few micrometer thin layer of a hard material which possesses the structure is supported by a much larger thick backbone of a more flexible material. Hard materials can become flexible when sized down to micrometric thin layers, while the high young modulus enables high aspect ratio features.[4,93] The flexible backbone ensures mechanical stability for handling and optimum demolding. This approach provides high resolution down to few tens of nanometers but maintains its scalability for industrial application.

The hybrid molds have been used in this thesis to reproduce patterns with lattice parameters down to 200nm, with holes of 100nm. They are a composite were the structured layer, with a thickness of few microns is made of hard PDMS (hPDMS) and the backbone of several millimeters is made of sPDMS. The hard PDMS is an elastomeric silicone similar to soft PDMS with a young's modulus 5 times larger than soft PDMS (around 10MPa) designed to reproduce larger aspect features.[94]

Fabrication procedure

The hPDMS is a mixture done with a kit purchased from Gelest (USA). First, we mix 1.7g of the vinyl prepolymer (7-8% vinylmethylsiloxane) with 9µl of the catalyst (Platinum divinyltetramethyldisiloxane), 50µl of the modulator (1,3,5,7 – tetramethylcyclotetrasilane), 0.5g of the hydrosilane polymer (hydroxyl siloxane) and 2ml of toluene (69% wt) in sequential steps, always under stirring. This gives a solution that will solidify in approximately 20 minutes, as the toluene evaporates. While it is liquid, the mixture is drop casted onto the master and spread by blowing air on it. This step also ensures that the mixture covers entirely all the structures and leaves no microbubbles trapped. After repeating this last step twice or thrice, when all the

substrate is fully covered, it is left 1h at room temperature for drying and 1 more hour at 60°C to cure the hPDMS. Finally a backbone of sPDMS is casted on top with the same procedure explained in the previous section.

2.3. Dry etching

2.3.1. Reactive ion etching (RIE)

The RIE is a dry etching technique used in micro and nanofabrication which combines both physical and chemical etching. In this process, the desired substrate is placed in a low pressure chamber, where a plasma is generated. Then, thanks to a strong voltage difference, the plasma ions gain kinetic energy and are guided to impact the surface of the substrate where they react with the surface and etch the material. Thanks to the directionality of the electric field that guides the ions to the substrate, the RIE can provide a highly anisotropic etching, in contrast to wet etchings. At the same time, as the etching reaction is chemically mediated, the RIE offers a fairly selective etching if the plasma composition is correctly chosen. It is always tried to maximize the ratio of etching of the final substrate against the etching of the mask with the initial pattern, usually a resist. In this thesis it has been used to transfer a pattern of holes from a Shipley resist into a thin film of germanium using a $SF_6/CHF_3/O_2$ mixture in **chapter 3**.

2.4. Characterization of the samples

After the fabrication of the nanostructures, the samples are characterized topologically, optically and electronically (if required) with the following techniques:

2.4.1. Topological characterization methods

2.4.1.1. Scanning electron microscopy (SEM)

The scanning electron microscopy gives us an almost nanometric resolution of the topography of the fabricated samples and it is routinely used during this doctoral work. The secondary electrons will give us a more detailed information on the structure while the backscattered will give us a hint on the composition. This later will be especially useful to distinguish between layers of different materials of the same device. We have used a Quanta FEI 200 FEG-ESEM

microscope. For conductive substrates, or with fairly good conductivities, we have used the high vacuum mode (10^{-3} Pa) and voltages ranging from 10 to 15KV. In the other hand, for poorly conductive substrates, low vacuum conditions with a 60Pa water vapor atmosphere and voltages form 5 to 10KV were used to avoid aberrations due to the charging of the surface.

2.4.1.2. Profilometry

We have used contact profilometry to determine the thickness of the thin films deposited. The equipment used was a KLA Tencor D-500 profilometer. A diamond tip in contact with the substrate with a specified contact force (in our case 0.03mg) scans the sample horizontally (in our case 0.1mm/sec). It can measure the scanned features with almost nanometric vertical resolution and submicrometric lateral resolution. Generally, we cleanly scratch the film down to the substrate and we measure the height difference generated. It has been extensively used as a previous step to the nanostructuration to know the deposition conditions that would give us the desired thickness of the material to be patterned. Also, it has been used to make correlations studies between the thickness of the active layers and the final performance of the optoelectronic devices.

2.4.2. Optical characterization

2.4.2.1. Fourier Transform Infrared spectroscopy (FTIR)

Generally the first step to verify the optical properties of the fabricated nanostructure is to measure the reflectance and/or transmittance in the visible and near infrared with the FTIR from 400 to 2500nm. The equipment used was a Bruker Vertex 70 FTIR spectrophotometer attached to an optical microscope (Bruker Hyperion). This allowed us to control visually the position in which we were taking the measurements. The spectra were recorded using 4x objectives with numerical aperture (NA) of 0.1, for both emission and collection, having a spot size of $400\mu m^2$. The reflectance measurements were normalized against silver and gold mirrors, for visible and infrared ranges respectively, and a cleaned glass slide for the transmission measurements.

2.4.2.2. Angle resolved spectroscopy

The angular-dependent transmittance was recorded in an optical table with a double rotation stage setup using as incident beam a halogen lamp (Ocean Optics HL-2000-HP_FHSA). Transmitted and emitted light was detected with a fiber-coupled spectrophotometer (Ocean

Optics USB2000+VIS_NIR_ES). We used angular resolved spectroscopy measurements to observe the angular dependence of diffraction modes. It has also been proven helpful to distinguish the origin of certain extinction peaks, as, for instance, the Mie modes are angle invariant and the diffractive modes strongly depends on the angle. Some of the angle dependent measurements were carried out in the ICMS by the group directed by Prof. Hernán Míguez.

2.4.2.3. Photoluminescence measurements

In **chapter 5.4** the photoluminescence (PL) measurements were performed in the same setup as the angle resolved spectroscopy, but using a 285 nm LED (FWHM = 13 nm, power = 50 mW) as the excitation source. In **chapter 4** the PL is excited by focusing a Ti:Sapphire laser (Chameleon model by Coherent, 1 kHz repetition rate, 150 fs pulse width, whose emission is bandpass filtered around 680 nm) through a 5 cm focal length lens. The average power impinged on the sample was 500 μW. The dye emission was collected by the same lens in illumination/collection geometry. After filtering the laser contribution, the PL is coupled into an optical fiber and alternatively connected to a compact spectrometer (USB 2000, Ocean Optics) to obtain the spectral information. The spectrally resolved PL measurements enables us to see how the structures that we fabricate affect the emission of light, whether is producing more efficient outcoupling of generated light, or if it is acting as an antenna, increasing the Purcell factor of the emitter.

2.4.3. Electrical characterization of photodetectors and solar cells

2.4.3.1. External quantum efficiency measurements (EQE)

The external quantum efficiency is defined as the ratio of the incoming photons, which are transformed to electrons to the external circuit current measurement. Its measurement enable us to correlate the efficiency on converting incident photons to collected carriers of the solar cell or photodetector fabricated. Moreover, as it is measured as a function of the wavelength, they can be directly correlated with the optical characteristics measured. This ensures that our photonic structures generate a change in the optical characteristics which finally enhances the electrical properties, being able to pin point at which wavelengths this enhancement occur. The EQE setup used in **chapter 5.3** consists of a Supercontinuum White laser (Fianium PM-SC) coupled to a Fianium monochromator (LLTFContrastTM), with the power calibrated by a broad-band silicon photodetector (Thorlabs S120V 200-1100 nm 50 mW). The setup is enclosed on a

black box, to prevent any light from affecting the measurement. The EQE wavelength scan was done from 400 nm to 1100 nm every 2.8 nm followed by a no-light measurement of the dark current of each device. In **chapter 5.2** EQE spectrum were acquired on a QuantX-300 quantum efficiency measurement system (Newport) where white light from a xenon lamp was chopped at a frequency of 25 Hz.

2.4.3.2. Intensity-Voltage measurements

The intensity-voltage measurements (J-V) allows to extract the main figures of merit of the solar cells such as the open circuit voltage (V_{oc}), the short-circuit current (J_{sc}), the filling factor (FF) and the power conversion efficiency of the device (PCE). The *J-V* was acquired under a simulated AM1.5 solar spectrum. The input power density was adjusted to 1 sun using a NIST-traceable calibrated reference cell (Newport 91150 V). The lamp spectrum was measured using irradiance-calibrated spectrometers (USB2000 and NIR512, Ocean Optics).

2.5. Simulation methods

One cornerstone of this thesis has been the ability to predict and reproduce the optical response by means of optical simulation software. This allowed to identify and verify the origin of the optical features measured and predesign the optimal structure for each application.

2.5.1. Finite domain time difference method (FDTD)

The numerical calculations were performed using Lumerical FDTD solutions (www.lumerical.com). FDTD is a powerful tool to solve Maxwell's equations over time in a volume. It works by discretizing the space in the so-called Yee cells, and the time into time steps with a leapfrog algorithm. The Maxwell's equations are solved for each cell at each time step until a steady state is reached. In our simulations, a linearly polarized plane wave source impinges a unit cell with periodic conditions with perfect matching layers above and below the substrate. Then transmission, reflection and electromagnetic profiles are obtained with profile and power monitors. The size of the mesh delimiting the discretization of the spatial cells depended on the minimum feature size of the architecture and the material simulated. In this thesis we have used mesh sizes of around 2-5 nm for the nanometric features and 10 nm in the regions without nanometric features. The simulated architectures reproduced the geometrical parameters extracted from SEM micrographs of the samples. The refractive indexes were

extracted from ellipsometry data for the PbS quantum dots, the germanium and the PBTTT:$PC_{71}BM$ and P3HT: $PC_{60}B$. Silver and gold were extracted from Johnson and Christy[95], and indium tin oxide (ITO)[96], zinc oxide (ZnO)[97], titania (TiO_2)[98], silicon[99] and Molybdenum trioxide (MoO3)[100] were extracted from known databases. For mesoporous materials such as mesoporous titania (m-TiO_2) we used a Bruggerman effective medium approach.

Chapter 3:

3. Light confinement in ultra-thin films

3.1. Introduction

The prospect of an efficient clean energy source and the need of converging light speed data transfer with current electronic systems push the scientific community into developing more economic and efficient ways to convert light into active electrons.[101] A first step to do so is to optimize the thickness of the active layer of the device to capture the maximum number of photons from the optical spectrum. In current crystalline silicon solar cells, thicknesses up to 300 µm provide the best performing devices.[102] However, not all photovoltaic (PV) technologies can afford such widths due to low mobility carriers[102,103] or expensive raw materials.[104] Diffusion lengths and recombination times limit the thickness and efficiency of many optoelectronic devices. A compromise between total absorption and conversion efficiency often needs to be reached.[101] Light trapping schemes[105] play a major role in balancing out optimum thicknesses for charge extraction and efficient light absorption.[66] The ultimate goal of a light trapping strategy is to provide maximum absorption of light in a broad spectral range while using the minimum amount of photoactive material. Traditional wafer based technologies have extensively exploited light trapping strategies up to a point where the classical limit of light trapping[106,107] is almost reached.[108] This upper limit for light trapping was demonstrated, by Eli Yablonovitch, to be $4n^2$, where n is the refractive index of the material. Nonetheless, this light trapping upper limit is reserved only for classic optically thick systems with ray-based optics. There is, however, an increasing interest in further decreasing the thickness of the active layer below the micron, where the light trapping schemes and its limitations cannot be based in traditional ray optics and have to be adapted to the electromagnetic wave behavior of light. This increasing interest arises from the fact that for devices with submicrometric to few micron active layers new properties appear for classic materials (such as flexibility for silicon[109]) and new materials like plastics[110] or nanocrystals[111,112] can be used at lower processing costs. Emerging PV based in perovskites, quantum dots or organics materials with promising prospects to compete with the well-established silicon PV technologies use active material thicknesses often below few microns. Capturing light in such thin devices require redesigning the strategy, moving

away from traditional ray optics approximations into the wave optics regime.[66] Many wave optics based designs are being currently investigated; photonic crystals,[113,114] plasmonics[115,116] and microresonators[1,117,118] provide new and exciting means of confining light in sub-wavelength thin films. Nevertheless**,** strong absorption enhancements are not restricted exclusively to the above-mentioned photonic architectures. Following, we will describe and study a case where strong absorption in nanometric flat semiconductor films is achieved with a simple Gires-Tournois design that will be a cornerstone of the work developed in this chapter.

3.2. Visible optical absorbers based on strong interference in ultra-thin films

In 2013, the group of Prof. Federico Capasso[33] demonstrated that flat nanometric films (up to 25 nm) of amorphous germanium (a-Ge) achieved 90% absorption broadband peaks in the visible range when deposited on optically thick gold films. Later, in 2014, the group of Prof. Mark L. Brongdersma demonstrated the capability of such architecture to surpass the Yablonovitch limit in silver substrates. Simply put, nanometric semiconductor coatings on metallic films act as Gires-Tournois interferometers, an asymmetric Fabry-Perot resonator where one of the interfaces is metallic.[25,119] The system used can be understood as an asymmetric waveguide coupled to a resonator or cavity (**Figure 1a**). To determine the condition of total absorption for this layered system, we must find the condition for critical coupling of the waveguide to the resonator[120], i.e., no reflection to the input and no transmission to the output of the waveguide. This becomes possible by perfect coupling of incident light into the optical modes of the resonator (or equivalently, by a destructive interference of light in the outside medium). The thickness of the semiconductor layer determines the position of the minimum in the reflectivity (maximum in absorption) of classical Fabry-Perot resonances (FPR).

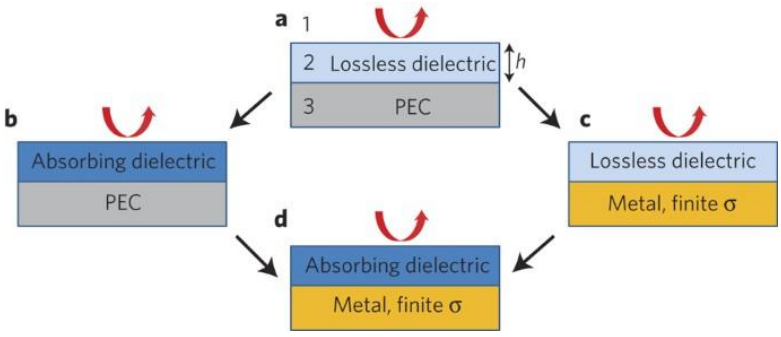

Figure 1. *Illustrating scheme of a the four possible combinations in a Gires-Tournois interferometers; with a lossless (**a**, **c**) or absorbing dielectric(**b**, **d**) and with perfect electric conductor (ideal metal, **a**, **b**) or real metal with finite conductivity (**c**, **d**).*[33]

However the introduction of losses both in the metal and the dielectric (**Figure 1a-d**) also plays a major role in the response of the system. In the case of a perfect electric conductor (PEC) with a lossless dielectric atop represented in **Figure 1a**, as there is neither absorption nor penetration into the metal, unity reflectance at all wavelengths is obtained. This type of systems can be used as elements for phase-shifting, commonly called Gires–Tournois etalons. When an absorbing dielectric is deposited on a PEC substrate, as depicted in **Figure 1b**, the system shows an absorption FPR for thicknesses equal to $m\frac{\lambda}{4n}$ (m is an odd integer and n the refractive index of the dielectric layer). No FP resonance exists for *h* smaller than $\frac{\lambda}{4n}$. A system composed of a lossless dielectric film on a real metal with finite optical conductivity such as gold or silver at visible wavelengths (**Figure 1c**) can support a resonance for $h \ll \frac{\lambda}{4n}$ owing to the non-trivial phase shifts at the interface between the dielectric and the metal, but the total absorption is small because the only loss mechanism is the one associated with the finite reflectivity of the metal. Finally, our case of interest, an ultrathin ($h \ll \frac{\lambda}{4n}$) absorbing semiconductor on a Au film at visible frequencies can support a strong and widely tailorable absorption resonance (**Figure 1d**). In this latter case, as explained in **chapter 1.3.5**, because of the penetration depth of the electric field in the metal at visible wavelengths, there is a phase shift superior to π in the partial reflection of the metal boundary (**Figure 2c, d** blue dashed line). As the destructive interference resonance condition for a Gires-Tournois resonator, leading to maximum absorption, requires that the total phase accumulation upon one round-trip in the cavity should equal an integer multiple of 2π (360 degrees in **Figure 2c, d**), this non-ideal behaviour of the metal enables reaching such resonant condition requiring less accumulated propagation phase, i.e. less active material thickness (**Figure 2c, d** red dashed line). Therefore, the resonant condition is below the classical $\frac{\lambda}{4n}$ condition. For instance, as is it presented in **Figure 2b**, a 12nm layer of amorphous germanium on top of the silver mirror presents a strong interference resonance at 625nm: the resonant condition is met at $\frac{\lambda}{11n}$. Also, due to the large refractive index of the germanium (**Figure 3a**), compared with the impinging media of air, the refraction angle remains very small within a wide range of incidence angles. This causes that each phase term shown in **Figure 2c, d** remains almost constant until the angle of incidence reaches 60 degrees. Another side effect of this high refractive index contrast is that the Brewster angle is pushed up to almost 80° (**Figure 2c**). These properties render this system with almost omnidirectional resonant absorption conditions.

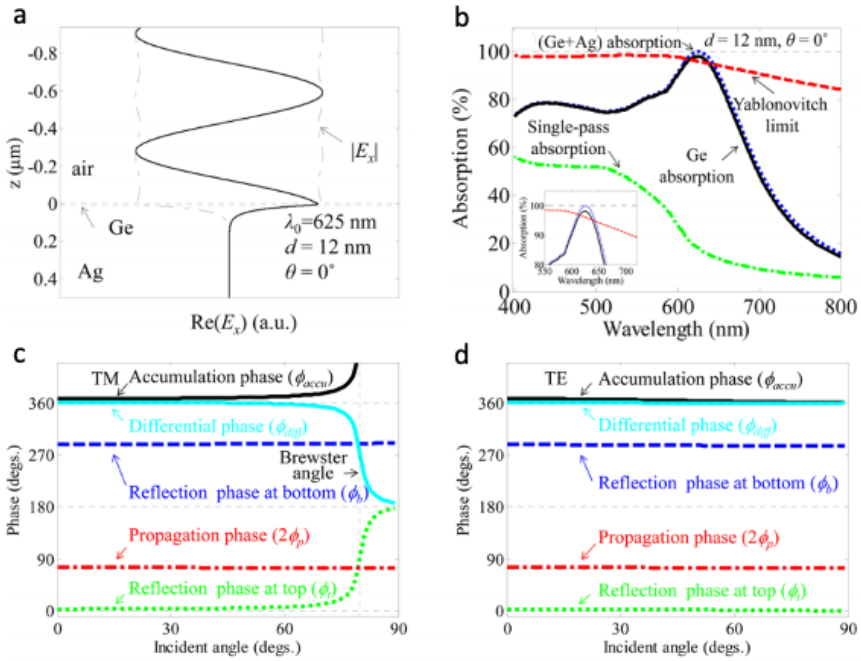

Figure 2. *(**a**) Transverse electric field (x-component) distribution for the air/ Ge (12 nm)/Ag case with λ_0 = 625 nm. Solid line: Re(Ex); dash-dotted line: |Ex|.(**b**) Absorption spectrum for the normal incidence. Dashed red line: Yablonovitch limit; dotted blue line: absorption in Ge (semiconductor) and Ag (metal); solid black line: absorption in Ge; and dash-dotted green line: single-pass absorption. (**c**) Reflection and propagation phases. Dash-dotted red line: propagation phase retardation in the semiconductor; dotted green line: reflection phase pickup at the top interface (air/Ge); solid black line: total phase; and dashed blue line: reflection phase pickup at the bottom (Ge/Ag). (**d**) TE result. The line legends are the same as in (**c**).*[72]

To provide explanation for the large and broadband absorption peaks found in this ultrathin system, we have to investigate the system proposed by Prof. Capasso in further detail. To do it we have to consider an a-Ge planar waveguide of thickness *t* with permittivity ε_d surrounded by two semi-infinite media (air and gold) with dielectric permittivities ε_a and ε_m, respectively (**Figure 3b**), and recover the equation relation for the existence of interface surface modes developed in **chapter 1.3.5**, which reads as:

$$k_{//} = k_0 \sqrt{\frac{\varepsilon_m \varepsilon_d}{\varepsilon_m + \varepsilon_d}} \qquad (1)$$

As explained in **chapter 1**, in the case of lossless materials, it is easy to see that, if $-Re(\varepsilon_d) < Re(\varepsilon_m) < 0$, then the propagation constant $k_{\|}$ is purely imaginary. This means that the modes

correspond to non-propagating waves or localized modes.[69] The energy of the evanescent surface wave is dissipated into two radiative waves propagating away from the surface. When we introduce strong losses in the system, such as the one presented, $k_{\parallel}$ becomes complex with a high imaginary part and the waves in the two media also become evanescent, rendering high absorptions. This condition, already presented in the introduction **chapter 1**, re-called as the quasi-bound regime, occurs for amorphous germanium on a gold substrate up to a wavelength λ =764 nm ($-\varepsilon'_{Ge} < \varepsilon'_{Au} < 0$). For instance, in the case exposed in **Figure 2,** at 625nm, $\varepsilon_{Ge} = 19.4 + 13.1i$ and $\varepsilon_{Au} = -11.2 + 1.3i$. The introduction of strong losses for gold and germanium favours high values for the imaginary part of $k_{\parallel}$ in a broader bandwidth. Due to the high extinction of the semiconductor layer in the quasi-bound regime, the FPR lead to very broad and intense absorption peaks related to highly damped surface modes. The 12 nm a-Ge film on top of a silver substrate presented in **Figure 2** exceeds 98% absorption (**Figure 2b**) at 625nm with a full-width half-maximum (FWHM) of almost 150 nm. This architecture is capable of exceeding the Yablonovitch classical limit[106] for light trapping in thin films (**Figure 2b**, red dashed line).

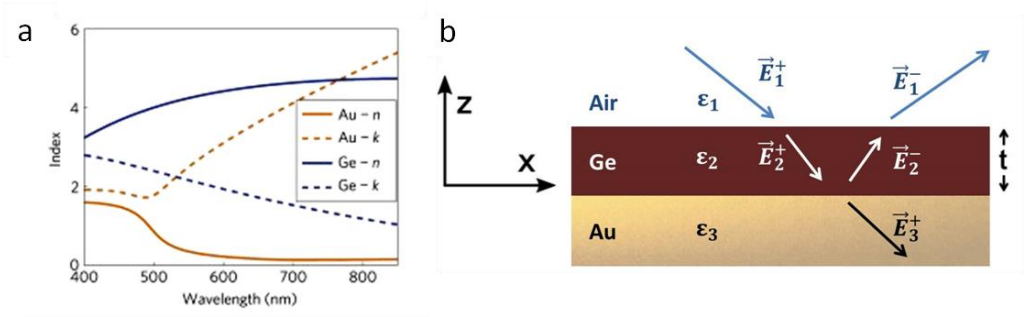

Figure 3. *(**a**) Real and imaginary refractive indices of gold and amorphous germanium.*[33] *(**b**) Scheme of the studied multilayer system used to obtain the dispersion relations of the layered structure.*

To gather a better insight of the absorption of such yet simple but powerful system we evaluated the evolution of the absorption profile of a 15 nm thick flat a-Ge film on gold as we change the angle of incidence and evaluated it with the dispersion relation of the system (**Figure 4**). In agreement with previous reports,[33,72] we find that such a simple layered configuration can also exhibit coupling between the incident light and a quasi-bound Brewster-type resonance whereby the energy of an incident plane wave is almost totally absorbed by the active medium. As explained in **chapter 1.3.5**, these Brewster modes are radiative modes which become surface

modes in the presence of losses.[69] The characteristic width of these absorption peaks originates in the above-mentioned quasi-bound regime of high damped modes where the reflected field is entirely suppressed. The large confinement factor together with a slow group velocity due to the flat dispersion curve of the quasi-bound Brewster modes (**Figure 4**) make the system a candidate for high absorption.[121] Our simulations, presented in **Figure 4a** and **b,** indicate that total absorption of the incident energy may occur in both TE and TM polarization. It is shown that for a thin layer of 15 nm the dispersion relation for the TM polarization reaches values of $k_{\parallel} \approx 0$ i.e., can be excited from normal incidence.

The surface wave is not permitted for the TE polarization at an interface dielectric/metal for this polarization.[122] However, the existence of an artificial surface wave in nonmagnetic media has been reported when an ultrathin film of high dielectric permittivity is inserted on a metal substrate.[123]

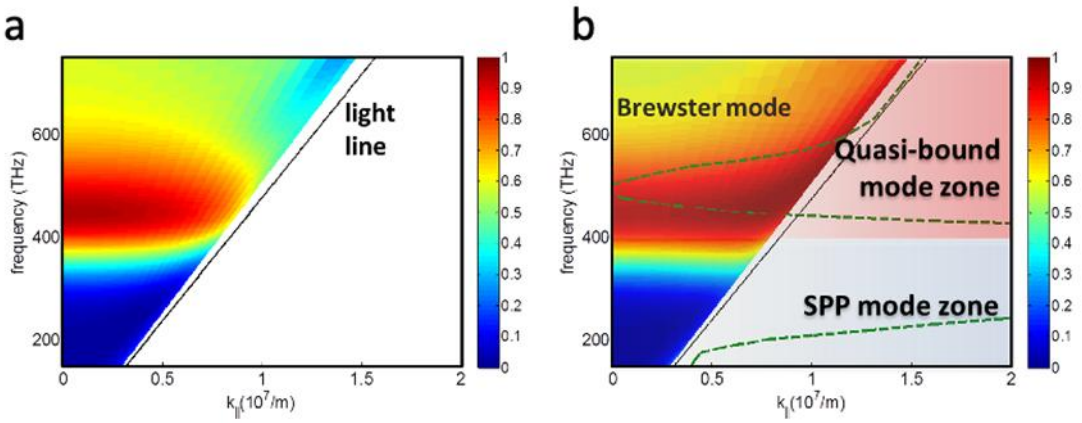

Figure 4. *Total absorption versus dispersion relation (frequency versus the parallel wavevector) in a 15 nm thick Ge layer for TE (**a**) and TM polarizations (**b**), showing the dispersion (green dashed curve) of the system calculated by FDTD is shown.*

As just demonstrated, such a simple architecture is capable of exceeding the Yablonovitch classical limit[106] for light trapping in thin films[72] and has tremendous potential to boost performance in photovoltaics[124], photocatalysis[125] and photodetection. However, the exploitation of these surface modes to improve light absorption is restricted to the visible regime, where the a-Ge film is strongly absorbing and the metal behaviour of gold and silver is far from a perfect electric conductor (PEC).

When the thickness of the active layer is increased, the absorption band due to the strong interference shifts to longer wavelengths (**Figure 5**). At these wavelengths, gold behaves closer to an ideal metal and $Re(\varepsilon_m) < -Re(\varepsilon_d) < 0$, meaning that we are no longer in the quasi-

bound regime. As is presented in **Figure 5**, this characteristic, together with the low values of the absorption coefficient of Ge for these wavelengths, results in a much lower absorption for the NIR range FPR.

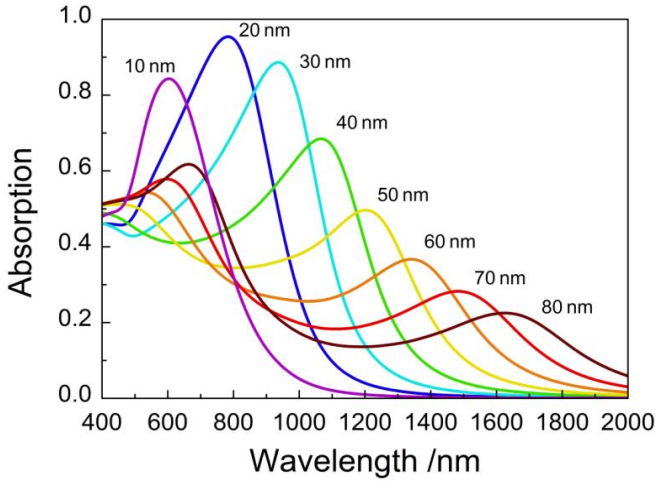

Figure 5. *Simulated absorption spectra of a-Ge thin films over gold substrates with different thickness increased from 10 nm up to 80 nm.*

This situation can be understood by comparing the absorption and dispersion relation of a 15nm thin film shown in **Figure 4** with that of a 70nm presented in **Figure 6**. In the latter case, the dispersion relation in the quasi-bound mode zone reaches only $k_{||}$ close to the light line due to the increasing thickness of the germanium,[126] as it is corroborated by the absorption profile in this zone (TM polarization).

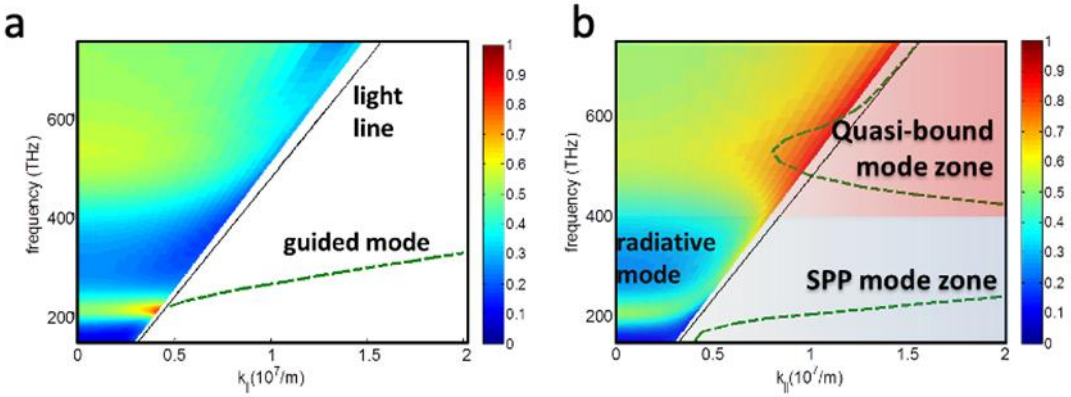

Figure 6*. Total absorption versus frequency versus the parallel wavevector (dispersion relations) in a 70 nm thick Ge layer for TE(**a**) and TM(**b**), showing the dispersion (green dashed curve) of the system calculated by FDTD.*

Therefore, light at normal incidence cannot be coupled to surface Brewster modes, which in turn, do not have the flat dispersion curves present in the case of the thinner films, substantially decreasing the absorption. This leads to a poor absorption for normal incidence FPR. It is also noticeable that, due to the thickness increase, a guided mode beyond the light line appears for the TE polarization.

Therefore, this strategy fails to provide strong absorption peaks when the thickness of the semiconductor layer is increased. Hence, a light trapping scheme that allows for a broadband absorption enhancement throughout the whole absorption region of germanium is still lacking.

In this chapter we describe how to design and fabricate an architecture based on ultrathin germanium films with broadband absorption, taking advantage of the aforementioned quasi-bound regime and the coupling to Brewster modes in the visible region (**Figure 7a**) but enhancing the absorption in the near infrared with a consciously designed 2D photonic crystal (PhC) structure (**Figure 7b**). We study how the photonic structure affects the incoming light, how it enables it couple to highly absorbing modes, and how its geometrical parameters can help us to tune its response.

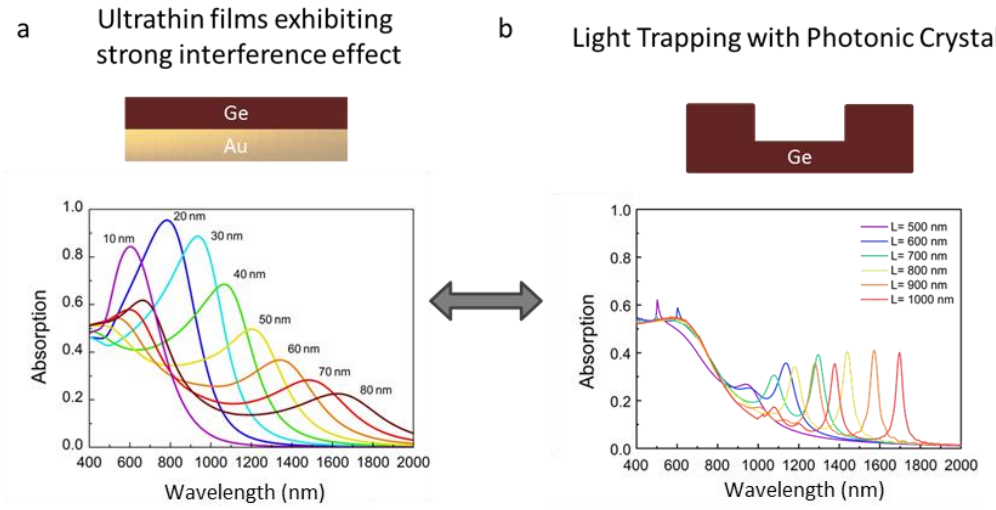

***Figure 7**. The two light trapping schemes that we will try to combine in this chapter: (**a**) the strong interference in ultrathin films, with thickness dependent absorption; and (**b**) the photonic modes provided by a photonic crystal tuneable with the lattice parameter that will be used to enhance the absorptions in the NIR.*

3.3. Ultrathin semiconductor superabsorbers from the visible to the near infrared

Our structure consisted in the a-Ge 2D square array of cylindrical holes built on top of a gold film shown in **Figure 8**. In a cross section of our a-Ge photonic crystal, two a-Ge heights are differentiated, t_1 and t_2 (**Figure 8d**); the overall layer of t_2 = 70 nm and the bottom part of t_1 = 15 nm inside the holes (55 nm depth).

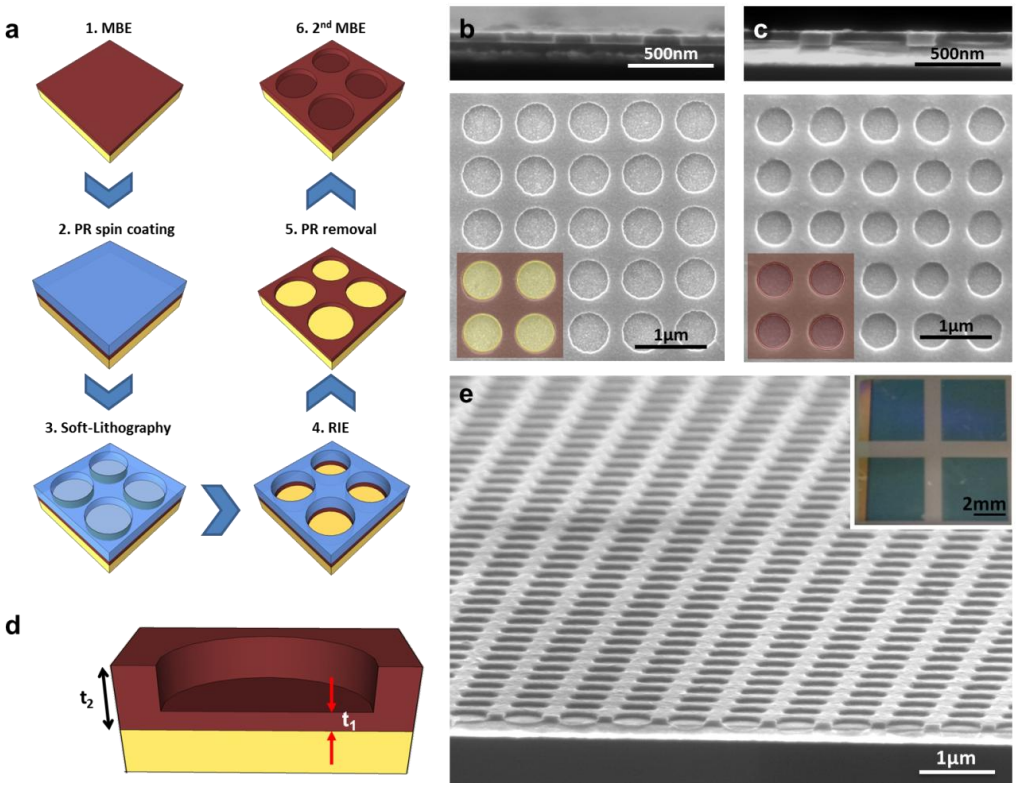

Figure 8. *Fabrication process of the nanostructure by NIL: (**a**) deposition of the a-Ge layer on gold by MBE (1), spin coating of the photoresist (2), nanoimprinting (3), reactive ion etching to expose the gold film underneath (4), removal of the resist (5) and a second deposition of a-Ge (6). (**b**) Top view and cross sectional (inset) SEM images of a nanostructured 55 nm thick a-Ge layer with a square array of cylindrical holes on gold (step 5 in fabrication scheme). (**c**) Top view and cross sectional (inset) SEM images of a 70 nm thick a-Ge square array of cylindrical holes filled with 15 nm thick a-Ge (step 6 in fabrication scheme). (**d**) Schematic depiction of the cross section of the a-Ge photonic crystal on gold. Two distinct heights of a-Ge can be distinguished corresponding to t_1 = 15 nm and t_2 =70 nm in the actual sample. (**e**) Tilted SEM view of the final a-Ge photonic crystal. Inset: Photograph of four germanium photonic crystal structures on gold with 4x4 mm^2 patterned areas.*

These two heights of a-Ge together with the metallic substrate allowed the architecture to sustain simultaneously, (i) a surface Brewster mode in the VIS range associated to the lower thickness t_1 and (ii) a suppression of backscattering in the NIR due to the coupling between the FPR of the thickness t_2 and the photonic-plasmonic modes of the nanostructure.

The 2D PhC structure designed using FDTD simulations maximized the absorption of the system from 400 nm to 1500 nm (**Figure 9**). The square array was chosen over other geometries because of the more extensive set of reciprocal lattice vectors sustained by the photonic crystal, hence the higher number of resonant modes contributing to the absorption spectrum. Regarding the morphology of the photonic crystal slab, an air hole array was preferred over a germanium pillar nanostructure due to its easier fabrication procedure and larger fill factor for the higher a-Ge thickness leading to slightly higher absorption in the near infrared (**Figure 9**).

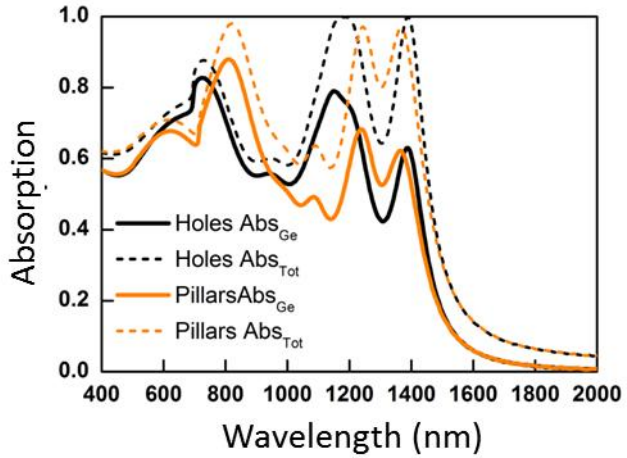

***Figure 9**. Total (dashed lines) and semiconductor (solid lines) absorptions of a hole array photonic structure (black) and a pillar array structure (orange) with r = 300 nm, t_1 = 15 nm, t_2 =70 nm and L = 700 nm.*

The thickness of the a-Ge layer on gold determined the frequency range at which the FPR appear (**Figure 7a**). The photonic crystal profile with two differentiated heights (**Figure 8d**) allowed to excite these resonances both at visible and NIR range. The filling fraction between both heights of a-Ge present in the photonic architecture determined the interplay between the absorption at VIS versus NIR wavelengths. To achieve precise control over all the thicknesses involved in the structure, the a-Ge layer deposition took place in two steps as summarized in the fabrication procedure (**Figure 8**). In brief, a 55 nm a-Ge layer was deposited onto a gold-coated substrate by molecular beam epitaxy (**Figure 8a1**). Then, a 250nm thin film of Shipley photoresist was deposited by spin coating and nanopatterned with sNIL methodology using a prepatterned sPDMS stamp, as explained in **chapter 2.2.2.2** (**Figure 8a2 and *3***). After the soft

NIL, a two step dry etching process was performed. First, a O_2 RIE was carried out to etch the remaining resist at the bottom of the imprinted holes and expose the germanium film. Secondly, we used a mixture of $SF_6/CHF_3/O_2$ gases in a second RIE process to transfer the pattern to the germanium and expose the gold substrate through the holes (**Figure 8a*4***). Finally, the resist is removed with acetone (**Figure 8a*5***). At this stage of the process (**Figure 8b**), the structure, a 55 nm a-Ge PhC, exhibited a strongly enhanced absorption in the NIR range (**Figure 10b**). In order to amplify the absorption in the visible range, a second 15 nm Ge layer was deposited (**Figure 8a6**). The resulting photonic structure consisted on a thin a-Ge layer t_1 deposited at the bottom of the hole array surrounded by a thicker a-Ge layer t_2 (**Figure 8c, d and e**). The final textured surface strongly absorbed visible wavelengths while exhibiting intense absorption peaks reaching almost 100% at the NIR range (**Figure 10a**). The absorption spectra of two flat a-Ge films on gold shown in **Figure 10c and d** illustrate the FPR modes excited at each thickness. On one hand, a 15 nm thick a-Ge layer (**Figure 10d**) achieved a single almost total absorption peak at 760 nm. On the other hand, the absorption of the 70 nm flat a-Ge film on gold (**Figure 10c**) shifted towards the NIR, but falling below 50% at 1400 nm. In comparison, the absorption measured in the final a-Ge photonic architecture was much more than the sum of the two FPR modes sustained by the different a-Ge thicknesses; there was an additional contribution to the absorption provided by the photonic crystal geometry, greatly improving the NIR response of the film. This resulted in an integrated absorption in the a-Ge of 61% from 400 nm to 1500 nm (**Figure 11b**), an enhancement of 78 % compared to the flat configuration with 70 nm germanium film on gold.

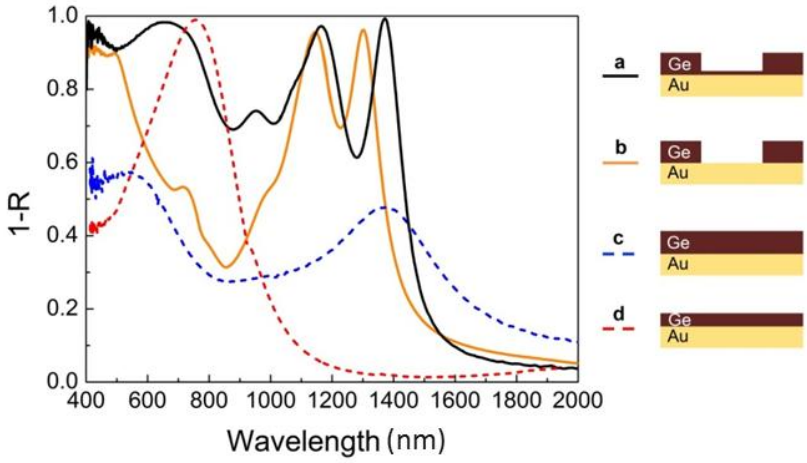

Figure 10. *Extinction spectra (1-R) of different a-Ge nanostructures fabricated on a gold film. (**a**) 70 nm a-Ge 2D PhC on a square array of cylindrical 55 nm deep holes; (**b**) 55 nm a-Ge 2D PhC with a square array of cylindrical holes etched down to the gold film; (**c**) a flat 70 nm thick a-Ge layer; (**d**) a flat 15 nm thick a-Ge layer.*

3.3.1. Analysis of the enhanced absorption provided by the structure

We investigated the role of the photonic crystal geometry in the enhancement in absorption, especially at the NIR frequencies where there were no Brewster modes to couple to. To elucidate the different resonant modes sustained by our photonic structure, the total absorption was calculated for architectures with a fixed radius r = 300 nm and thicknesses t_1 = 15 nm and t_2 = 70 nm, upon varying the lattice parameter L (**Figure 11a)**. The dashed line corresponds to a lattice parameter of L = 700 nm, being the photonic architecture under study in **Figure 11b**. In the latter we show that the simulated total absorption accurately reproduced the position of the experimental absorption peaks. From the fitting it was also possible to extract the fraction of light absorbed by the a-Ge layer, being the rest of the absorbed light lost in the gold substrate (**Figure 11b**).

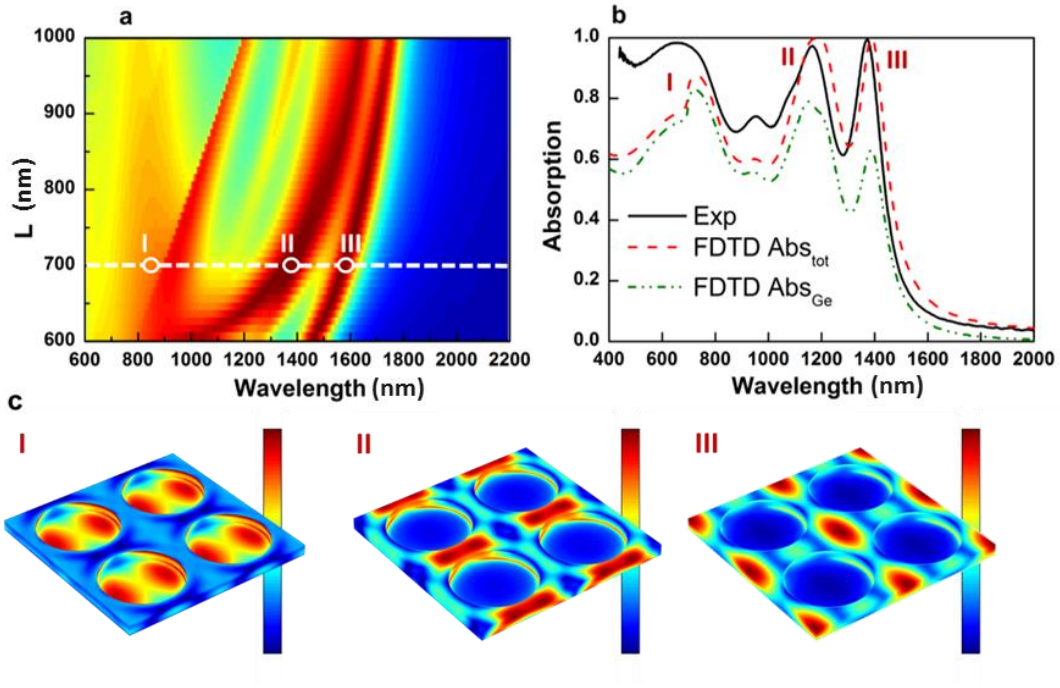

Figure 11. *Optical resonances sustained by the photonic structure. (**a**) Calculated total absorption at normal incidence with r = 300 nm, t_1 = 15 nm, t_2 =70 nm as a function of wavelength and lattice parameter L.. (**b**) Experimental 1-R (solid black line) and simulated total absorption (red dashed line) of the a-Ge PhC on gold with pitch L = 700 nm, corresponding to the horizontal dashed line in **a**. The fraction of light absorbed by the germanium is also plotted (green dash-dotted line). (**c**) Spatial distribution of the normalized electric field at the three wavelengths circled in (**a**): 600 nm (peak **I**) 1170 nm (peak **II**) and 1370 nm (peak **III**).*

Next we analyzed the different resonances that originated the absorption peaks by looking at the spatial distribution of the electric field in the structure (**Figure 11c**) at the three wavelengths encircled in **Figure 11a**. In the visible spectrum, at a wavelength $\lambda \approx 600\, nm$, the resonance (peak **I**) was due to the coupling of the incident light to the FPR-Brewster mode produced by the strong interference in the t_1 slab (**Figure 11c**). This peak was very broad (from 500 to 900 nm) due to the high extinction of the semiconductor layer in the quasi-bound regime, as explained previously in this chapter (**section 3.2**).[127] The position of the FPR-Brewster resonance was not affected by the increase in lattice parameter L (**Figure 11a**, VIS regime), as its spectral position mainly depends on the thickness of the active layer t_1. Only a decrease in the magnitude of the absorption occurred when the filling fraction of t_1 decreased with respect to that of t_2. This mode (**I**) intersected with the first order of diffraction for $\lambda \approx L$ (in our example L = 700 nm) that corresponds to the straight diagonal mode in **Figure 11a**. In sum, for short wavelengths the electromagnetic radiation was mostly enclosed within the thin t_1 a-Ge layer (**Figure 11c, I**) and diffracted modes of the architecture also appear.

The maps of the electric field distribution at longer wavelengths, $\lambda \approx 1170 \wedge 1370\, nm$ shown in **Figure 11c, II and III** indicate the confinement of the electric field in the overall layer t_2 of a-Ge. Here, the field distribution follows the geometrical modes of the inverse a-Ge photonic crystal. In this regime, the total absorption approached 100% with 80% of the absorption attributed to the a-Ge. Moreover, this absorption spectrum was robust against changes in the angle of incidence as proven by FDTD simulations for the two polarizations, even for large angles up to the first diffraction order line (See black dotted line in **Figure 12c and d**). Above the diffraction line, at higher angles, there are radiation losses because part of the light was diffracted back to air.

Regarding the nature of these resonances, it is useful to remember that, as introduced in **chapter 1.3.3**, a bidimensional grating accesses parallel wavevectors $k_{\parallel}$ larger than $k_0 = \frac{\omega}{c}$ inside the photonic crystal. The parallel wavevector $k_{\parallel}$ can be obtained from **equation 2** (blue lines in **Figure 12c**):

$$k_{\parallel} = k_{\parallel 0} \pm G_m \qquad (2)$$

Where $G_m = m_{xy}\frac{2\pi}{L}$, $m_{xy} = \sqrt{m_x^2 + m_y^2}$, and $m_x, m_y = 0,1,2 \ldots$ A combination of numbers $[m_x, m_y]$ gives the diffraction order inside the semiconductor layer. Therefore, the bi-dimensional periodicity granted access to the photonic-plasmonic modes with $k_{\parallel}$ larger than the

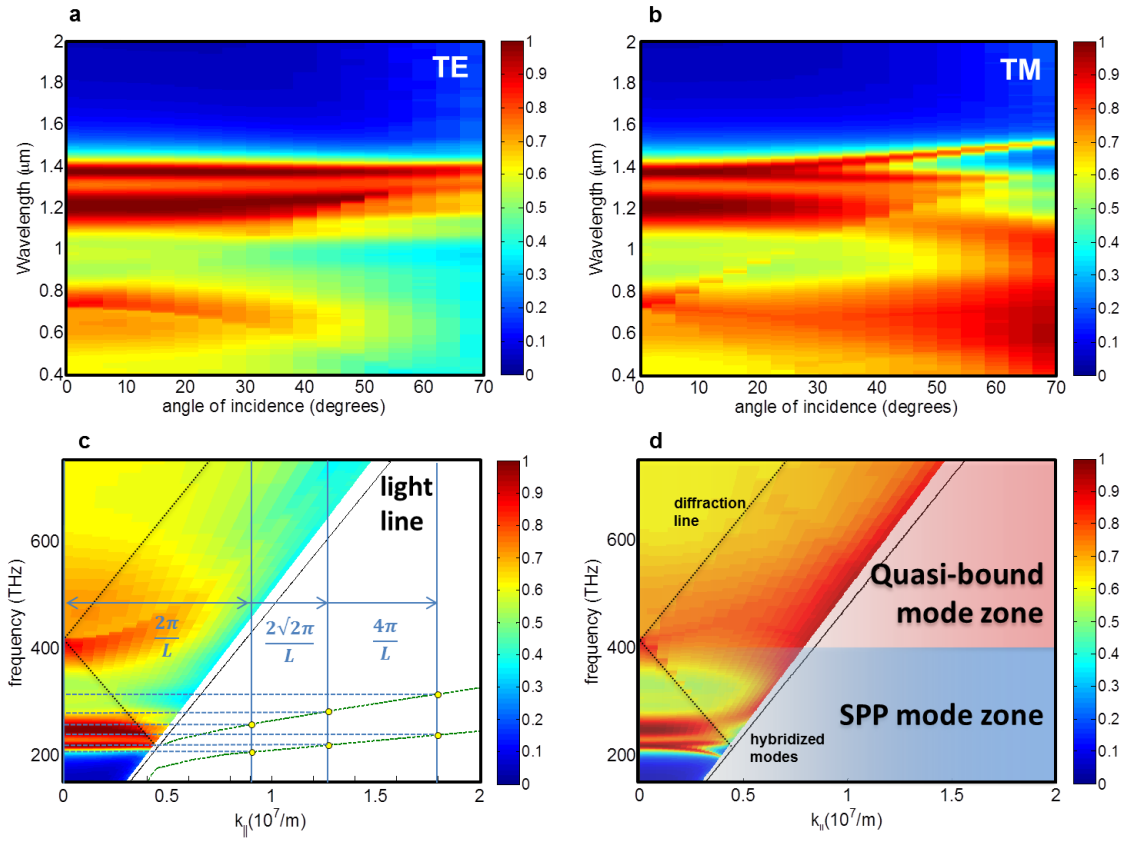

Figure 12. *Total absorption versus wavelength and angle of incidence in a photonic structure with r = 300 nm, t_1 = 15 nm, t_2 =70 nm and L = 700 nm for TE (**a**) and TM polarizations (**b**). Dispersion relation of frequency versus parallel wavevector for both polarizations, (**c**) and (**d**), respectively. Scheme of the decomposition of radiation phenomena into a superposition of discrete modes, (**c**). The vertical blue lines correspond to the $k_{||}$ of the diffraction orders of the lattice which couple to the modes above the light line (green dotted lines).*

air-light line, which could not be excited from outside an unpatterned thin film because of insufficient $\boldsymbol{k}_{||}$ (green dotted dispersion lines in **Figure 12c**). The absorption exhibited by our nanostructure in the NIR was the result of the coupling between of these photonic-plasmonic modes and the FPR (**Figure 12**). We designed the architecture to spectrally match the position of the FPR, determined by the resonant condition associated to thickness t_2 -as is shown by the confinement of the electric field in this layer (**Figure 13c**)- with the photonic-plasmonic modes, governed by the matching between the diffraction modes of the bidimensional grating and the allowed surface photonic-plasmonic modes (**Figure 12c**, blue dotted lines). The flat dispersion relation of the photonic-plasmonic modes, represented by the green dotted lines in **Figure 12c**, indicate an associated group velocity much smaller than *c* (i.e., a large density of states), which

amplify any light-matter interaction phenomena such as light absorption.[121] The cross-sectional maps of the electric field distribution of the hybridized modes, presented in **Figure 13**, confirm their bound nature to the interface. These photonic-plasmonic resonances are two surface waves at the interfaces Ge/Au and air/Ge which show evanescent fields in both air and Au layers.

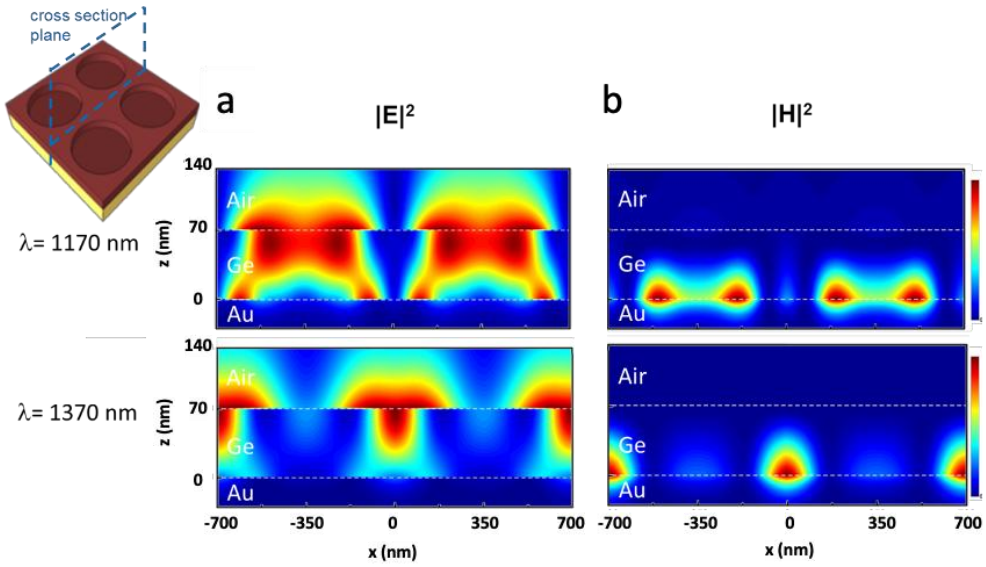

Figure 13. *Intensity of the (**a**)electric and (**b**)magnetic field at the plane shown in the top inset at wavelengths, 1170 and 1370 nm for the nanostructure (the units are normalized to the maximum of each plot).*

Moreover, these hybrid modes showed a confinement of both magnetic and electric fields similar to findings in previous works[71,128,129] in which the interference of magnetic and electric dipoles plays a major role in the angle-suppressed scattering. An important role both for the interference resonance and the large confinement was played by the incorporation of the metal substrate. We enlightened this phenomenon by representing the field behaviour of the a-Ge photonic structure without metal substrate and comparing it with the complete system metal/semiconductor. **Figure 14** shows how the confinement was significantly larger in the maximum absorption peaks of the structure with metal substrate, **d** and **f**, relative to those of the structure without the metal substrate, **c** and **e**. Consequently, the absorbed fraction of light is much larger (**Figure 14a**).

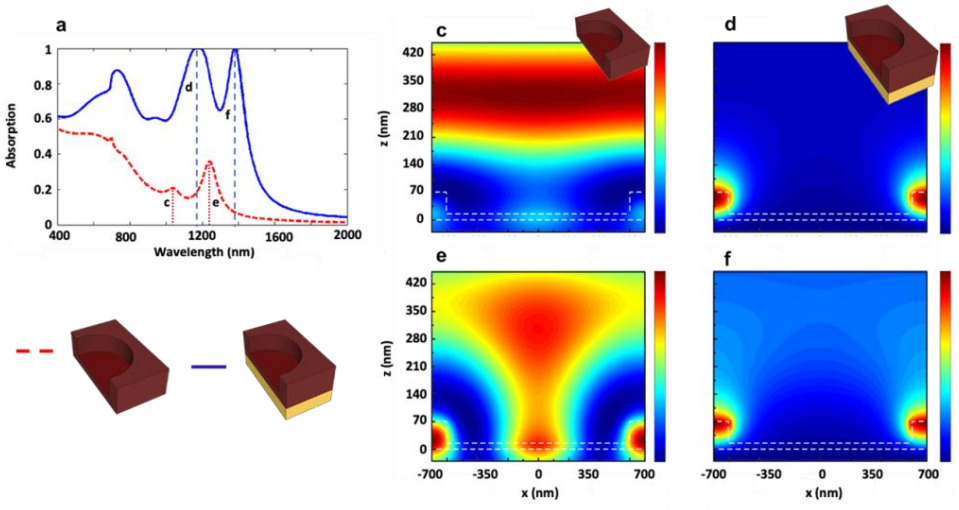

Figure 14. *Effect of the metallic substrate in the confinement of the electric field. (**a**) Absorption at normal incidence of the system calculated by FDTD for the a-Ge hole square array over metal (blue solid line) and without metal (red dashed line). (**b**) Scheme of the cross section of the structures perpendicular to the plane of incidence for TM polarization. Intensity of the electric field at the resonant wavelengths for the nanostructure (**c**), (**e**) and with the gold substrate (**d**) and (**f**). The resonant wavelengths are at 1035 nm (**c**), 1,240 nm (**e**), 1,170 nm (**d**) and 1370 nm (**f**).*

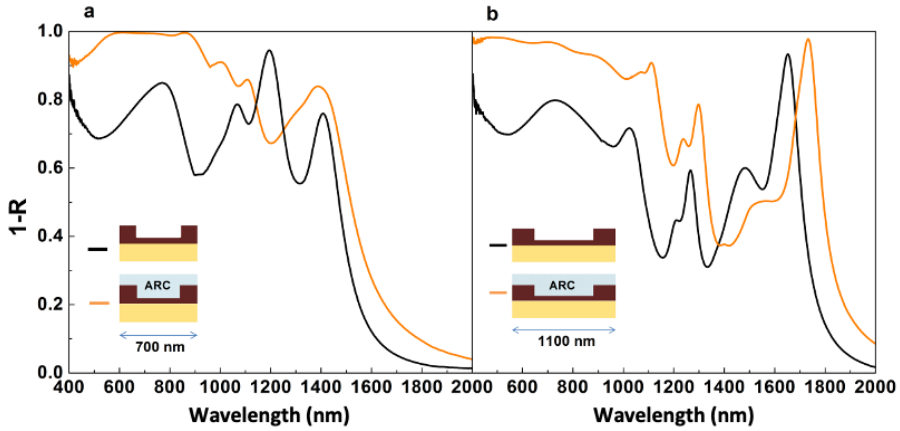

Figure 15. *Improvement of the visible light absorption using an Anti-Reflection Coating (ARC). Experimental 1-R of the photonic structure with (orange line) and without (black line) antireflection coatings for two different lattice parameters and hole radii: (**a**) L=700 nm and r = 300 nm. (**b**) L = 1100 nm and r = 880 nm. In both cases the a-Ge heights of the architecture were kept constant at t_2 = 80 nm and t_1 = 20 nm.*

In order to further increase the absorption in the visible region, we deposited, by spin coating, a 100 nm thin film of a lossless dielectric layer (Hydroxypropyl cellulose , n_{ARC} = 1.47) on top of the photonic crystal as an antireflection coating (ARC). This ARC layer decreased the impedance mismatch of the semiconductor with air, boosting the absorption in the visible spectrum, and producing an almost perfect total absorption in these frequencies (**Figure 15**). In this way, the a-Ge photonic crystal on gold with an ARC exhibited an 81% of total integrated absorption from 400 to 1500 nm (**Figure 15a**). The fraction of light absorbed in the germanium rised to a total of 69 %, which represented a 101% enhancement of the a-Ge absorption compared to that of a flat film with the same thickness.

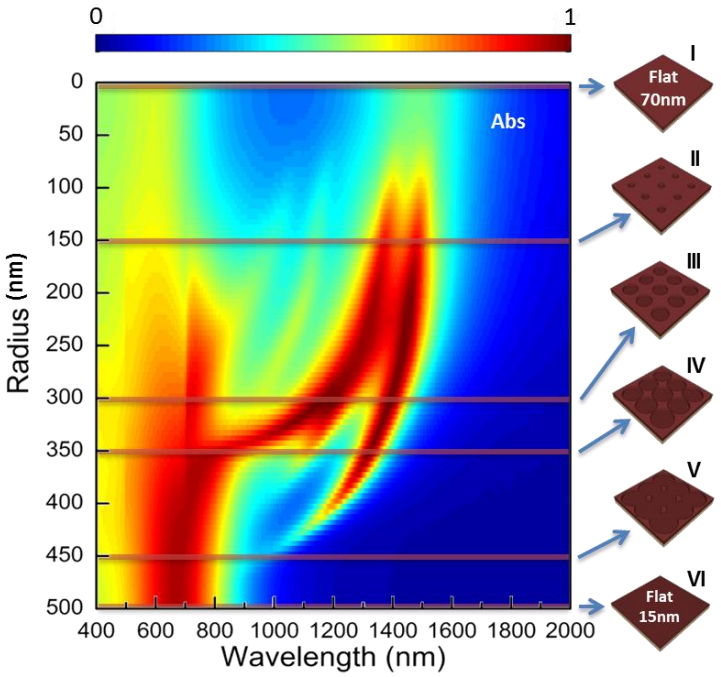

Figure 16. *Evolution with radii of the calculated total absorption versus wavelength at normal incidence of the photonic architecture with L = 700 nm, t_1 = 15 nm and t_2 =70 nm.*

3.3.2. Influence of the geometrical parameters

As we have seen in the previous section the resonances at long wavelengths showed a strong dependence with the geometric parameters of the photonic architecture. Here we elaborate on the versatility of our structure. In **Figure 16** we represent the absorption of an architecture where the hole radius r was varied in the array structure for a fixed lattice parameter $L = 700\ nm$. The structure evolved from a flat 70 nm thick Ge layer (**I**) ($r = 0$) to a flat 15 nm thick Ge layer (**VI**) ($r = \sqrt{2}/2\ L$), by opening holes. For radius reaching $r \approx 100\ nm$ (**II**) the photonic modes in the NIR, began to appear due to the structured layer and their spectral separation

increased with the radius (**III**). Furthermore, the increase of the radius involved a decrease of the fill factor of t_2 vs. t_1. This implies that there was more surface covered only with the thin layer of Ge. Thus, the absorption due to the strong interference in the thinner layer of t_1 = 15 nm emerged in the visible range. For $r = \frac{L}{2} = 350\ nm$ the holes started to overlap each other tangentially (**IV**) and the peak with the electric field confined at this position (absorption peak **II** of **Figure 11,** λ=1170 nm at r=300 nm) disappeared. The same happened with the mode related to the a-Ge between the four holes (λ=1370 nm at r=300 nm), in their cell diagonal. As the inverse cell structure decreased (**V**), this absorption decreased and shifted to shorter wavelengths (absorption peak **III** of **Figure 11**). Finally, when the diameter of the holes was equal to the diagonal of the cell (**VI**, $r = \sqrt{2}/2\ L$), all that was left was the flat thin layer of Ge t_1, with its FPR-Brewster peak at visible frequencies.

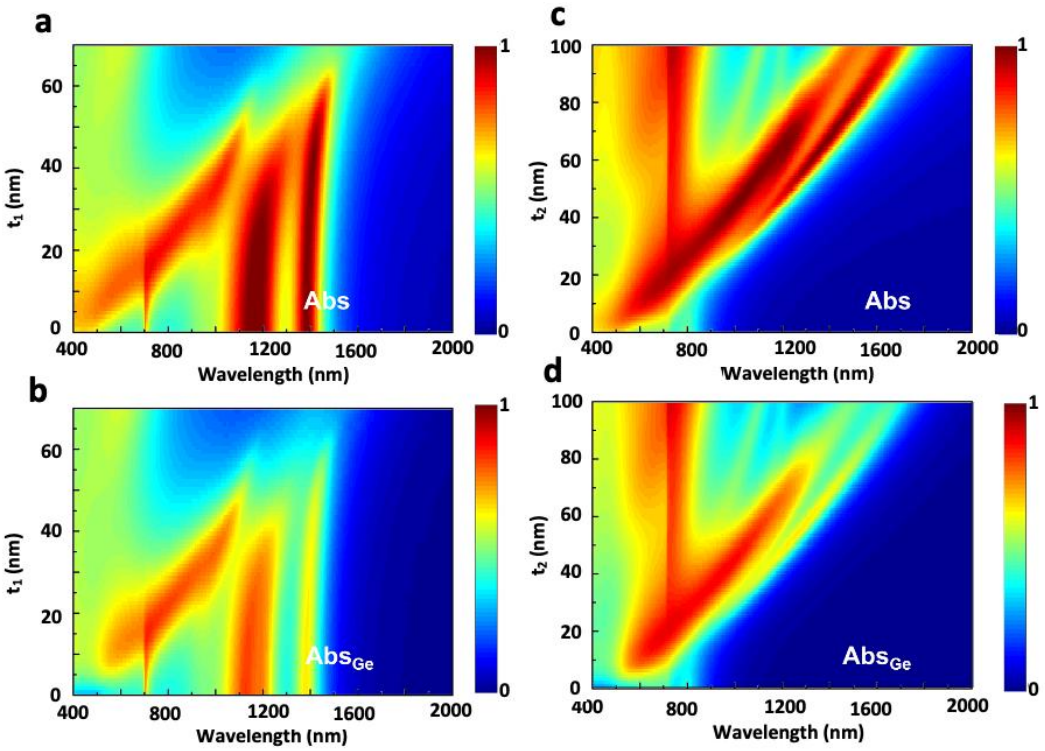

***Figure 17**. Evolution of the total absorption (**a**) and a-Ge absorption (**b**) in a square hole array with 700 nm lattice parameter and 300 nm radius. The larger thickness t_2 is kept fixed at 70 nm and the smaller thickness t_1 inside the holes is varied. Total absorption (**c**) and a-Ge absorption (**d**) in a square hole array with 700 nm lattice parameter and 300 nm radius. The larger thickness t_2 is varied and the smaller thickness t_1 is kept fixed at 15 nm.*

The thicknesses t_1 and t_2 were also essential characteristics in order to control the spectral positions of the absorption peaks as illustrated in **Figure 17** for both the total absorption and the fraction absorbed in the Ge active layer. The increase of t_1 when t_2 = 70 nm is fixed (**Figure 17a**

and b) causes an increase of the position in wavelength of the FPR-Brewster mode confined in the thinner slab t_1 whereas the other peaks associated to t_2 remained fixed. In **Figure 17c and d** , where thickness t_1 = 15 nm is fixed and thickness t_2 is varied, we can observe that for increasing t_2 the associated absorption peaks with the electric fields localized in t_2 shifted towards longer wavelengths whereas the peak associated to the thinner thickness t_1 remained fixed.

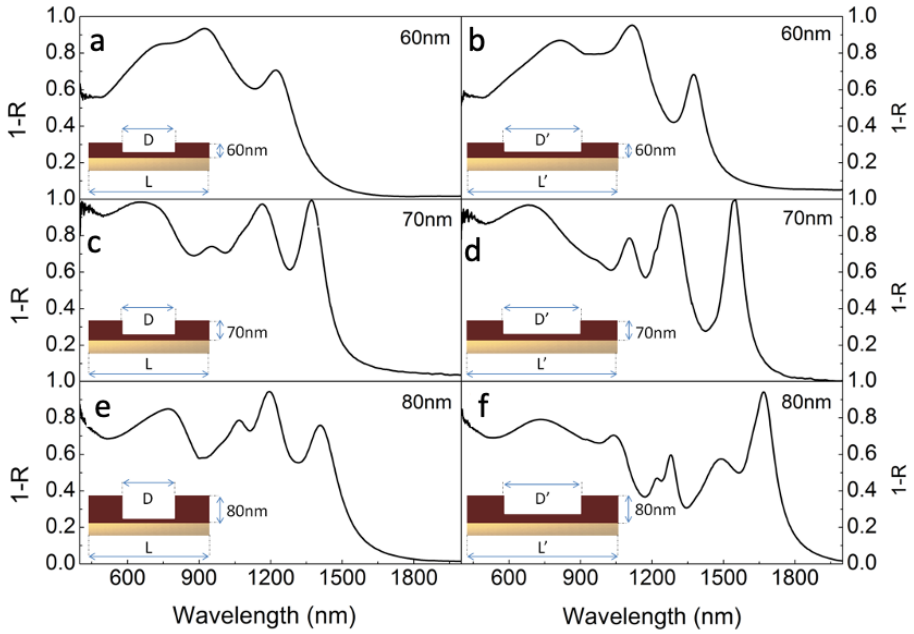

Figure 18. *Experimental extinction of the designed structure varying both layer thickness and lattice parameter showing tuneable absorption. Three thicknesses have been used: 60, 70 and 80 nm, one for each row of plots. Two parameter configurations are shown: the first column set samples had a lattice parameter (**a**, **c**, **e**) L =700 nm with a diameter D=560 nm and the second column samples had the parameters (**b**, **d**, **f**) L'=1100 nm and D'=880 nm.*

In **Figure 18**, we show the experimental extinction measurements for several samples that correspond to photonic crystal structures, varying the thickness and lattice parameters. In **a**, **c**, **e** the lattice parameter and the hole diameter are 700 nm and 560 nm respectively, and the large a-Ge thicknesses t_2 is varied with values of 60, 70 and 80 nm. The observed changes are in agreement with the calculations described above, where the NIR infrared resonances shift towards longer wavelengths as we increased the layer thickness. The same trend is found in the graphs **b**, **d** and **f**, for spectra measured on photonic crystals with 1100 nm lattice parameter and 880 nm hole diameter. In addition, for every fixed a-Ge thicknesses, larger photonic crystal lattice parameters showed to effectively shift resonant modes towards longer wavelengths, agreeing with results of **Figure 11a**.

3.4. Conclusions

A new design for ultra-thin super absorber device was proposed. Our structure consisted in a a-Ge 2D square array of cylindrical holes built on top of a gold film. The conscious pick of the materials involved and a proper design led to a 81% of total integrated absorption (69% in the semiconductor) over a broad spectral range, from 400 nm to 1500 nm. The herein demonstrated broadband absorption comes from the synergy of coupling the impinging light to Fabry-Perot resonances hybridized with Brewster modes in the visible spectrum and with photonic-plasmonic modes sustained by the architecture in the near infrared range.

By finely adjusting the a-Ge thickness, grown with MBE, we placed the spectral position of the Fabry-Perot resonance of the underlying layer in the quasi-bound regime, allowing a direct coupling to the surface Brewster modes. This rendered the substrate with a high and broad absorption. By setting the thickness to 15 nm, this almost reached total extinction and a 400 nm bandwidth from 500 to 900 nm.

The geometry of the photonic crystal dictated the frequencies for the photonic-plasmonic modes. With an array of 300 nm diameter holes in a 700 nm period etched in a 70nm thin a-Ge layer, these modes are placed in the NIR, between 1000 and 1500 nm. In this spectral range they match the position of the Fabry-Perot mode provided by the layer of the same thickness. Thus, we enhanced the low absorption profile of a thin film of the same thickness, which did not reach 50% due to the low values of the germanium absorption coefficient in these wavelengths. Thanks to the in-coupling of the light through the structure to these engineered slow light modes, this absorption was boosted up, achieving near unity absorption peaks, with almost 80% absorption in the dielectric.

By merging these two phenomena present in the visible and near infrared, the absorption in the active layer exceeded over 100% that of a flat 70 nm a-Ge film on gold. Furthermore, the high refractive index of the semiconductor renders the absorption profile of the photonic structure independent to the angle of incidence. The fabrication of these photonic structures followed a highly scalable nanoimprinting technique, which adds to the appeal of the enhanced optical properties described herein. We believe this photonic structure has a tremendous potential for light harvesting applications such as photodetection and photocatalysis. In addition, a properly designed interplay between FPR-Brewster and photonic-plasmonic modes may result in many exciting optical properties extendable to other systems and materials.

Chapter 4

4. Versatile all-dielectric metasurfaces fabricated by soft lithography and chemical vapor deposition

Among the high dielectric materials currently available, silicon has reached a prominence in the field of nanophotonics due to its low cost and straightforward implementation into current CMOS technologies.[18] In photonics, Si also has played a fundamental role, for instance, individual silicon nanoresonators support Mie resonances with both magnetic and electric dipolar nature.[128] The high field confinement achieved in these resonators has led to several advances in photo-electrochemical applications[130], all dielectric nanoantennas[131] and SERS.[132] Moreover, they also constitute the building blocks of more complex structures such as nanoparticle clusters[133,134], photonic crystals[135], metasurfaces and metamaterials[136] that exploit the different responses that originate from their interactions, determined by their morphology and arrangement.[18,71] This higher order arrangement provides unique characteristics emerging from the collective response such as magnetic perfect reflection, color filtering, electric and magnetic field enhancement, wavefront shaping and Huygens's metasurfaces.[10,45,136–141] Despite the great interest raised by high-index dielectric structures, their widespread implementation is hindered by their dependence on complex and expensive fabrication processes. Unlike plasmonic materials, straightforward synthetic methods for monodisperse high dielectric constant colloids are scarce. Silicon spherical particles have been achieved by magnesioreduction of silicon dioxide colloids[142] chemical vapor deposition (CVD)[143] and by laser ablation[144] but it still remains a challenge to assemble them into complex structures.

In this chapter we describe how to design and fabricate a silicon based photonic architecture that serves as a platform to excite electric and magnetic resonances in the VIS and NIR using highly scalable and inexpensive nanopatterning techniques. First, we unveil the unconventional fabrication procedure, overviewing also all the possibilities that the chosen fabrication techniques can offer. Next, we thoroughly discuss the resonances present in the metasurface, from those of the individual building blocks to the response of the whole architecture. Finally,

we use the designed metasurface as a substrate for light emission enhancement, trying to understand the phenomena that lead to this enhancement.

4.1. Unconventional nanofabrication of the metasurface

In order to exploit the Mie resonances exhibited by spherical silicon resonators in a large area metasurface, it is necessary to use highly uniform resonant units to obtain sharp resonances, useful for photonic applications. Classical lithographies have been used to produce many silicon metasurfaces with high homogeneity and resolution in which many of their exciting properties have been studied, but still present hurdles in scaling up the process. Most of the silicon colloids fabricated by other methods (CVD, laser ablation, silicon milling, etc) enabled the study of the Mie resonances on a single particle, but the optical properties are severely affected by the size distribution of the resonators and by their random organization. Herein we adapted the nanoimprinting lithography and CVD techniques for the creation of silicon metasurfaces based in silicon hemispheres. The integration of these techniques allowed the generation of a monodisperse array of silicon hemisphere resonators with the desired organization on the substrate surface, combining the resolution, monodispersity and spatial positioning of classical lithographies with a large scale focus for industrial applications.

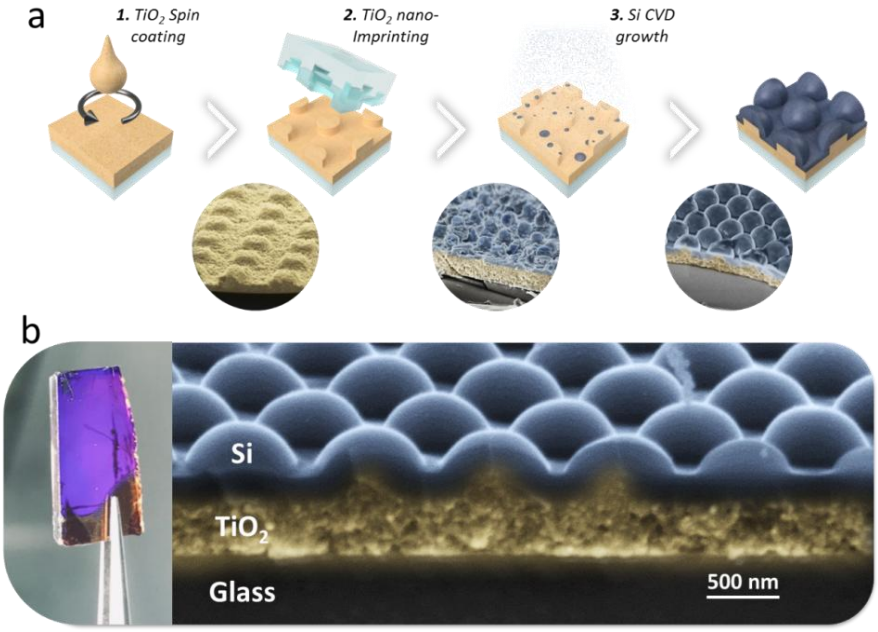

Figure 1. *(**a**) Schematics of the metasurface fabrication steps: (**1**) spin casting the titania paste, (**2**) nanoimprinting and annealing step and (**3**) Silicon coating by CVD. (**b**) SEM cross section and photograph of a fabricated sample.*

The fabrication procedure of our metasurface was reduced to two simple steps: the fabrication of a nanostructured mesoporous titania (m-TiO_2) backbone and the infiltration and coating with silicon (**Figure 1**). The first step relies on soft sNIL, a technique capable to produce extended nanostructured areas with high fidelity, rapidity, cleanroom-free and at a low cost, as explained in **chapter 2.2.2.2**.[2–4] In short, a pre-patterned hPDMS mold is pressed against the just spun coated layer resist that is left with a negative impression of the pattern (**Figure 1a**). As a NIL resist, we used a commercially available titanium dioxide nanoparticle paste dispersed 1:3 w/w in ethanol (90T Dyesol commercial paste). A porous network of sintered 20 nm anatase TiO_2 nanocrystals is left behind after the m-TiO_2 paste is annealed at 545°C, which withstands the 365°C required during the Si-CVD process without cracking or delamination. This porosity was later filled with silicon, endowing the structure with a higher refractive index, hence stronger light confinement. It is worth mentioning that a residual layer of resist was left under the pillars after demolding. In our case, we produced 350 nm pillars on a 400 nm thick resist layer (see **Figure 1b**). The residual layer, once infilled with silicon acted as a high refractive index waveguide whose thickness could be controlled at the spin coating step of the m-TiO_2 resist. Silicon deposition was achieved by low pressure, low temperature chemical vapor deposition using S_2H_6 gas as precursor.[145] Porous TiO_2 structures were placed in an ampoule under vacuum (10^{-6} Torr) where disilane at the desired pressure was condensed and then decomposed, to Si and H_2, at 365°C for 1 hour. The amount of infiltrated Si was controlled by adjusting the chamber pressure between 70 and 110 Torr. After Si infiltration, the Si/TiO_2 was cleaned gently with acetone to remove any byproduct that could have been deposited on the surface. Since in our set up, the decomposition of disilane was allowed to proceed to termination, it was the gas pressure what determined the amount of infiltrated Si for a fixed temperature.[143]

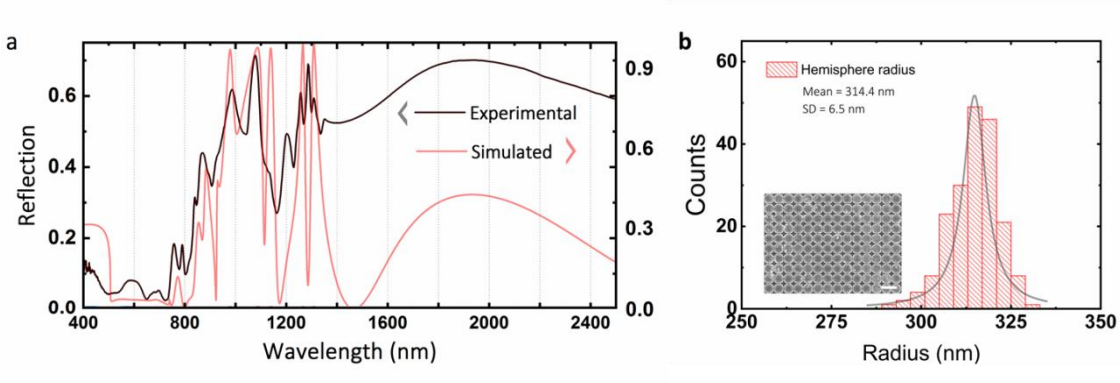

Figure 2. *Optical response of the metasurface with lattice parameter L= 600 nm on a 400 nm Si/TiO_2 waveguide. (**a**) Experimental vs simulated reflectance. (**b**) Radius distribution of the fabricated silicon hemispheres.*

The choice of temperature regulated the decomposition rate of disilane into silicon.[146] Initially, the Si infiltrates the m-TiO_2 backbone increasing the refractive index of the structure. Once the porosity of the m-TiO_2 is filled, the CVD conformal growth reaches a phase of accumulation of material on the top of the imprinted m-TiO_2 pillars, leading to the formation of the Si-hemispheres (**Figure 1b**). The good agreement between the simulated and measured optical response of the metasurface (**Figure 2a**) is thanks to a high homogeneity in the size of the grown hemispheres. We characterized the radius size and homogeneity of the fabricated hemispheres obtaining values of 314.4 ± 6.5 nm (**Figure 2b**), obtaining polydispersity values comparable with other techniques as can be seen in **Table 1**.

Method	Output	Area	Diameter	Standard Deviation	Spectral Range
Laser ablation[68]	Disordered Si NPs	cm^2	50 - 400 nm	--	700 - 800nm
Laser ablation[147]	Disordered Si NPs	mm^2	170.5nm	--	640nm
IL+RIE[148]	Ordered Si NPs	cm^2	1-2 µm	--	10 - 50 µm
Laser printing[149]	Disordered Si droplets	--	160-240	~2-3%	400 - 1000nm
Selective liquid laser heating[150]	Disordered c-Si spheres	--	161 nm	~200%	--
Laser ablation[151]	Disordered Si spheres	--	40-200 nm	~25%	400 - 1000nm
CVD + further separation[143]	Disordered Si spheres	--	1-4 µm	~30%	5 - 40 µm
Blender[152]	Disordered Si spheres	--	105 nm	~20%	300 - 800nm
NIL+CVD – This thesis	**Array Si spheres**	**cm^2**	**300-800 nm**	**~3%**	**400 - 2000 nm**

Table 1. *Summary of the particle size and polydispersity and scalability of the present work compared with previous works.*

We found good agreement between calculated and experimental reflections (**Figure 2a**), with minor disagreements between 1100 to 1400nm which can be attained to the differences in the collection measurements. In simulations, a plane wave was impinged and collected fully perpendicular to the sample. However, in the experimental setup, a 4X objective with numerical aperture of 0.1 was used for illumination and collection, rendering a light cone up to 6°. The optical response of the samples greatly depended on the angle of incidence, as we will show in the next section, and provoked the small mismatch. To give an idea of how the optical response

changed with the angles of illumination, we present in **Figure 3** the simulated optical response at 0° and 6° for both TM and TE incidences (**Figure 3a, b** and **c**, respectively). The average of the three spectra, shown in **Figure 3d**, may be a better approximation to represent the optical response obtained in experimental results. Nonetheless, this still does not recover the lack of coherence that is given by the source and the manufacturing imperfections.

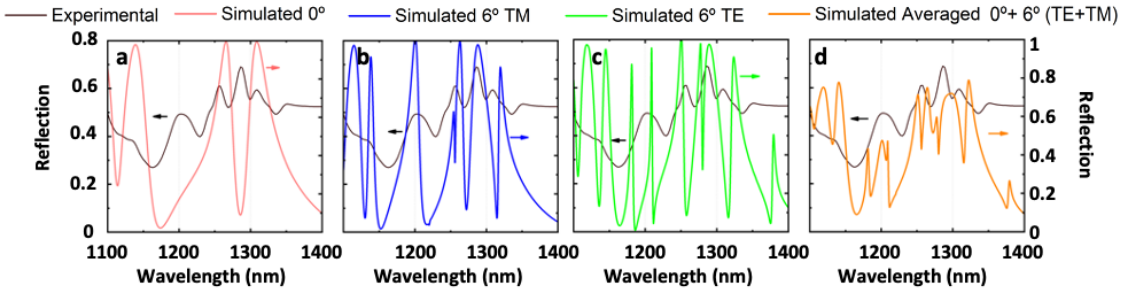

Figure 3. *Optical response of the metasurface with lattice parameter L= 600 nm on a 400 nm Si/TiO_2 waveguide. Experimental (black line) vs simulated reflectance at 0° (**a**) and 6° for TM (**b**), TE (**c**) and the average of the three (**d**).*

4.2. Origin of the optical response of the metasurface

We start by describing the role of each of the components of the metasurface and how they contribute to the overall optical response of the ensemble. In **Figure 4** we compare the FDTD simulated optical properties of the different components present in the final metasurface. We begin with the smaller and most simple resonant units, in this case a silicon hemisphere (**Figure 4a**), and from that we build up our metasurface adding complexity. As introduced in **chapter 1.3.2**, similarly to silicon spheres, rods, holes and discs[153–155], Si hemispheres support Mie resonances in the VIS and NIR wavelengths of electric and magnetic nature. For instance, a silicon hemisphere with a radius of 190 nm presents a magnetic dipole (MD) at λ = 1028 nm and an electric dipole (ED) at λ= 975 nm (**Figure 4a**). When these hemispheres are disposed in a hexagonal lattice of period *L*= 600 nm on a glass substrate (**Figure 4b**), the collective response of the array is still dominated by the single particle Mie resonances rather than by diffraction and surface lattice resonances (SLR) that are lost in the glass substrate.[135] An improved optical response can be achieved by placing the hemispheres onto a high refractive index waveguide. In our case a 400 nm thick high-index layer that supports quasi-guided modes (QGM) accessible from out of plane illumination via the hemisphere array (**Figure 4c, d**).[135] This configuration exhibits now a number of electric and magnetic resonances (**Figure 5**) in addition to the initial

magnetic and electric dipoles, MD and ED, that can still be found at λ = 930 nm and λ = 981 nm, respectively. Finally, the metasurface that we fabricated (**Figure 4d**), had a lower waveguide refractive index than that of pure silicon but still high enough to sustain the magnetic and electric resonances.

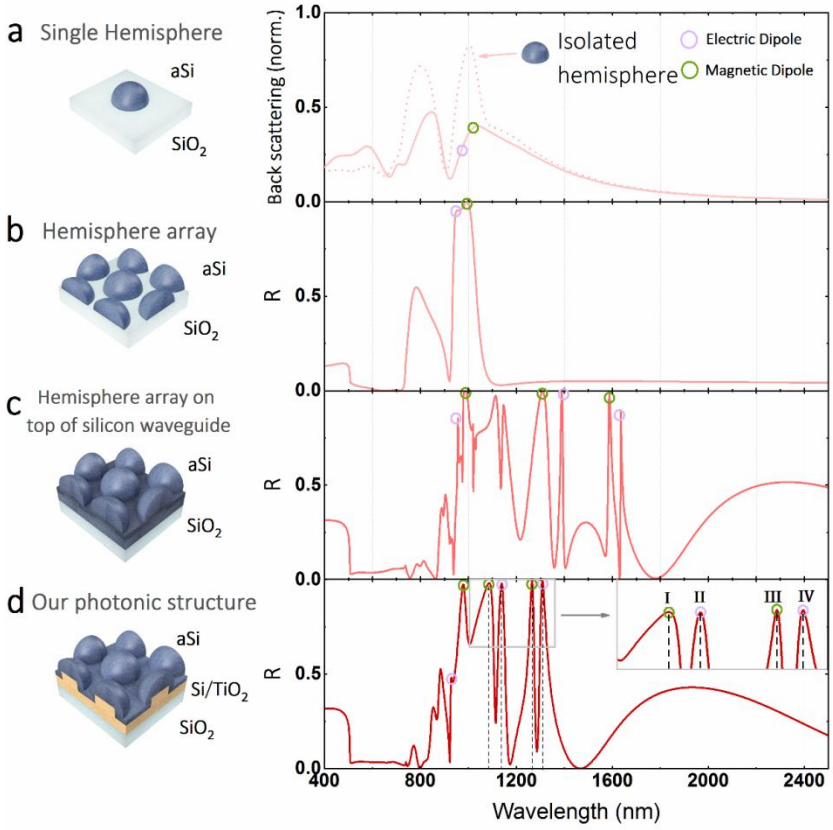

Figure 4. *Engineering of the optical response of the high-index dielectric metasurface via FDTD simulations. (**a**) Backscattering of a single silicon hemisphere (190 nm radius) self-standing (dotted line) vs on glass. Reflectance spectrum from a hexagonal hemisphere array with lattice parameter L=600 nm (**b**) on top of glass, (**c**) on top of a 400 nm silicon waveguide and (**d**) on top of a 400 nm Si/TiO_2 waveguide. Electric and magnetic dipolar resonances in each case are circled for clarity.*

A better insight in the origin of the resonances sustained by the fabricated metasurface could be obtained by looking at the electromagnetic field spatial distributions (**Figure 5**). The electric and magnetic fields inside the structure (**Figure 5**) confirmed the presence of two TE and two TM modes with a significant contribution from the QGM sustained by the high-index waveguide. The transversal electric modes TE_0 and the TE_1 appeared at 1309 nm and 1139 nm, respectively, and they presented a strong circulation of the magnetic fields in the hemisphere, thus conferring an

intense electrical dipolar moment on the particle (**Figure 5b and d**). We observed the same trend in the TM_0 and TM_1 modes placed at 1266 nm and 1086 nm, which presented strong MD in the hemisphere caused by the circulation of the electric field (**Figure 5a and c**). The circulation and distribution of the electromagnetic fields on the silicon hemisphere revealed the dipolar aspect of these resonances and the contribution from the QGM peaks.

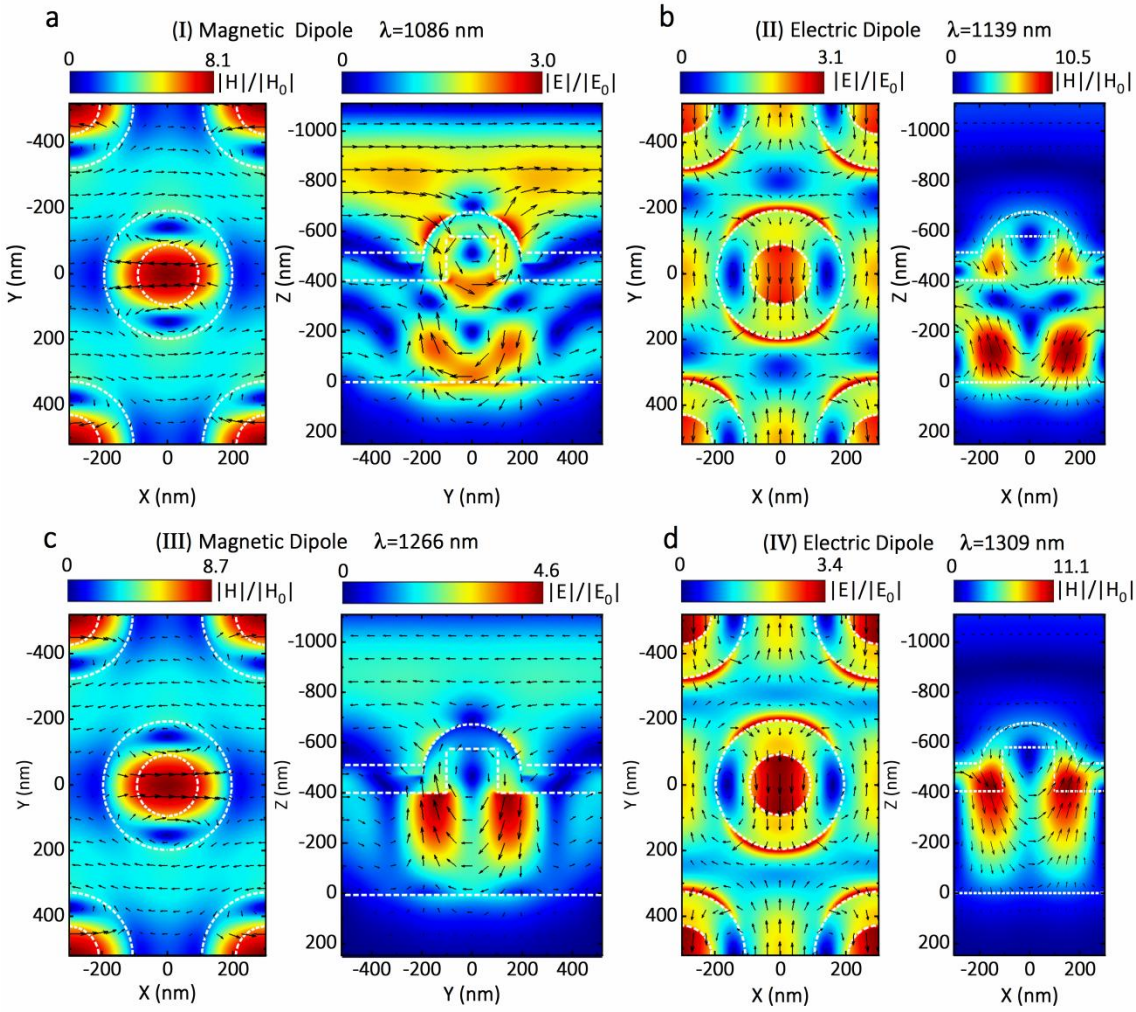

Figure 5. *Spatial distribution and nature of the electromagnetic fields for the different resonances highlighted in Figure 1d I-IV; namely (**a**) λ= 1086 nm (MD-TM_1), (**b**) λ= 1139 nm (ED-TE_1), (**c**) λ= 1266 nm (MD-TM_0) and (**d**) λ= 1309 nm (ED-TE_0). Vectors stand for the real part of the corresponding field in the plane*

In order to certify the contribution of the Mie resonances on the QGM we developed the multipolar decomposition of the metasurface, presented in **Figure 6**. Strong electric dipole contributions were present in the QGM at wavelengths 1309 nm and 1139 nm confirming the hybridized Mie-QGM nature of the resonances, describing them as ED-TE_0 and ED-TE_1 modes. Similar magnetic dipolar contributions were found for the Mie-QGM MD-TM_0 and MD-TM_1 at 1266 nm and 1086 nm respectively.

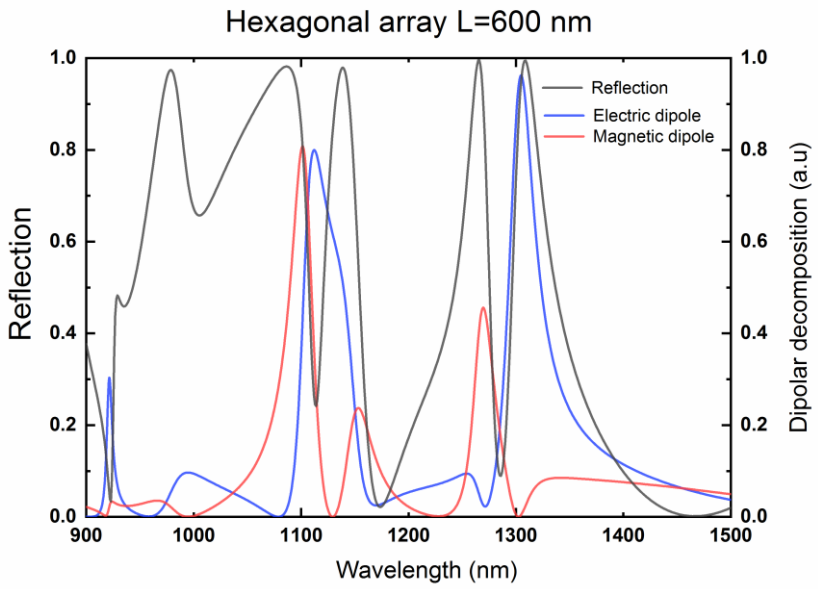

Figure 6. *Reflection of a hexagonal metasurface of L=600nm with the multipolar contribution decomposition of the hemisphere Mie resonances.*

For the decomposition in multipolar moments we represented the contribution to the scattering cross sections of the electric and magnetic dipole moments in the hemisphere, without the contribution of the substrate. The following expressions were used:

$$C_{sca}^{p} \propto |\boldsymbol{p}|^2 \tag{1}$$

$$C_{sca}^{m} \propto \frac{|\boldsymbol{m}|^2}{c} \tag{2}$$

$$\boldsymbol{p} = \int \boldsymbol{P} j_0(kr) d\boldsymbol{r} + \frac{k^2}{10} \int \left\{ [\boldsymbol{r} \cdot \boldsymbol{P}]\boldsymbol{r} - \frac{1}{3} r^2 \boldsymbol{P} \right\} \frac{15 j_2(kr)}{(kr)^2} d\boldsymbol{r} \tag{3}$$

$$\boldsymbol{m} = -\frac{i\omega}{2} \int [\boldsymbol{r} \times \boldsymbol{P}] \frac{3 j_1(kr)}{kr} \, d\boldsymbol{r} \tag{4}$$

Where p and m are the electric and magnetic dipoles, respectively, and j_n corresponds to the n-order spherical Bessel function. Being $P(r) = \varepsilon_0(\varepsilon_1 - \varepsilon_2)E(r)$, where ε_0, ε_1 and ε_2 are the vacuum permittivity, the relative dielectric permittivity inside the particle and the relative dielectric permittivity of the surrounding media, respectively. $E(r)$ is the electric field, calculated by means of finite elements (FDTD), inside the hemisphere. We also calculated the quadrupole and octupole moments expressions but turned out to be orders of magnitude lower than those of the electric and magnetic dipoles. These calculi were performed by Dr. Juan Luis García-Pomar.[156]

The spectral response upon variation of the angle of incidence of the impinging light for both TE and TM polarizations presented in **Figure 7** also provided a visual way to characterize the resonances provided by the metasurface. TE modes are insensitive to the angle variation in the TM polarization as well as the TM modes are to the angle variation in the TE polarization. These confirmed the TE and TM natures of the QGM. The Mie-QGM ED-TE_0 and ED-TE_1, with sharp reflection peaks located at 1309 nm and 1139 nm, showed almost no angle dependence in the TM polarization up to 30° while having a strong dependence with the angle variation in the TE polarization. Likewise, the Mie-QGM MD-TM_0 and MD-TM_1, with the reflection peaks located at 1266 nm and 1086 nm, respectively, were angle invariant in the TE while having a strong dependence with the angle variation in the TM polarization.

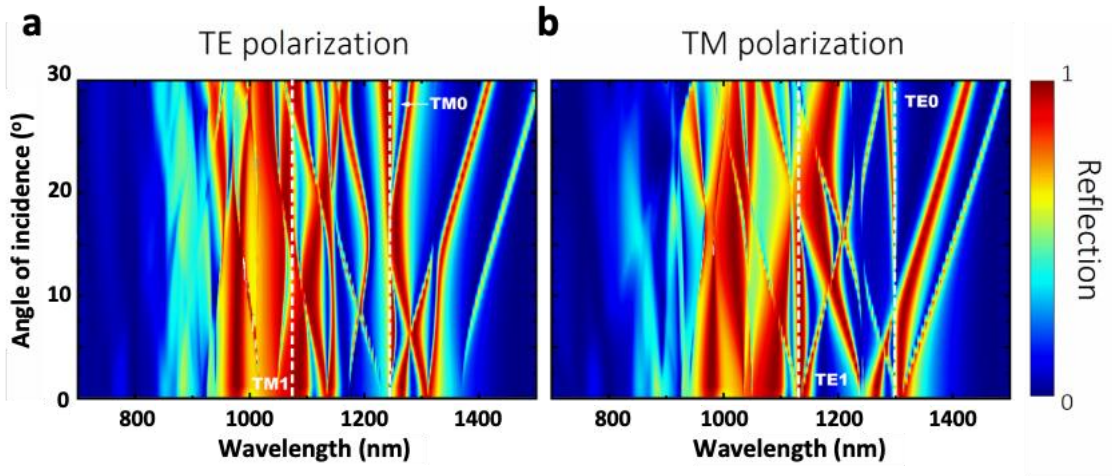

Figure 7. *Study of the reflection of a hexagonal metasurface of L=600nm upon angle variation of the impinging polarized light with (**a**) transversal electric and (**b**) magnetic configurations.*

These results indicate that our metasurface supported hybridized Mie-QGM with strong electromagnetic fields that can be exploited in many photonic applications. These can be shifted towards desired regions of the spectrum by changing essential parameters of the architecture, such as the waveguide thickness, the lattice parameter or the geometry of the periodicity, to match the desired applications. In **Figure 8** we analyze the effect of the waveguide thickness to support the quasi-guided modes. The slab thickness and the refractive index of the waveguide defined the number and spectral position of quasi-guided modes supported by the metasurface. As the thickness was increased, more quasi-guided modes were supported, and these are red-shifted.

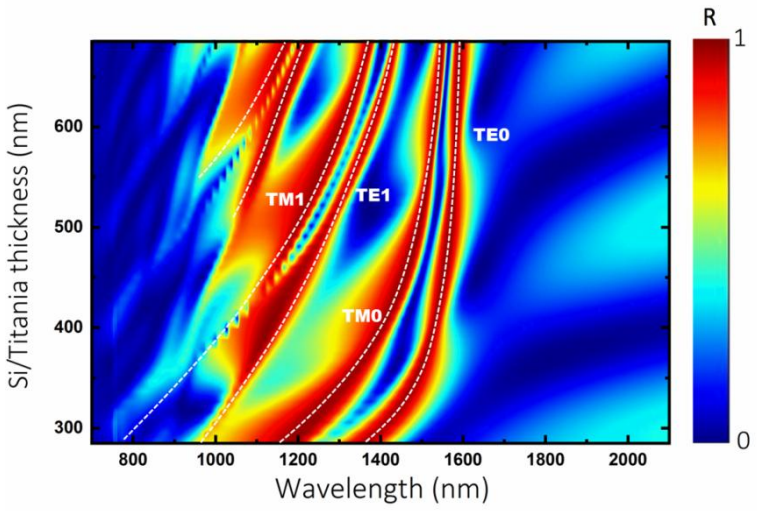

Figure 8. *Study of the reflectance versus the Si/TiO_2 waveguide thickness underneath the silicon hemispheres for a hexagonal metasurface with L=600 nm. (dash lines are guide to the eye).*

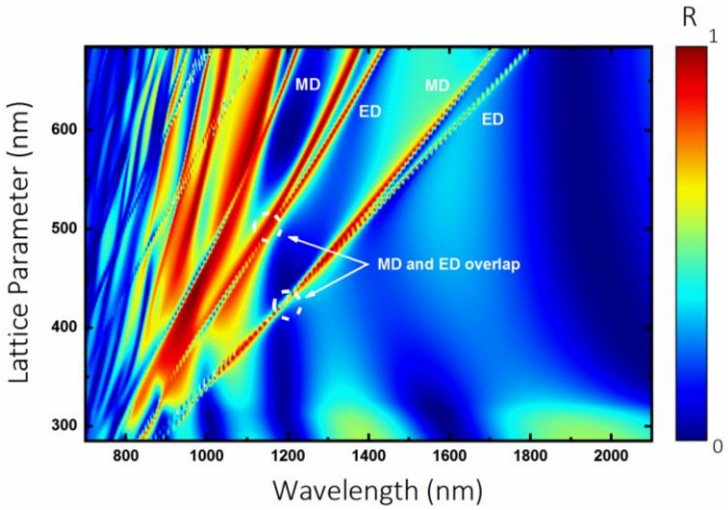

Figure 9. *Study of the reflection of hexagonal metasurfaces with the change of the lattice parameter. The hemisphere radius is r= 150 nm.*

We also investigated the possibilities that the change of the lattice parameter could offer. As shown in **Figure 9**, using architectures with different lattice parameters enables placing the Mie-QGM resonances in desired regions of the spectrum. With this idea we fabricated metasurfaces with lattice parameters ranging from 300 to 800 nm by using different pre-patterned hPDMS molds at the sNIL step (**Figure 10**). In this way, we had a set of samples with the Mie-QGM covering a wide spectral range from 800 to 2000 nm with the possibility to fit specific applications (**Figure 10**). The possibility to modify and overlap the position of the ED and MD might also induce the appearance of exotic optical properties in our structures. In the

calculations of **Figure 9,** at L ≈ 400 nm, an inversion of the spectral position of the ED-QGM with respect to the MD-QGM is predicted, as studied in previous reports.[137,154,157] The overlapping of these has recently been related with anomalous suppression of backscattering, called as the Kerker effect, and directional light propagation.[38,137,154]

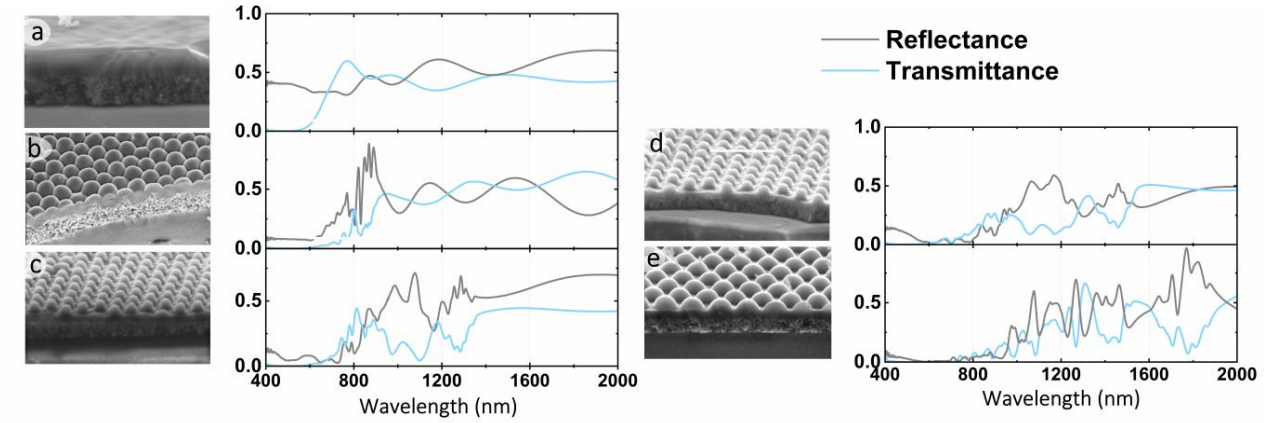

Figure 10. *Optical response of all dielectric metasurfaces with varying lattice parameter. SEM inclined view and reflectance (black) vs transmittance (blue) spectra of (**a**) flat reference sample and hexagonal metasurfaces with lattice parameters of (**b**) 300 nm, (**c**) 600 nm, (**d**) 700 nm and (**e**) 800 nm.*

The versatility of the technique also allowed us to explore other geometries, such as squared lattices which behaved similarly (**Figure 11**). The rectangular lattice arrangement offers the possibility to change the spectral position of the magnetic or the electric modes independently by increasing the pitch distance for each plane directions independently, as reported elsewhere.[157]

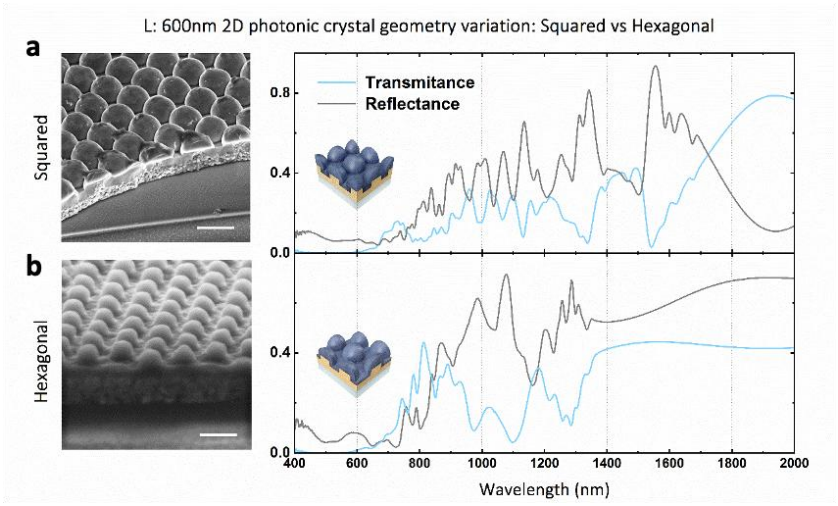

Figure 11. *Comparison of experimental reflectance (grey) and transmission (blue) in L=600 nm metasurfaces with squared (**a**) and (**b**) hexagonal lattices.*

4.3. Enhancing Photoluminescence with all dielectric metasurfaces

Finally, we tested the ability of our metasurface to act as a nanoantenna to enhance the photoluminescence (PL) of light emitters deposited on top of the structure (**Figure 12**), as a proof of principle to illustrate their photonic applications. The selected dye IR-140[158] (Sigma Aldrich) emits in the spectral range of 750-900 nm. The dye was dispersed, to a 0.35 wt% concentration in a biopolymer film made of a deoxyribonucleic acid (DNA)-cetyltrimethyl ammonium polymer matrix[159], which presents a low quenching contribution to the dye efficiency. An ethanol solution of DNA and dye was spin coated at 6000 rpm, giving rise to a film of few μm thickness. To maximize the interaction of the studied resonances with the dye we chose the architecture with *L*= 300 nm since the dipolar-QGM reflection peaks of this structure (**Figure 10b, and 12b**) matched well the emission of the dye. As a consequence, the PL spectra of the dye deposited on the metasurface was greatly reinforced with various peaks clearly distinguishable (**Figure 12b**). These peaks closely matched the positions of the optical resonances of the metasurface, as illustrated by reflection measurements.

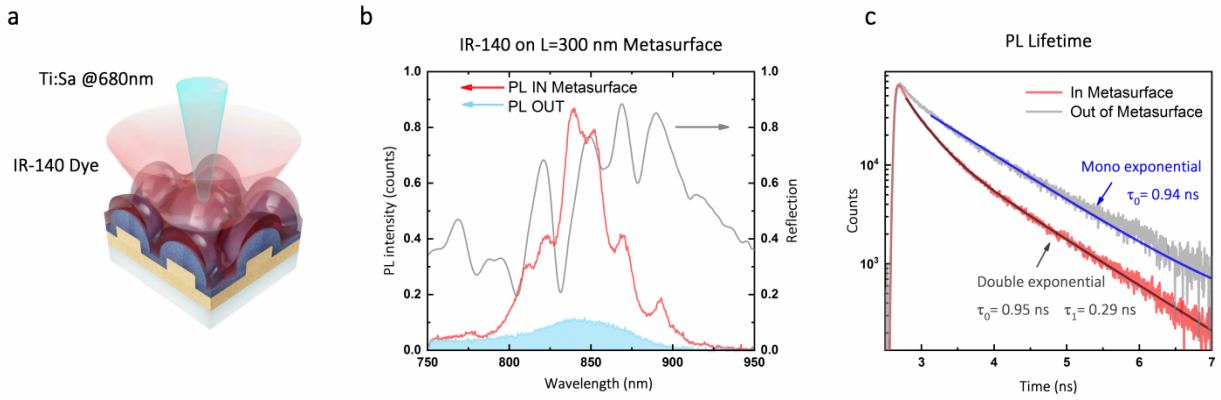

Figure 12. *Photoluminescence enhancement of a NIR dye on the metasurface. (**a**) Scheme of PL measurement configuration: the emission of the spin coated dye on the metasurface (L=300 nm) is excited by a Ti:Sapphire laser and collected in reflectance mode with a 5 cm lens. (**b**) PL intensity of the dye placed on the metasurface (red) vs on a planar Si substrate (blue). The reflection of the nanostructured substrate (gray) is included for comparison. (**c**) Time-resolved PL decay for emitters deposited on the metasurface (red) and on the reference substrate (grey) with their corresponding fitting curves.*

In order to certify the origin of the PL enhancement, we calculated electric and magnetic superficial energies of the L =300 nm metasurface, which are plotted in **Figure 13**. The enhanced electric and magnetic superficial energies provided by the designed Mie-QGM at the resonant wavelengths of 896, 874 and 838 nm endowed the system with increased PL emission, exhibiting

a maximum 8.1-fold enhancement from a flat sample with equivalent dielectric contrast. For the superficial energy ($\boldsymbol{S_e}$) evaluation, the following expressions were used (**eq.5-7**):

$$S_e = \frac{\int W_t ds}{\int ds} = \frac{\int W_e ds + \int W_m ds}{\int ds} \tag{5}$$

$$W_e = \frac{1}{2} E \cdot D \tag{6}$$

$$W_m = \frac{1}{2} B \cdot H \tag{7}$$

Where W_e and W_m are the electric and magnetic energies respectively. This finding illustrates the great potential for coupling between the metasurface modes and the emitters. Moreover, to further characterize the interaction, we evaluated how the increased density of electromagnetic states in the near-field of the metasurface increased the decay rate reducing the PL lifetime (Purcell effect). We measured the time-resolved PL of the emitters on the sample and on the reference plane (**Figure 12c**). The former showed a faster decay, a shortened PL lifetime, which indicated a more efficient PL response with an enhanced spontaneous emission rate. In particular, the time resolved emission of the dye on the planar sample followed a mono-exponential decay (with τ = 0.94 ns), while a double exponential decay was found when the dye was placed on the metasurface (with τ_0 = 0.95 ns and τ_1 = 0.29 ns). Interestingly, the slow component of the double exponential decay (τ_0) was consistent with the intrinsic lifetime of the dye on the reference plane, indicating that it originated from the molecules that do not interact with the Mie-QGM resonances. Finally, we evaluated the Purcell factor (P) of spontaneous emission rate as $P = \tau_1^{-1} - \tau_0^{-1} = 2.4$ by using the relationship found in previous reports.[160]

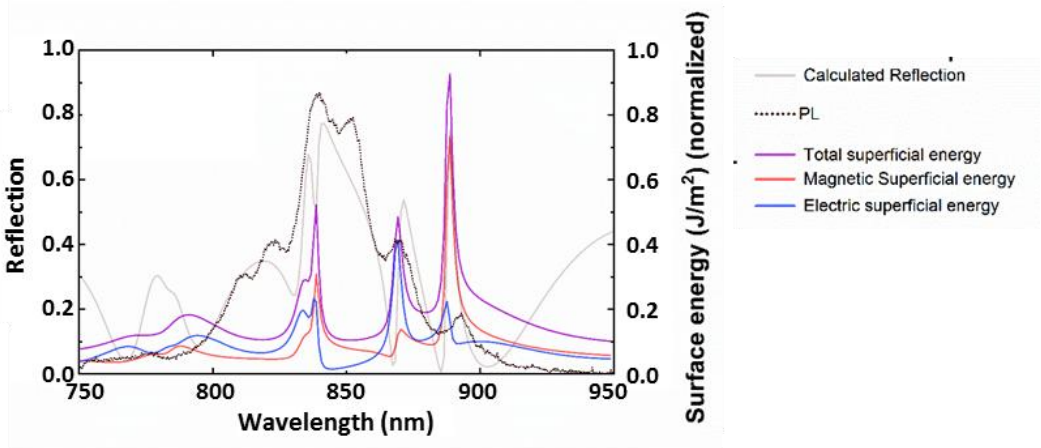

Figure 13. *Calculated reflectance (grey) and total superficial energy (violet), both magnetic (red) and electric (blue), of the L=300 nm hexagonal metasurface used in the photoluminescence emission measurements (black dotted line) of the studied IR-140 dye.*

4.4. Conclusions

We designed and fabricated a full dielectric metasurface. This was composed of a 2D array of silicon hemispheres on a silicon-infiltrated titania (Si/TiO_2) waveguide. This inventive architecture was designed to simultaneously sustain Mie resonances from the hemispheres and quasi-guided modes. Interestingly, these architectures were easily fabricated via highly scalable techniques, a long sought goal in the field of high dielectric nanostructures.

The backbone of the metasurface, consisting of an ordered array of pillars over a waveguide layer, was composed of a commercial anatase m-TiO_2 paste. The reasons to choose this material were three: First, it is easy to nanopattern by solvent assisted soft NIL; secondly, it is highly temperature resistant, so it can stand the silicon deposition conditions; and third, anatase TiO_2 has one of the highest refractive index amongst visible transparent materials, which is essential for light guiding, as introduced in **chapter 1.2.2**.

The role of the silicon was to provide with a spherical resonator to sustain the Mie modes and to raise the refractive index of the waveguide layer. The low pressure CVD growth allowed the silicon to infiltrate in the m-TiO_2, which enhanced the light confinement in the structure. In the other hand, the conformal growth of the silicon over the TiO_2 pillars ended up with the formation of hemispheres with a polydispersity of 3%.

These silicon hemispheres sustained strong magnetic and electric Mie modes, which are appealing for plenty of photonic applications, as introduced in **chapter 1.3.2**. At the same time, these resonant modes coupled to the guided modes of the high refractive index waveguide thanks to the diffraction granted by the periodic lattice. The hybridization of these modes provided with high extinction peaks of electric and magnetic nature. Such resonances rendered the metasurface with enhanced superficial energy. This intense field enhancement has many applications that we illustrated with the enhanced photoluminescence from a NIR dye placed atop, obtaining an 8.1-fold PL enhancement with an enhanced Purcell effect.

Finally, we demonstrated the versatility of the technique and how the spectral position of the resonances can be tuned. We provided the key guidelines to optimize the substrate efficiency and response for different applications by varying its geometrical parameters.

Chapter 5

5. Coupling light into optoelectronic devices via diffraction-guided modes

5.1. Introduction to diffraction-guided modes

As explained in **chapter 1.3**, diffraction and guided resonances are two of the main tools that one can use to manipulate light at the nanoscale. The hybridization between the two modes has been extensively used in the field of sensing[161], light harvesting[162], optical communication[163] and spectroscopy[164] among others, up to the point that it became a field on its own. Coupling light with diffraction began in 1902 when Robert W. Wood turned his attention to the sudden variations and suppression of the intensity of reflected light in diffraction modes of gratings.[165] Five years later, Lord Rayleigh provided the first explanation, suggesting that these anomalies in light reflectance where related to the coupling of diffracted modes to evanescent modes in the surface.[166] Later on these resonances would be also called "Wood's, or Rayleigh-Wood's anomalies" (RAs). Other significant contributions from Fano in 1941, Hessel and Oliner, and finally Maystre in 1972, ended up with a description of the electromagnetic mode behind those anomalies.[167–169] The latter finally experimentally demonstrating that the extinction of the reflected diffraction modes was due to the coupling to leaky guided surface waves with various intensities. Nowadays, such gratings that support leaky guided surface modes, also known as quasi-guided modes, are referred to as resonant waveguide gratings (RWG) (**Figure1**). These can be defined as a thin waveguide film with an optical grating, similar to the structure developed in **chapter 4**.

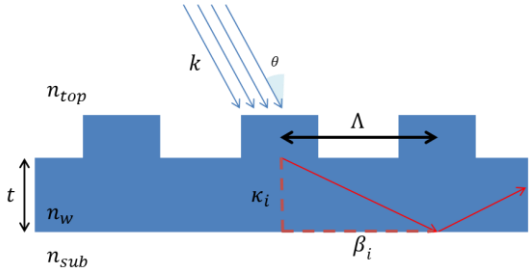

Figure 1. *Schematic of an impinging light on a RWG. The diffraction grating provides enough parallel momentum to the impinging light to match the propagation constant of the guided modes.*

In RWG, the optical grating provides the structure with the diffraction modes which will modify the transverse momentum of impinging light, allowing it to couple to the guided modes of the underlying waveguide layer. The number of quasi guided modes that are allowed depend on the waveguide thickness (**Figure 2a**). If the waveguide is very thin, the number of available modes get reduced until we are left with the fundamental mode, the one with the lowest cut-off frequency (**Figure 2b**)**.** If the grating depth is shallow enough, we can calculate analytically which modes are allowed inside the RWG, treating it as a pure slab waveguide.[170] However, we must impose the propagation wavevector ($k_{//}$) to be equal to the wavevector of the light diffracted by the grating. In this way, we are selecting the guided modes that can be excited through the diffraction grating. The expression for the allowed (i) modes read as:

$$\tan(\kappa_i t) = \frac{\kappa_i(\gamma_i + \delta_i)}{\kappa_i^2 - \gamma_i\delta_i} \qquad \text{For TE modes} \qquad (1)$$

$$\tan(\kappa_i t) = \frac{n_w^2\kappa_i(n_{sub}^2\gamma_i + n_{top}^2\delta_i)}{n_{sub}^2 n_{top}^2\kappa_i^2 - n_w^2\gamma_i\delta_i} \qquad \text{For TM modes} \qquad (2)$$

With:

$$\kappa_i = \sqrt{n_w^2 k^2 - {k_{//}}_i^2} \qquad (3)$$

$$\gamma_i = \sqrt{{k_{//}}_i^2 - n_{top}^2 k^2} \qquad (4)$$

$$\delta_i = \sqrt{{k_{//}}_i^2 - n_{sub}^2 k^2} \qquad (5)$$

$${k_{//}}_i = k\left(n_{top}\sin\theta - \frac{m\lambda}{\Lambda}\right) \qquad (6)$$

$$k = \frac{2\pi}{\lambda} \qquad (7)$$

Where λ is the wavelength; θ, the illumination angle; Λ, the grating period; i, the guided mode order; m, the grating diffraction order; and n_{top}, n_w and n_{sub} are the refractive indexes of the impinging media, the RWG and the substrate, respectively. By solving equations 1 and 2, we can analytically predict the TE and TM guided modes that can be excited, as presented in **Figure 2a**. In **Figure 2b** is shown how for thin films only the fundamental mode is allowed, whereas if the thickness is increased, the successive modes, 1st and 2nd, are also permitted

(**Figure 2c and d,** respectively). Gratings with shallow features will exhibit better guided modes which are translated to spectrally narrower resonances but low coupling efficiencies. In the other side, deep gratings will have higher scattering cross sections but with more damped resonances, leading to spectrally broader peaks.

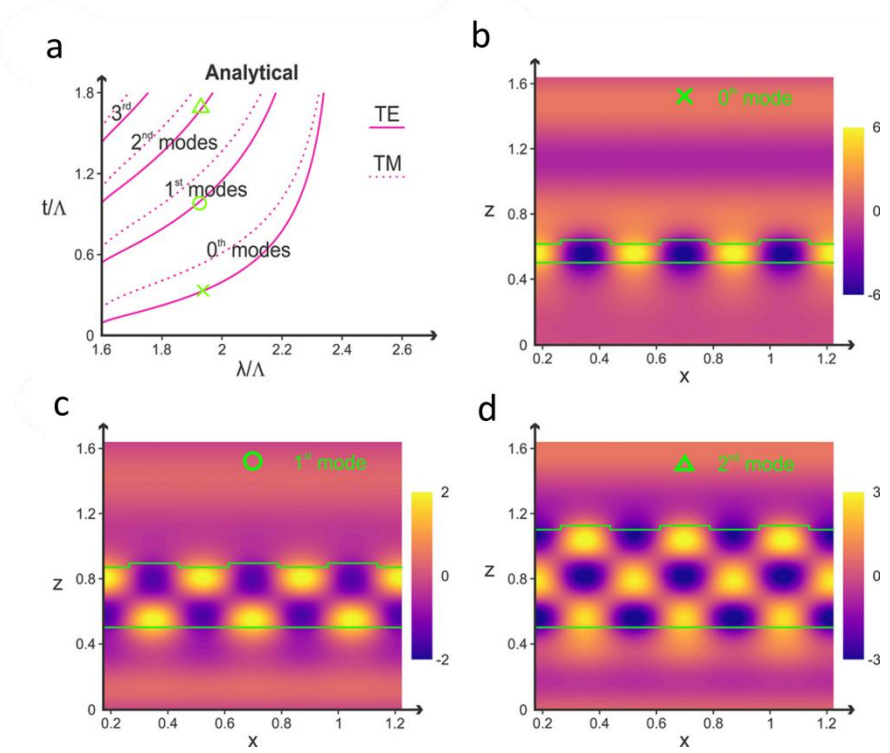

Figure 2. *Example of a resonant waveguide grating. (**a**) Guided modes allowed, both TE and TM (solid and dotted, respectively) calculated analytically as a function of the thickness of the waveguide and the grating period. (**b-d**) Electric field profiles for TE guided modes at the same wavelength for three RWG with increasing thickness.*[170]

Developments in analytical and computational methods, which enabled to control the near and far field electromagnetic profile of the available QGM modes, have skyrocketed the applications of RWGs, some of them summarized in **Figure 3**.[171–173] The most extended application for the RWG is to work as a grating coupler for planar waveguides, which has been implemented since the 1960s.[174] Currently, RWGs are also being used in light filtering[161], as focusing elements[175], to enhance non-linear effects[176], to achieve electromagnetic induced transparency[177], as refractive index biosensors[161], as absorbers[162], as fluorescence enhancing substrates, in wavelength division demultiplexers[163], as polarizers[178], as polarization beam splitters[179], in spectrophotometers[164], as active tunable filters[180] and in security as anti-counterfeiting designs[181], among others.

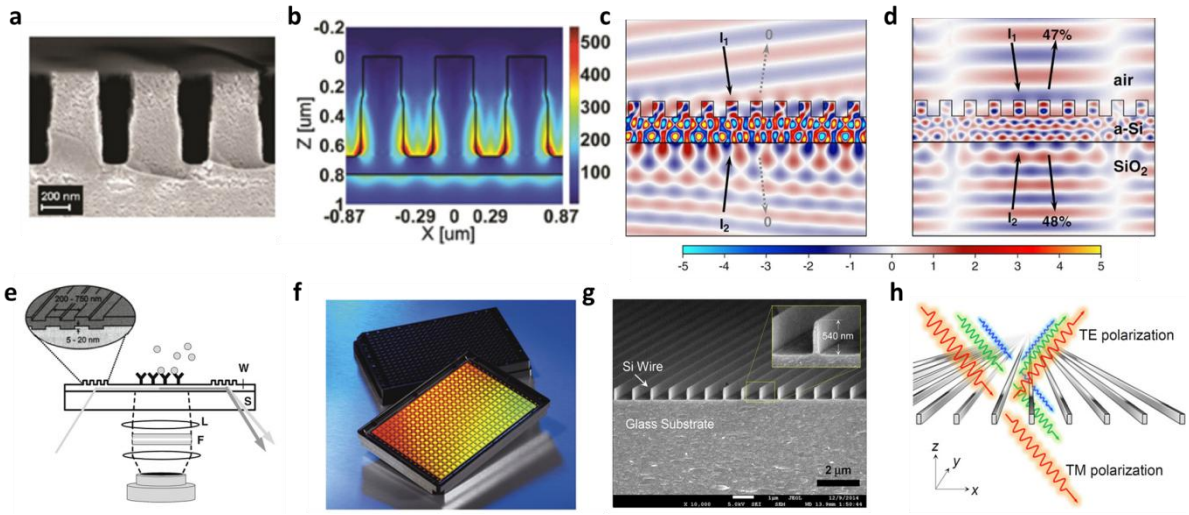

Figure 3. *Examples of RWG applications. (**a**) SEM of a SiN grating used for UV Third harmonic generation and (**b**) its profile of the electric field intensity responsible of the non-linear effect enhancement.*[176] *(**c**) Magnetic field intensity in a coherent perfect absorber when the two TM incident beams are in phase, leading to perfect absorption, and (**d**) out of phase.*[162] *(**e**) Schematic drawing for a RWG based biosensor and its macroscopic appearance (**f**).*[161] *(**g**) SEM and (**h**) process scheme of an ultra-sparse TE reflector.* [178]

The advances in RWG and their applications have not been only increased by the modern computational methods and algorithms but also by the massive advances in nanofabrication. Higher quality of the features and more homogeneity and reproducibility are needed to obtain efficient gratings with the optimum resonances. Among other lithography techniques, the most used ones for RWG fabrication are interference laser lithography[182], electron beam lithography[183], laser ablation[184], anisotropic etching[185] and nanoimprint lithography.[81] As seen in previous chapters, soft NIL is undoubtedly a promising technique for fabricating patterned substrates with high resolution, a low cost and in a large scalable way; that can be used to manage light at the nanoscale.[2,3] However, the seamlessly implementation of these structures in optoelectronic devices is not trivial. Often, nanostructuration of the layers of an optoelectronic device results in deterioration of some other properties while trying to enhance its optical properties. Lower photoluminescence quantum yields in light emitting devices, lower filling factors with higher recombination rates in solar cells and higher dark currents and non-linearities in photodetectors are amongst the typical consequences of the introduction of an external element within the device.

In this chapter we explore the implementation of 2D photonic crystals acting as RWG in a series of optoelectronic devices: a solar cell, a photodetector and a light emitting layer. First, we introduce the background of the type of device, its applications, and the need for a photonic improvement. Secondly, we analyze and design how the photonic structure could be implemented. A conscious pick of the materials used and the geometrical parameters is crucial for the correct functioning of the device. Finally, we fabricate the device and evaluate its optical and electronic properties.

5.2. Nanostructured colloidal quantum dot solar cells for enhanced infrared efficiency

5.2.1. Introduction to colloidal quantum dot solar cells

Colloidal quantum dots (CQDs) combine bandgap tunability with low manufacturing cost facilitated by solution processing.[186] Lead chalcogenide CQDs provide absorption and emission tuned into the infrared region (IR) of the solar spectrum – a regime of interest in sensing[187], machine vision, autonomous driving and solar energy harvesting.[188] IR CQDs can potentially extend the response of photovoltaic technologies further into the IR range, acting as the back cell in a tandem structure with metal-organic halide perovskite (Eg = 1.58 ~ 1.68 eV) or Si (Eg = 1.1 eV) solar cells.[189,190] The solar spectrum contains up to 15 mA/cm^2 of potential short-circuit current beyond 1100 nm (**Figure 4a**), a total 7% extra power conversion efficiency (PCE) on top of c-Si.[190] The absorption coefficient of lead chalcogenides in the IR range is ~ 10^4 cm^{-1} at the excitonic peak. Thus, ~ 1 µm of active layer material is needed in a conventional planar device to fully absorb IR photons from 1100 to 1800 nm. Unfortunately, the carrier diffusion lengths in solid CQDs are limited to a few hundred nanometers. This absorption-extraction trade-off has so far limited the efficiency of IR photon harvesting to 3.9% and 1.1% beyond the perovskite and c-Si absorption limits, respectively.[191] Light management strategies have been sought to increase CQDs absorption in the IR range to overcome the absorption-extraction compromise. These include the use of multilayers as cavities[192–194], plasmonic nanoparticles[47,109,195–197] and grating structures.[1,198] In particular, nanostructuring of the metal back mirror has been advanced as a means to enhance absorption by increasing the optical path within the active layer of the material.[199,200] To date, though, the realization of structured CQD solar cells has come at a cost to backside charge collection and has been accompanied by increased surface recombination.

For semiconducting materials such as organics[201,202] and perovskites[203], direct PDMS imprinting of the active layer before metal evaporation has previously been used to form back photonic electrode structures.[201,202] It comes by no surprise the fact that this nanoimprinting method has been widely used in solvent based solar cells due to its easy implementation. Also, patterning the active layer, which is often the thickest deposited layer of the solar cell, allows to develop bigger structures with stronger scattering efficiencies. In the case of CQD solar cells, a structured active layer has been formed by spin-casting CQDs onto a corrugated mold-on-substrate; and then transferring the now-backside-structured active layer onto a new electron transport layer (ETL) stack. However, this approach does not deliver a significant net advance

in PCE because it is accompanied by increased surface recombination leading to V_{oc} and *FF* losses.[1,198] Alternative approaches such as molding the hole transport layer (HTL) have so far been precluded by the rigidity of the EDT-treated (1,2-ethanedithiol) CQD HTL layer.

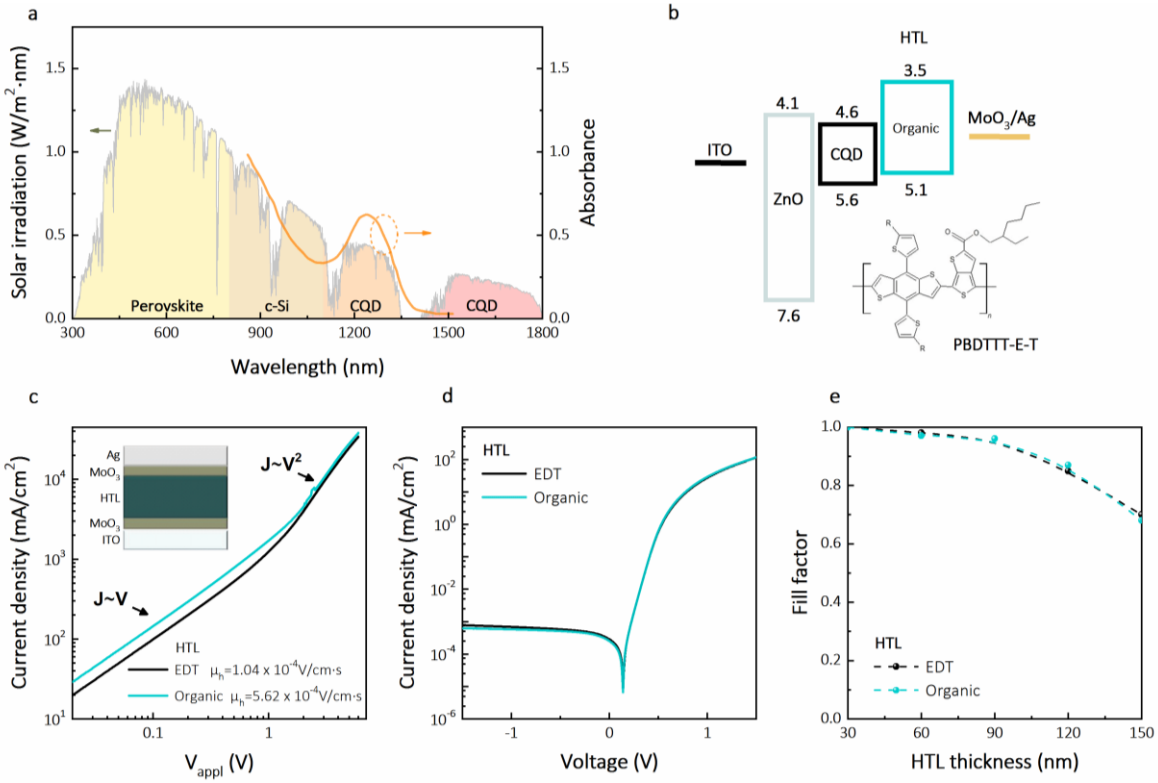

Figure 4. *(**a**) AM 1.5 Solar irradiation (left) versus range of operation of widely used solar technologies and absorbance curves of infrared CQD with different crystal size (right). (**b**) Energy level diagram of full CQD device structure and chemical structure of organic polymer used as an HTL. (**c**) Hole mobility of EDT (black) and organic (blue) HTL respectively. (**d**) J-V curves under dark conditions of CQD-EDT (black) and organic (blue) HTL. (**e**) FF dependence of IR CQD devices with the thickness of the HTL layer for CQD-EDT- (blue) and organic-deposited (black) HTL.*

In this section we describe a method to achieve enhanced IR light trapping and simultaneously provide efficient hole extraction in lead sulfide (PbS) CQD solar cells. We first examine the colloidal quantum dot solar cell and determine in which layer and how we can introduce a photonic structure to avoid disrupting the electrical properties. Afterwards, we design the photonic structure to maximize the absorption in the infrared range beyond 1100 nm and the way to introduce the nanostructuration seamlessly into the fabrication scheme. Later on we proceed with the fabrication of the solar cell and finally we present the optical and electrical characterization. This work was done in collaboration with the Prof. Ted Sargent group at the University of Toronto.

5.2.2. The device: IR colloidal quantum dot solar cell

5.2.2.1. Composition

The CQD solar cells fabricated and studied in this work had the usual solar cell layered structure, with its band gap diagram shown in **Figure 4b.** The layered structure comprises a transparent electrode of indium tin oxide (ITO) followed by an ETL of zinc oxide, the active layer of CQDs, the main HTL, the composition of which will be detailed in the next paragraph (as it is the layer of main interest), an extra nanometric HTL of Molibdenum trioxide (MoO3) and the silver back contact. The CQDs used were oleate-caped PbS CQDs synthesized with a recipe developed by the Ted Sargent's group[203], which present an excitonic peak at 1220 nm and have an average refractive index of 2.5 in the NIR range (obtained from ellipsometry measurements). Regarding the main HTL, best CQD solar cell IR performances up to date use a 40 nm EDT-treated CQD layer.[191] However, the attempts to nanostructure this HTL were hampered by its rigidity. Therefore, we sought to replace conventional EDT HTLs with new materials that were compatible with soft NIL. The optimal HTL should be easily deformed by gently pressing with the PDMS mold with minimal chemical interaction. From an optoelectronic standpoint, the HTL would require appropriate band alignment with the CQD active layer, with HOMO (highest occupied molecular orbital) levels similar to EDT. Also, it must have sufficient charge carrier mobility for holes to enable the incorporation of a relatively thick layer (around 100 nm) with efficient hole extraction. This thickness is required to imprint features relevant to the spectral regime of interest, since lower structures may not have enough impact in the optics of the system.

Amongst the possible candidates, we selected PBDTTT-E-T, a copolymer of benzo[1,2-b:4,5-b']dithio-phene (BDT) and thieno[3,4-b]thiophene (TT)[206], which exhibited the highest yield of extraction of photogenerated carriers, good charge transport properties and adequate surface tension during self-assembly.

We compared the performance of the candidate organic HTL with that of conventional EDT-treated CQD (CQD-EDT) layers. We used the space charge limited current (SCLC) method to estimate mobility.[207] The overall structure of SCLC devices was ITO/MoO_3/HTL (EDT-CQD or the organic layer)/MoO_3/Ag (**Figure 4c**). The layer of MoO_3 was deposited on ITO as an electron-blocking layer in this electrode. The measured hole mobilities for the CQD-EDT and PBDTTT-E-T were 1 x 10^{-4} V/cm·s and 6 x 10^{-4} V/cm·s respectively, indicating that the organic

layer provides a hole mobility advantage relative to the conventional approach. Those are similar mobilities as in previous reports. [208,209]

To test further the performance of this new organic HTL, we fabricated full CQD devices including this layer in an ITO/ZnO/IR CQD layer/HTL/MoO_3/Ag configuration and characterized current-voltage characteristics under dark conditions. Both HTLs exhibit comparable transport properties at similar thicknesses (~ 65 nm) (**Figure 4d**). We tracked the *FF* of both devices as a function of HTL thickness as thicker HTLs would allow the incorporation of photonic structures with deeper corrugation and stronger scattering efficiency (**Figure 4e).** The CQD device that used the PBDTTT-E-T HTL maintained 83 ~ 85% of the initial *FF* until 100 nm thick of HTL under 1 sun illumination.

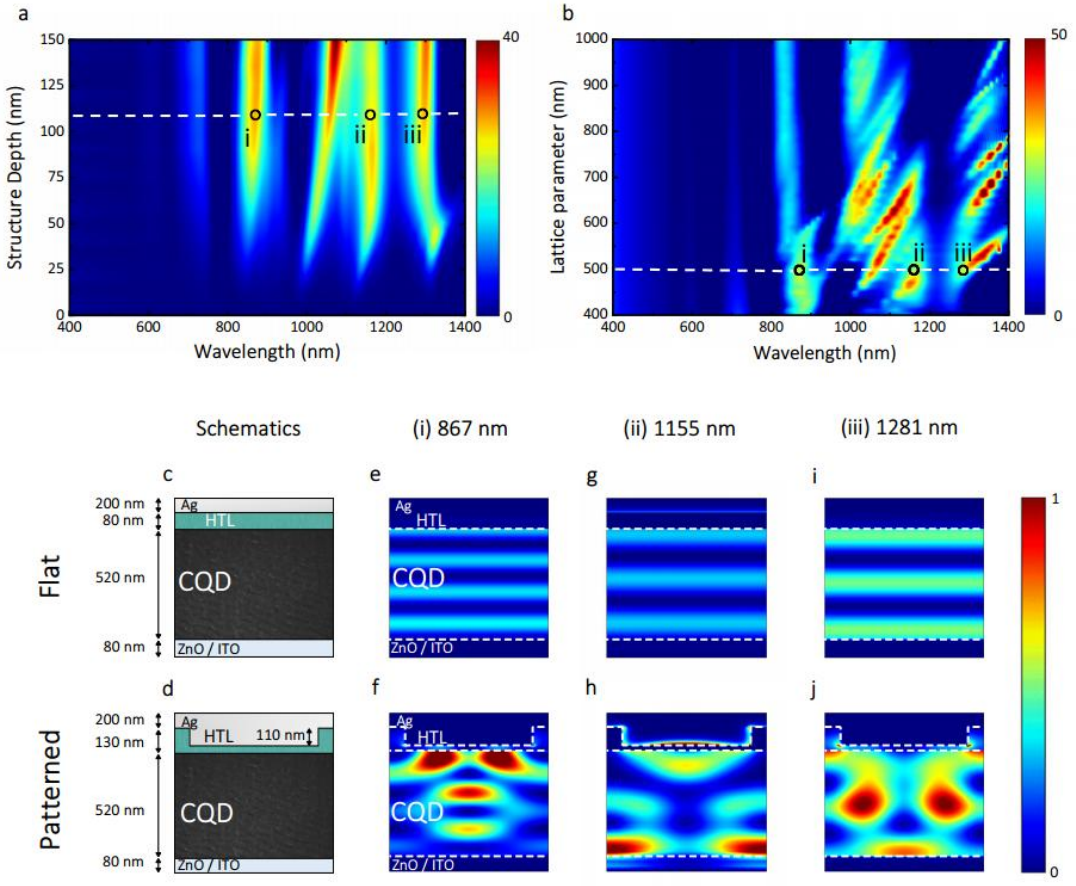

Figure 5. *(**a**) Calculated absorption enhancement for patterned 520nm thick IR CQD active layers at normal incidence as a function of wavelength and structure depth and (**b**) structure lattice parameter L. Schematic cross-sections of flat (**c**) and patterned (**d**) devices and cross-sectional absorption maps at enhancement wavelength peaks: 867 nm (**e**) (**f**) 1155 nm (**g**) (**h**) 1281 nm (**i**), (**j**) for flat and imprinted devices respectively.*

5.2.2.2. The light trapping scheme

We then sought to design photonic nanostructures that enhance IR absorption using FDTD modeling. In our simulations (**Figure 5**), we studied the influence of the geometry of the photonic structure, but restricted the thicknesses of the active and electron/hole transport layers to those compatible with efficient optoelectronic operation (e.g., maximum HTL layer thickness was restricted to 150 nm). We focused our attention on photonic architectures formed by square arrays of cylindrical holes, a 2D photonic crystal, which have shown to produce broad light absorption enhancement in thin film systems.[155] The absorption enhancement was calculated respect to a planar device with the same active layer thickness and 80 nm HTL thickness – the optimal planar device with the highest PCE. We began by exploring the lattice periodicity (*L*) and the depth of the cylinders in the HTL (h) to tune the enhancement towards the wavelengths of interest and maximize its intensity (**Figures 5a**-**b**). The depth of the cylinder enables the system with photonic modes (**Figure 5a**) whose position can be tuned with the lattice parameter (**Figure 5b**). Theoretically, features with depths beyond 100 nm could provide stronger scattering from the photonic structure, but this would be at the expense of diminished electrical transport, as well as increasing the risk of shunting.

In **Figure 5b** we can differentiate the photonic modes sustained by the photonic crystal in the solar cell. In this diagram, we encounter modes whose frequency remains invariant to changes in the lattice parameter such as the resonance observed at 867 nm (**i**, **Figure 5b**). The absorption enhancement peaks whose frequency depends on the lattice parameter are highlighted in **Figure 5b** as **ii**, **iii**. At these wavelengths, the backscattered light of the photonic electrode couples to the photonic resonances specifically provided by the periodicity of the array, being trapped within the active layer of the material. Further insight can be gained by studying the spatial distribution of the power absorbed at the resonances **i**, **ii**, **iii** from **Figure 4b** for the planar and the photonic electrode configuration. The flat architectures (**Figure 5e, g, i**) present a standing wave absorption profile while patterned devices (**Figures 5f, h, j**) show higher overall absorptions and distinct electromagnetic field profiles. The resonance appearing at 867 nm (**i**) is located around the cylinder structure following its dipolar mode (**Figures 4f**), whereas resonances located at 1155 and 1281 nm correspond to lattice modes caused by the diffraction of the 2D photonic crystal into the CQD film (**Figures 5 h** and **j**).

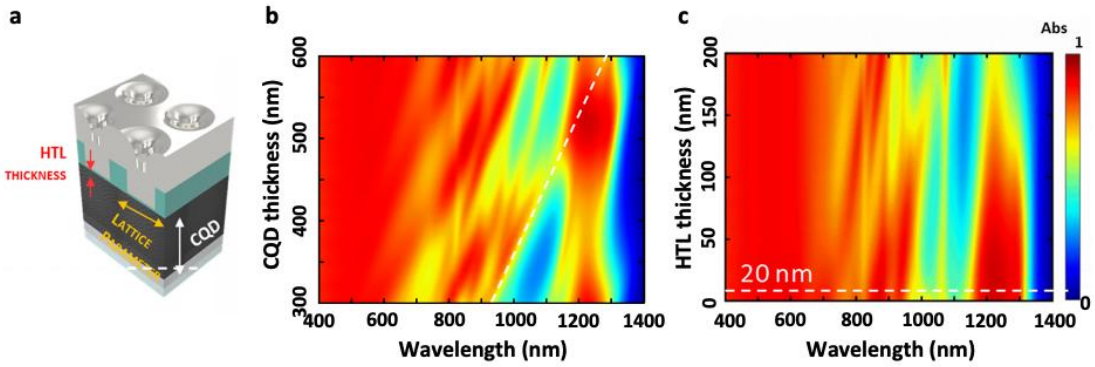

Figure 6. *(**a**) Schematic of the designed device and the FDTD calculation parameters. The absorption changes of the CQD layer as a function of wavelength and (**b**) CQD thickness and (**c**) HTL thickness at the base of the structure.*

From our simulations, the photonic architecture that maximizes IR absorption near the 1100-1400 nm region (near the excitonic peak) consists of a square array of 110 nm deep holes in the organic HTL with a periodicity of *L* = 500 nm over a 520 nm thick IR CQDs layer (**Figure 5d**, **6a**). By doing so, we achieved absorption peaks of +30% at 1155 nm and 1281 nm and even achieved a 10% extra absorption at the maximum of the excitonic peak at 1220 nm. The thickness of the active layer has also been optimized by FDTD simulations obtaining an optimum the mentioned value of 520 nm. In **Figure 6b** we can observe how a thickness dependent photonic mode (white dashed line) overlaps the excitonic peak at that precise thickness boosting the absorption in the IR. Also, we resolved that the structures that better perform optically are those with the minimum amount of HTL in the base of the structure (**Figure 6c**). However, we have to leave at least a minimum amount of around 20 nm to avoid undesired recombination effects due to pinning holes.

5.2.3. Fabrication of the nanostructured CQD solar cell

The preferred array pattern was implemented into CQD devices with the aid of sNIL[2,3], an approach already presented in **chapter 2.2.2.2**. First, the deposition of the ZnO and CQDs layers, as well as the CQDs fabrication, was carried out by spin coating following previous reports.[204,205] Then, we spin-casted the organic HTL onto the flat CQDs film on a Glass/ITO/ZnO substrate. Immediately following spin coating, and while the polymer was still wet, we gently pressed the hPDMS stamp against the sample for 2 min (**Figure 7a**). The spinning time was reduced from 30 to 7 s to ensure that the polymer was still wet when the rotation was over. If the spinning time was too long and the solvent completely dried, we were

not able to pattern the layer. After we removed the stamp, the organic layer showed consistent iridescence across the region of indentation. Atomic force microscopy (AFM) revealed the resulting 2D hole squared array structure to have 110 nm depth from the 130 nm total thickness of the HTL (**Figure 7b**)**.** The nanostructured layer produced via NIL retains a residual layer of imprinted material (in our case, 20 nm) that prevents completely perforating the imprinted film: this is important to prevent shunts. SEM cross sectional images revealed the morphology for the photonic HTL structure (**Figure 7c**).

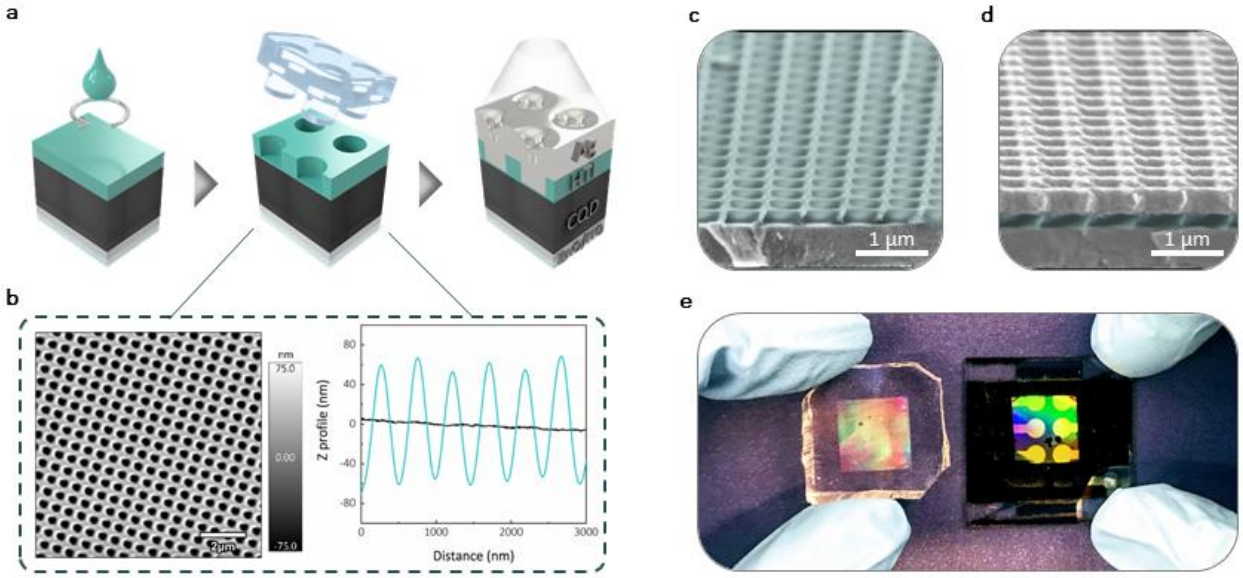

Figure 7. *(**a**) Schematics of the PDMS imprinting process in CQD devices. (**b**) Surface images and line profile of organic layer scanned by AFM after imprinting. Scale bar: 2 µm (**c**) SEM images of organic hole transporting template after imprinting (left) and (**d**) final metal structure deposited onto the organic template. (**e**) Photograph of the pre-patterned PDMS mold (left) and the final IR CQD device after nanoimprinting (right).*

To complete the devices, we thermally evaporated 20 nm of MoO_3 and 400 nm of Ag on top of the patterned HTL. The thick silver layer provided a smooth and uniform coating of the organic template, retaining thereby the structures (**Figure 7d**) designed with the aid of FDTD. The final CQD devices retained the desired diffraction of light as viewed from the electrode side (**Figure 7e**).

5.2.4. Optical and electrical characterization of the nanostructured device

The external quantum efficiency of IR CQD solar cells exhibited broad spectral responses from 350 nm to 1400 nm and strong excitonic peaks near 1220 nm (**Figure 8a**)**.** The photonic electrodes led to a 14% J_{sc} enhancement, raising the original J_{sc} of 32 mA/cm^2 of flat devices to 36 mA/cm^2 in patterned ones. The EQE improved across the entire 350-1400 nm spectral range and was most significant in the IR range 1000 nm to 1400 nm. With a maximum EQE of 86% at 1220 nm, these photonic electrode devices set a new record EQE relative to prior IR CQD photoelectric devices, including both solar cells and photodetectors.[210]

To ascertain the origin of the EQE enhancement, we compared the measured absorption (A) and measured EQE of each device, both flat and patterned devices (**Figure 9**). Their spectral features correlated closely between A(λ) and EQE(λ). Correspondingly, the estimated internal quantum efficiency (IQE) was comparable, and varied minimally with λ, for flat and patterned devices (**Figure 8a**).

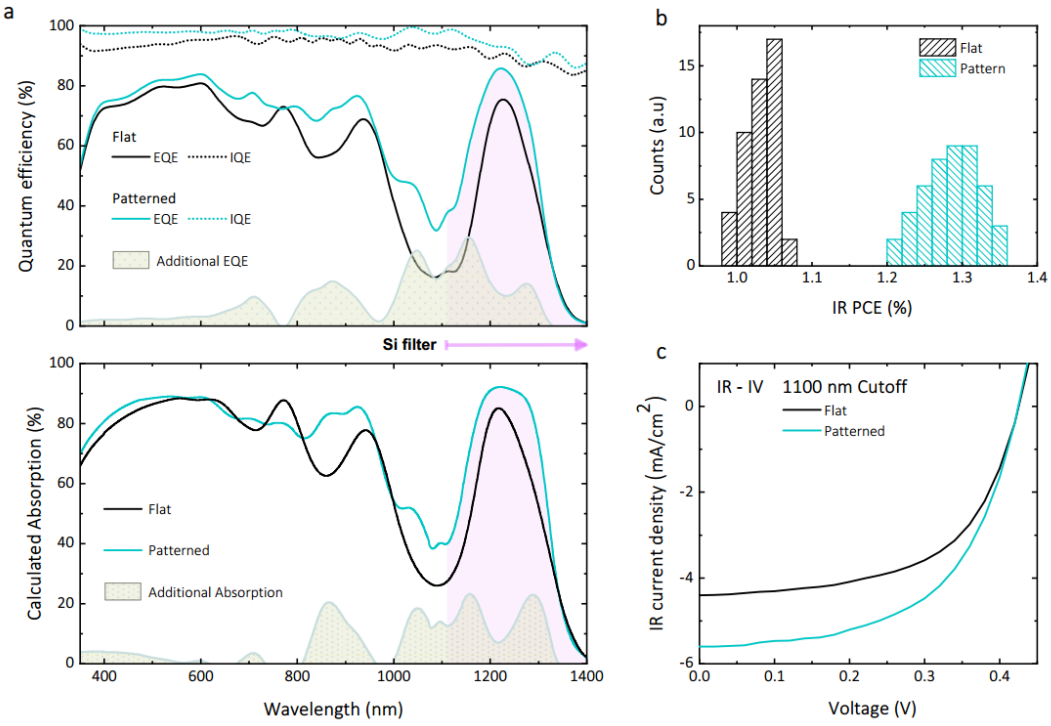

Figure 8. *(**a**) Experimental EQE and IQE (dots) (up) and calculated absorption (down) spectrum of IR CQD device with (blue) and without (black) imprinting. The grey area depicts the additional EQE/absorption enhanced with the photonic electrode. (**b**) Statistical histogram of PCE of IR CQD devices with (blue) and without (black) imprinting. (**c**) Representative J-V curves of IR CQD devices with (turquoise) and without (black) imprinting. The J-V was measured after the 1100nm-cutoff filter (purple region in a).*

We then measured the *J–V* characteristics for both flat and patterned IR CQD devices under AM 1.5 illumination with a silicon cut-off filter (allowing illumination for λ > 1100 nm) (**Figures 8b-c**). The PCE of the devices with the photonic electrode (1.27%) was statistically higher than that of flat devices (1.03%). In the IR region, the flat device generated 4.4 mA/cm^2 and the patterned device 5.6 mA/cm^2, achieving a J_{sc} 27% enhancement with comparable V_{oc} and *FF* (See **Table 1**). [191,211]

1220nm CQD	V_{oc} (V)	J_{sc} (mA/cm^2)	FF	IR PCE (%)[a)]	+ c-Si PCE (%)[b)]
Flat	0.43 ± 0.00[c)] (0.43)[d)]	4.30 ± 0.08 (4.4)	0.56 ± 0.10 (0.57)	5.25 ± 0.11 (5.51)	1.03 ± 0.02 (1.08)
Patterned	0.43 ± 0.00 (0.43)	5.40 ± 0.14 (5.6)	0.55 ± 0.15 (0.56)	6.50 ± 0.15 (6.83)	1.27 ± 0.03 (1.34)

Table 1. *IR CQD solar cells parameters characterized under AM 1.5G with 1100nm-cutoff filter. (**a**) Calculated IR PCE under the filtered AM 1.5 solar spectrum (19.1 mW/cm^2, cutoff <1100 nm), (**b**) Added IR PCE to c-Si solar cells under the AM 1.5 solar irradiation, (**c**) Average solar cells parameters and standard deviations, (**d**) Brackets depict the best values at each parameter*

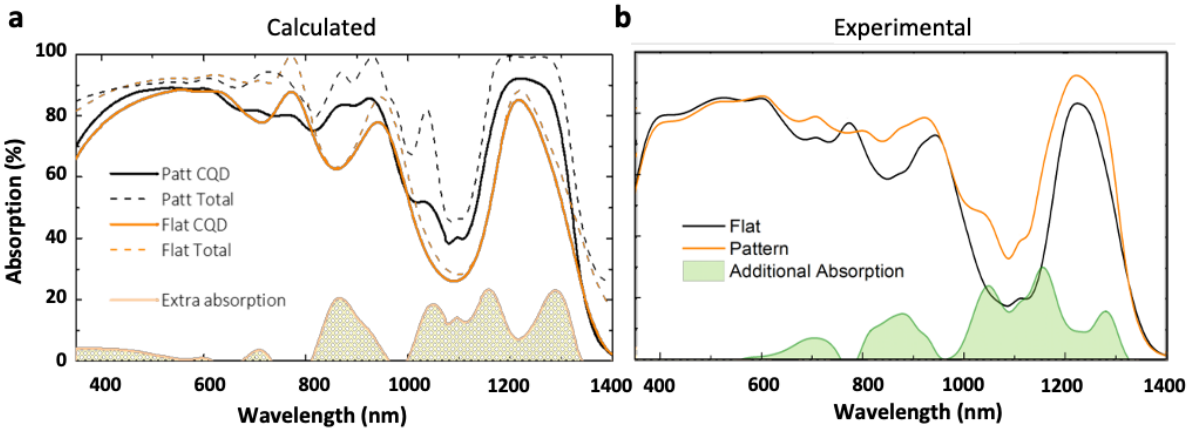

Figure 9*. (**a**) Calculated CQD (solid) and total (dot) absorption of flat (orange) and patterned (black) device. Note that the total absorption comprises that of ITO, ZnO, HTL and electrode. Yellow area depicts the absorption difference between patterned and flat CQD device structure. (**b**) Experimental absorption of IR CQD solar cells with (Orange) and without (black) pattern. Green area exhibits the absorption difference between pattern and flat device.*

To sum up, we designed and fabricated CQD solar cells with photonic back electrodes that improve absorption within the CQD solid especially in IR range. To fabricate the photonic structure within the HTL, we replaced the conventional rigid EDT-treated CQD HTL with a soft, patternable conjugated copolymer with high hole mobility and a band alignment conducive to the egress of holes from the CQD active layer into the contact. Soft NIL added to the HTL fabrication procedure enhanced EQE and PCE in the spectral regime beyond silicon's absorption. Therefore, we succeeded in integrating seamlessly a light trapping structure in solution-processed IR optoelectronics.

5.3. Extending the responsive regime of organic photodetectors through simple nanostructuring

5.3.1. Introduction to organic photodetectors

Nowadays, near infrared photodetectors are a ubiquitous technology, used on a daily basis in applications such as automatic sliding doors, NIR cameras, remote controls, telecommunications, spectrophotometers, and medical diagnosis.[212,213] Current NIR photodetector technologies rely on combining silicon or, to a lesser extent, III-V (InGaAs) with color filters or gratings.[214,215] This approach has proven to be functional and reliable. However, such wafer based photodetectors with extra filtering components fail to satisfy the new demands for wearable, cheap and flexible devices. In this direction, organic photodetectors (OPDs) are emerging as an appealing alternative, thanks to their flexibility, low embedded energy processing and high compatibility with available and easily scalable techniques such as roll-to-roll processing.[216–219] Ease and low cost manufacture is not their sole advantage, since the composing organic polymers and/or small organic molecules can be chemically tuned to provide a variety of absorption ranges.[220–222] While this approach works well in the visible range, extending the photoresponse towards the NIR range has been challenging. Lower bandgap polymers and small molecules with responses that go deeper into the infrared are being synthesized[223,224]. Nevertheless, these new materials are complex and expensive, both in time and energy, reducing their potential to be used in real devices.[223] Moreover, new molecules have to be developed for each targeted wavelength range, strongly increasing the required synthetic efforts.

Alternatively, some effort has been devoted to extend and increase the absorption in the NIR region of inexpensive and readily available materials using new inventive designs.[225,226] One approach that rendered promising results to obtain narrow and high external quantum efficiencies in the NIR is the filtering effect in thick polymer layers, also known as charge collection narrowing.[227] However, since this approach relies on the intrinsic absorption of the materials, it still requires relatively low bandgap materials to reach into the NIR region.

A recently proposed elegant alternative is to take advantage of the direct intermolecular Charge Transfer State (CTS) absorption, extending the photoresponse into the NIR region without the need of low bandgap materials.[228–231] The CTS is the result of the interaction between the HOMO of the donor and the lowest unoccupied molecular orbital (LUMO) of the

acceptor. This state appears only at the donor-acceptor interface, where the different electronic orbitals come together forming a new, intermediate state. The latter usually has a significantly lower transition energy than the corresponding constituents in a type II heterojunction, such as typical donor/acceptor blends. In other words, the HOMO energy level of the donor is higher than that of the acceptor and the LUMO energy level of the acceptor is lower than that of the donor (staggered gap). Since the CTS has a lower transition energy, the blend can potentially absorb light with photon energies below the bandgaps of each of its separate components. The CTS absorption strength depends on the intermixing of the molecules and, unfortunately, is around two orders of magnitude lower than singlet absorption due to the fact that it is an intermolecular state.[224] The intrinsic low oscillator strength of the CTS often requires the use of very thick active layers at high reverse voltages in order to obtain a significant photoresponse.[232] In a traditional device configuration, in order to enhance the absorption of the CTS, the thickness of the active layer must be enormously increased (tenths of microns); implying the usage of hundreds of Volts applied bias to extract charges efficiently.[232] In order to avoid such high voltages and thick layers, light trapping schemes offer an interesting alternative to greatly enhance the CTS absorption. Recently, the use of metal cavities has led to an impressive photoresponse in OPDs beyond the bandgaps of the composing materials.[35,233–235] When using optical micro-cavities, the detection wavelength can be tuned by controlling the cavity dimensions accurately, i.e. the active layer thickness. While these devices exhibit a very good performance, the resonant frequency critically depends on film thickness. Thus, they may not be compatible with techniques such as roll-to-roll, in which thickness usually fluctuates within a certain tolerance. In the other hand, major accomplishments have already been achieved in photovoltaics by structuring the device with photonic crystals.[236–239] In the case of 2D photonic crystals, its periodic structure diffracts incident light and enhances the optical path within the active layer, rendering higher efficiencies.

In this section we describe a method to enhance the CTS absorption of organic photodetector devices effect via a nanostructured active layer in the shape of a photonic crystal.[240] First, we choose the materials used and design the device with the photonic structure. To fulfill real application demands, we employ low cost blend materials and use inexpensive and scalable techniques. Later, we fabricate it disturbing the minimum as possible the original fabrication scheme. Finally, we characterize it optically and electronically. This work was done in collaboration with Prof. Mariano Campoy and Martí Gibert from the Nanopto group at the ICMAB.

5.3.2. The Device: NIR organic photodetector

5.3.2.1. Composition

The organic photodetectors fabricated and studied in this work had the usual layered structure, presented in **Figure 10b** and similar to the one used in the last section for CQD solar cells**.** This comprised a transparent electrode of ITO followed by an ETL of ZnO, the organic active layer (AL), a HTL of MoO3 and the silver back contact. In our organic photodetectors, the AL were P3HT:$PC_{60}BM$ and PBTTT:$PC_{70}BM$ bulk heterojunction (BHJ) blends for four main reasons (**Figure 10a**): (1) these blends are based on inexpensive materials, which makes them appealing for large scale applications; (2) they exhibit a significant CTS absorption that extends deep into the NIR region, so we can extend the response of the photodetector beyond the band gap; (3) they have high carrier mobilities that allow to deposit thick active layers, which is essential to take maximum profit of the CTS low absorption coefficient;[224] and (4) they have a relatively low glass transition temperature which will allow us to perform the nanoimprinting.

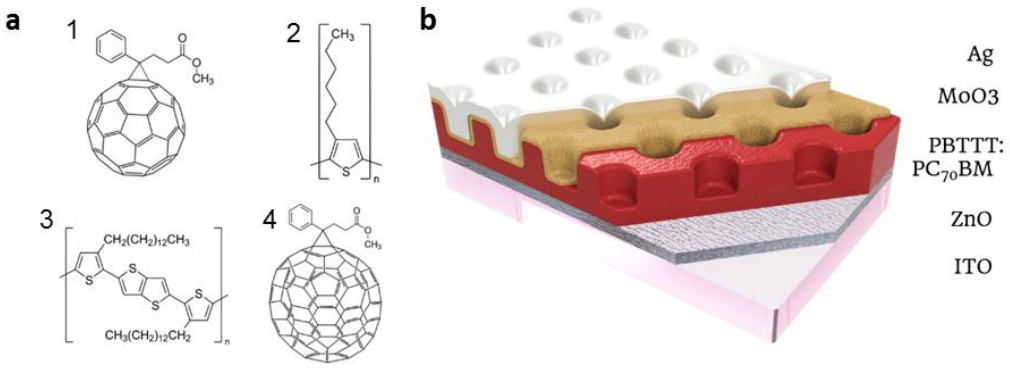

Figure 10. *(**a**) 1.Phenyl-C61-butyric acid methyl ester ($PC_{60}BM$) (>99.5%), 2.Poly(3-hexylthiophene-2,5-diyl) (P3HT), 3.[6,6]- Phenyl C71 butyric acid methyl ester ($PC_{70}BM$) and 4.Poly[2,5-bis(3-tetradecylthiophen-2-yl)thieno[3,2-b]thiophene] (PBTTT-C14). (**b**) Diagram the organic photodetector structure and each layer's material.*

5.3.2.2. The light trapping scheme

In order to have a significant response on the NIR region, the nanostructuration of the device was of key relevance to grant it with light trapping properties at wavelengths below the band gap of the BHJ materials. The nanostructure consisted on an array of cylindrical pillars forming a 2D photonic crystal at the back electrode. This protruded into the AL, acting as a diffraction grating that couples the incident light to the guided modes of the active layer (**Figure 10b**). The

array lattice parameters (L) were chosen to be of 400, 500 and 600 nm to place their Rayleigh-Wood's anomalies inside the range of absorption of the charge transfer state (λ=700-1100 nm, **Figure 11**). As explained in the introduction of the **chapter 5**, the diffraction caused by the lattice periodicity grants the incoming light with enough parallel momentum to access to guided modes of the active layer. It must be taken into account that these guided modes are inherently leaky because of the same grating, which enables the in-coupling as well as the out-coupling.

One critical parameter to take into account in the design of the photonic nanostructure is the depth of the array of holes on the active layer. As discussed in **chapter 5.1**, deeper holes would lead to higher pillars that would exhibit stronger diffraction and thus provide more efficient light trapping. Nevertheless, if the holes present on the active layer are too deep, the nanometric MoO_3 hole transport layer would not cover the active layer homogeneously, leading to the creation of pinholes and disrupting the electrical properties of the device. For this reason, we limited the height of the features of our architecture down to 60 nm, avoiding pinhole generation with a complete coverage of the active layer by each of the subsequent layers.

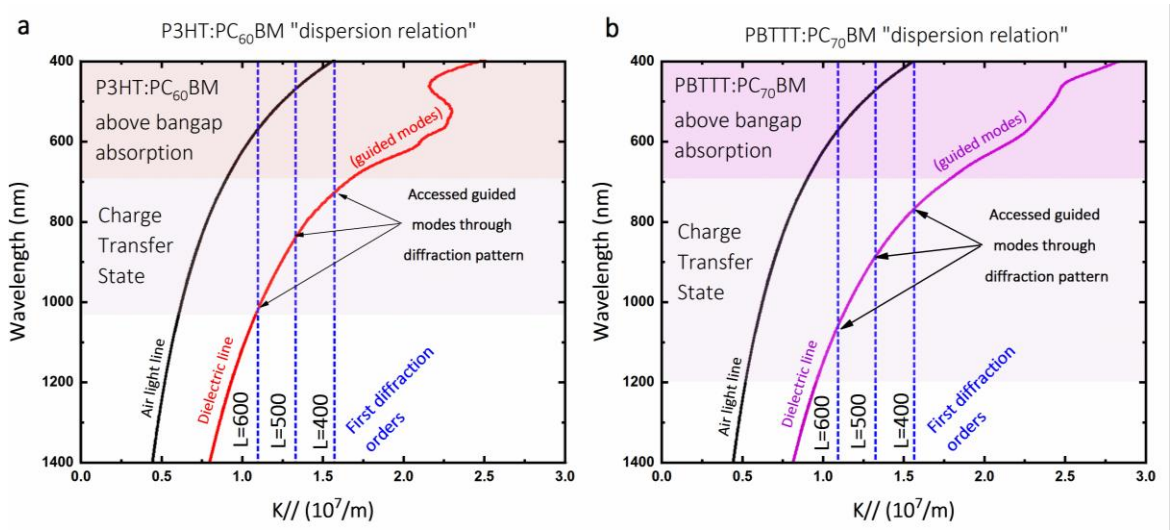

Figure 11. *Dispersion relation of the wavelength vs parallel wavevector of the incident light for (**a**) P3HT:PC60BM and (**b**) PBTTT:PC70BM blends. The first diffraction orders of the photonic crystal arrays with lattice parameters of 400 ,500 and 600 nm (blue dashed lines) grants to the incident light the necessary momentum to couple to the guided modes within the semiconductor material in the Charge Transfer State range of absorption (**a**) red and **b**) purple lines).*

The second cornerstone of this work was being able to deposit a thick active layer to take maximum profit of the low absorption coefficient of the CTS[224] while keeping electrical losses to a minimum. A compromise between the optical and electrical properties of the device must be reached when designing the optimum device thickness to ensure the best performance as an efficient NIR photodetector. While thin active layers (of the order of 100 nm) exhibit high EQEs in the visible but negligible CTS absorption in the NIR, thicker active layers deteriorate the system's electrical response in the visible due to filtering effects, but maximize the CTS absorption response in the NIR. Since the majority of visible photons are absorbed within the first nanometers due to the intrinsic high absorption coefficient of the blend, the charge generation distribution is non-uniform and the travel path for half of the charges is significantly longer, leading to high recombination probabilities and therefore decreasing the overall electrical response in the visible range. On the other hand, charges generated from CTS absorption at NIR wavelengths are homogeneously distributed along the entire active layer due to its low absorption coefficient, rendering in a much more effective electrical response.[227] The thickness of the active layer could be increased to achieve a higher CTS response up to the point where the AL would be so thick that the whole device starts having electrical losses due to the limited conductivity of the blend (on the order of several microns). For our purposes, the optimum active layer thicknesses were 700 nm for P3HT:$PC_{60}BM$ and 1600 nm for PBTTT:$PC_{70}BM$.

Another relevant aspect is the thickness of the hole transport layer, in this case MoO_3, as it affects both electrical and optical properties. As the layer is deposited on top of the nanostructured active layer, extremely thin layers (less than 5 nm) would lead to pinhole formation as discussed above, even with shallow features. Also, thicker layers (over 50 nm) must be avoided since that diminishes the light trapping capabilities of the designed structure. This is mainly because the HTL deposition leads to a smoothing effect of the pattern left for the next layer, the silver contact back reflector, whose structure plays a major role to the light trapping scheme. Therefore, the HTL layer was set to 10 nm, enough to have a uniform coverage while maintaining the optical properties of the device.

Finally, the thickness of the back reflector contact was set to be 200 nm to avoid undesired light transmission and ensure good uniform coverage of the whole structure.

5.3.3. Fabrication of the NIR organic photodetector

To fabricate the device, we deposited a 100 nm ZnO ETL over the ITO covered glass substrates by blade coating. After annealing at 1h at 100°C, we proceeded with the deposition of the thick active layer, again by blade coating. After the deposited active layer was dry, we nanostructured it with the hot embossing soft tNIL technique detailed in **chapter 2.2.2.1** (**Figure 12a**).

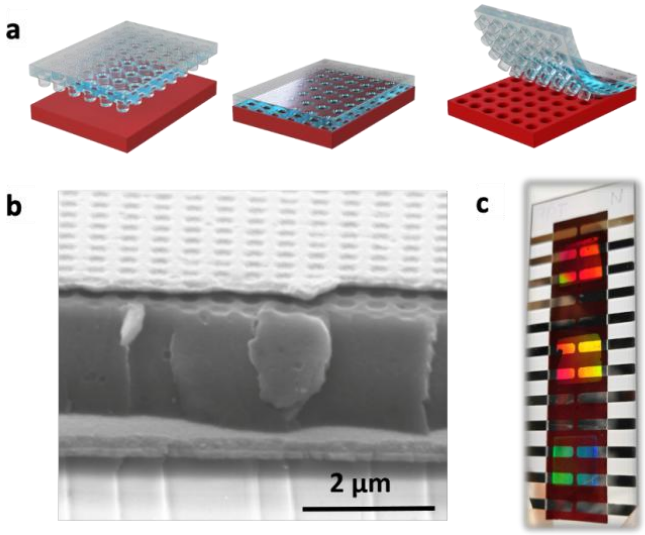

Figure 12. *(**a**) Soft nanoimprinting lithography process steps. (**b**) SEM image of one of the finished nanostructured photodetectors. (**c**) Picture of the finished device showing different iridescence for each lattice parameter nanostructure; L= 600, 500 and 400 nm from top to bottom.*

This nanostructuring technique has demonstrated reliability to produce extended areas of nanostructures and avoids using aggressive nanostructuring processes, as detailed in **chapter 2.2**. Pressing at 4 bars a nanostructured hPDMS stamp mold onto the active layer at 135°C, above the glass transition of the polymer blend, was enough to nanoimprint the negative photonic crystal shape on the device. Once the active layer was nanoimprinted with the 60nm deep features, 10 nm of MoO_3 and 200nm of Ag were sequentially thermally evaporated (**Figure 12b, c**). When the back electrode was deposited onto the nanostructured active layer, it took its shape resulting in a nanostructured back electrode, which acted both as reflecting and diffracting element.

Finally, the samples were annealed to increase the AL crystallinity. Annealing the sample at 135°C during 20 minutes has a significant effect on its performance. Un-annealed samples and over annealed samples showed responses 10-20 times lower than annealed samples.

5.3.4. Optical and electrical characterization of the nanostructured device

As our goal was to improve the efficiency of the CTS absorption in the NIR range, we focused the characterization in that spectral range, from 700 to 1100 nm. We began with the optical characterization to ensure the photonic impact of the nanostructure on the device. Later on, we corroborated the photoelectrical characteristics of the device with EQE and light beam induced photocurrent (LBIC) measurements to ensure that the optical modification produced by the light trapping scheme renders in a performance enhancement. Finally, we checked the electrical characteristics of the device to confirm that our pattern did not affect the electrical performance of the device.

The extinction FTIR measurements revealed that the patterned devices always had higher extinctions in the region of interest that the flat devices. In **Figure 13** it can be seen how the devices with L= 600 nm pattern showed the highest extinctions in the 950 to 1100 nm regime (red line), in agreement with the analytical calculus done in the nanostructure design section (**Figure 11**). Also in agreement with the previous calculus, the devices with L= 500 nm exhibited a strong extinction peak around 910 nm (**Figure 13** blue line). On the other hand, the L= 400 nm devices did not show great extinction enhancements but a slight one from 750nm to almost 900 nm (**Figure 13** green line). This was probably due to the proximity and overlapping of the main excitonic peak of the active material and the predicted diffraction mode for this lattice parameter, which prevents it to be clearly resolved, and can be seen just as a shoulder or an extension of it.

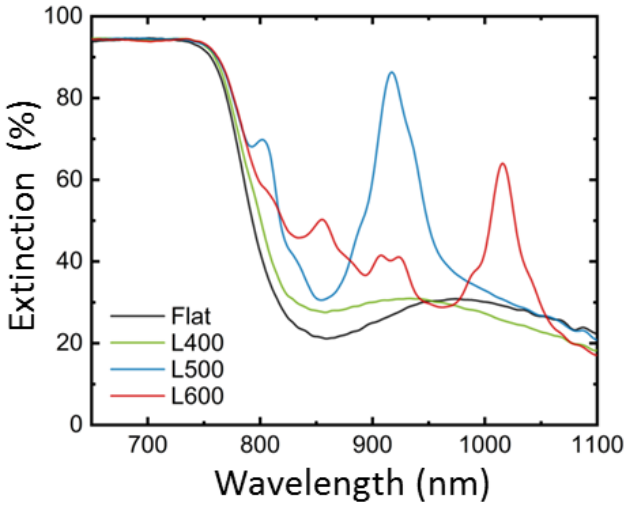

Figure 13. *PBTTT:$PC_{70}BM$ photodetectors extinction measurements for non-structured (flat, black) and nanostructured with L= 400 (green), 500 (blue) and 600 nm (red).*

To characterize the performance of the fabricated organic photodetectors we performed EQE measurements combined with LBIC measurements as well as dark current and pulsed light response measurements. The EQE measurements provided us with spectral dependence of the efficiency that can be directly correlated with the calculated absorption of the designed architectures and the LBIC maps ensured the macroscopic homogeneity in the performance of the devices.

All the nanostructured devices fabricated with the optimized parameters discussed revealed a better EQE performance in the near infrared region of interest compared to the reference flat samples (**Figure 14**), for both active layer compositions. This enhancement is in the form of very narrow peaks at specific wavelengths that depend on the lattice parameter of the photonic crystal and the refractive index of the active layer. Larger lattice parameters induce a redshift in the position of the peaks. Also, as predicted in **Figure 11**, PBTTT: $PC_{70}BM$, with slightly higher refractive index than P3HT: $PC_{60}BM$, presented the enhancement peaks more into the infrared (**Figure14b** vs **14a**). For both AL compositions, the devices with the smallest lattice parameter of 400 nm presented a peak at the tail of the singlet absorption (**Figure 14** blue lines), located at 750 nm and 800 nm for P3HT: $PC_{60}BM$ and PBTTT: $PC_{70}BM$ respectively. Compared with the flat reference of the same thickness, this represented an enhancement of 60 and 70% for each one. In the samples with L= 500 nm several peaks achieved EQE efficiencies deep into the NIR range over 2% for both PBTTT:$PC_{70}BM$ and P3HT:$PC_{60}BM$ (**Figure 14a,b** green lines). P3HT: $PC_{60}BM$ samples exhibited peaks at wavelengths around 800-850 nm

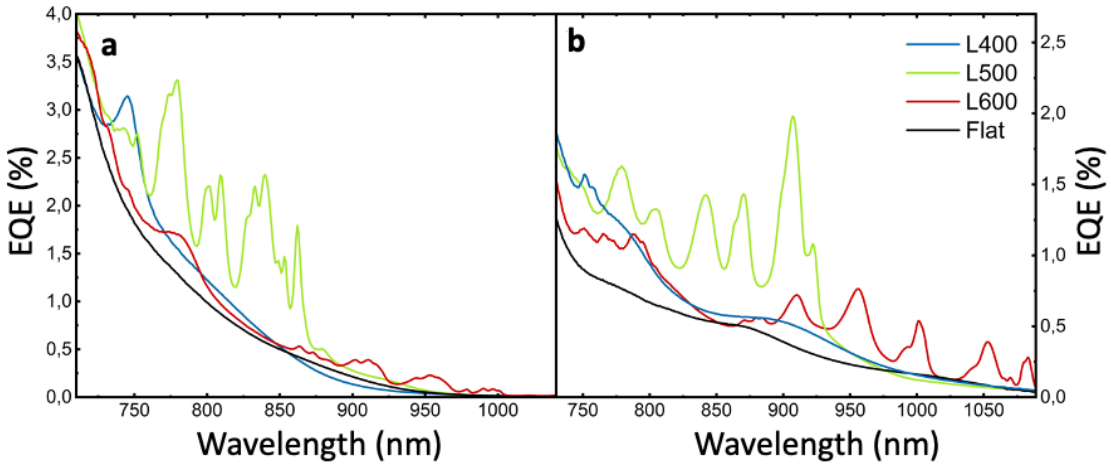

Figure 14. *External quantum efficiency measurements for non-structured (flat) and differently nanostructured photodetectors (L= 400, 500 and 600 nm) with an active layer of (**a**) P3HT:$PC_{60}BM$ and (**b**) PBTTT:$PC_{70}BM$.*

with a 4-fold enhancement factor on its maximum at 837 nm with respect to the planar reference, achieving a maximum EQE value of 2.4%. In the case of PBTTT:$PC_{70}BM$, the peaks fell deeper into the NIR (850-920 nm), where a 5-fold increase on conversion efficiency could be seen at 907 nm, with EQE maximum values of 2% (**Figure 14**).

Finally, in the L= 600 nm devices, EQE enhancement peaks with maximum values around 0.5 % were present significantly further into the NIR reaching wavelengths of 1000 nm and almost 1100 nm for PBTTT: $PC_{70}BM$ and P3HT: $PC_{60}BM$, respectively (**Figure 14a, b red lines**). The lower values in the EQE performance, compared to the other lattice configurations, were due to the decrease of the CTS absorption coefficient at higher wavelengths, being more pronounced in P3HT:$PC_{60}BM$ than in PBTTT:$PC_{70}BM$.[35] In P3HT:$PC_{60}BM$ based devices, the EQE peaks were located around 900-1050 nm, with a maximum at 1000 nm where a 5.8-fold enhancement was reached. For PBTTT:$PC_{70}BM$ devices, the peaks were a bit deeper into the NIR, around 950-1100 where the maximum enhancement was located at 1083 nm, being 6 times better than its flat counterpart.

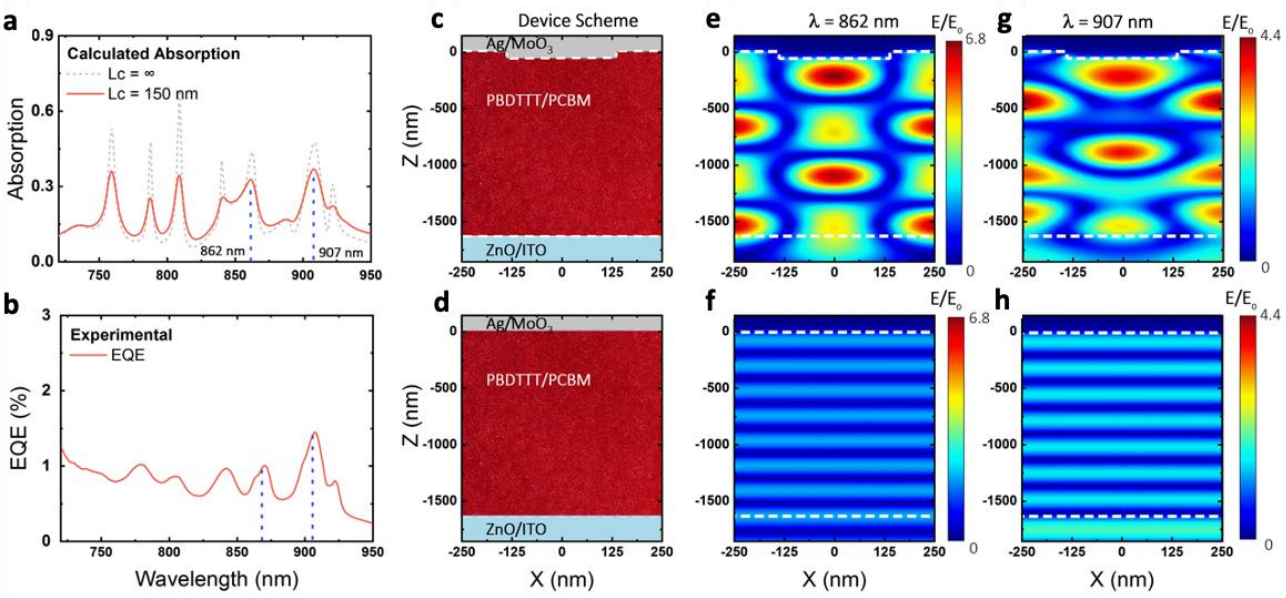

Figure 15. *(**a**) Calculated absorption of the fabricated devices with fully coherent light (grey dashed) and 150 micron coherent light (purple). (**b**) External quantum efficiency measurements for a PBTTT:$PC_{70}BM$ nanostructured photodetector with a lattice parameter of L = 500 nm. Sample scheme for nanostructured (**c**) and flat (**d**) devices and calculated electric fields at wavelengths 862 (**e** and **f**), and 907 nm (**g** and **h**), for nanostructured and flat devices, respectively.*

Since the lattice parameter of L= 500 nm provided the best EQE enhancement values, thanks to a high CTS absorption with little influence of the singlet absorption tail, this was the system that was studied in more detail (**Figure 15**). A calculated absorption spectrum (**Figure 15a**) of the L= 500 nm PBTTT: $PC_{70}BM$ device with good agreement with the external quantum efficiency spectrum (**Figure 15b**) allowed us to validate the effect of the photonic electrode through the examination of the electric fields at the peaks of maximum response. The electric field profile examination at the peaks of 862 nm and 907 nm in both the nanostructured (**Figure 15c**) and the flat (**Figure 15d**) devices shows how the fields in the planar device present a standard plane wave distribution (**Figure 15e, g**) while the patterned devices show a diffraction pattern inside the active layer (**Figure 15f, h**) with field enhancements over 6 times the incident power. The stronger field enhancement in the active layer generated by the diffraction modes of the array is what provided a higher absorption of the charge transfer state in the selected wavelengths.

In addition to unbiased EQE, we also evaluated the photodetectors under reverse V bias to evaluate the charge generation capacity of our nanostructured devices compared with the flat reference samples. For the L= 500 nm PBTTT:$PC_{70}BM$ device, an increase from 2% to 7.5% EQE performance at 907 nm was measured while the reference device still layed below 2% under a 23 V reverse bias. Also nanoimprinted and flat devices exhibited similar dark currents, indicating that we successfully avoided pinhole formation and had a good conformal layer deposition. Obtained values were around 10 $nA \cdot cm^{-2}$ at 1 V and 1 $\mu A \cdot cm^{-2}$ at 15 V. We considered these dark current values low considering the large area of photodetection (8 mm^2). Also, the response of the nanostructured photodetectors was highly linear exhibiting r^2 values up to 0.999 over more than 50 dB.

As the spectral EQE response depends on the lattice parameter of the pattern, one step further in this project was to incorporate a gradient of the different geometries in the same device to visualize spatially how the spectral response varies with the different structures. In this way we also certified the homogeneity of the structures and its performance through all the device. This could be done with an LBIC mapping. The proceeding is based on the measurement of the local short circuit current in the cell by locally irradiating with laser light. A LBIC mapping of a PBTTT:$PC_{70}BM$ device with the three different lattice parameters at three different wavelength excitations shows how we tuned the absorption of the CTS with the various geometries (**Figure 16**). When excited with a wavelength of 710 nm, all three different patterns offered similar responses because all of them have diffraction orders at these wavelengths, where the singlet tail absorption is still present (**Figure 16a**). Although no

significant difference was observed between the three patterns, they all outperformed the flat non-patterned regions (which is the mostly deep blue region found in between the patterns in **Figure 16**), revealing the importance of the nanostructuration. When the excitation wavelength was set to 941 nm, in a spectral region where there is no contribution of the singlet tail absorption, only CTS absorption, the difference between the three fabricated structures became more relevant (**Figure 16b**). At this wavelength, the pattern of L = 400nm did not present any light diffraction, so its response was equal to the flat zones. Meanwhile, regions with L = 600 nm and 500 nm still showed good responses, being this last the one the optimum for this wavelength, as studied before with the spectral EQE. Finally, at 1031 nm, only the region patterned with the 600 nm lattice parameter offered good enhancement with respect to the planar reference (**Figure 16c**). With this study it is demonstrated how we can tune the EQE's spectral response with a rational structure design and how it could be all integrated in one device to have a gradient dependent spectral response in one same device.

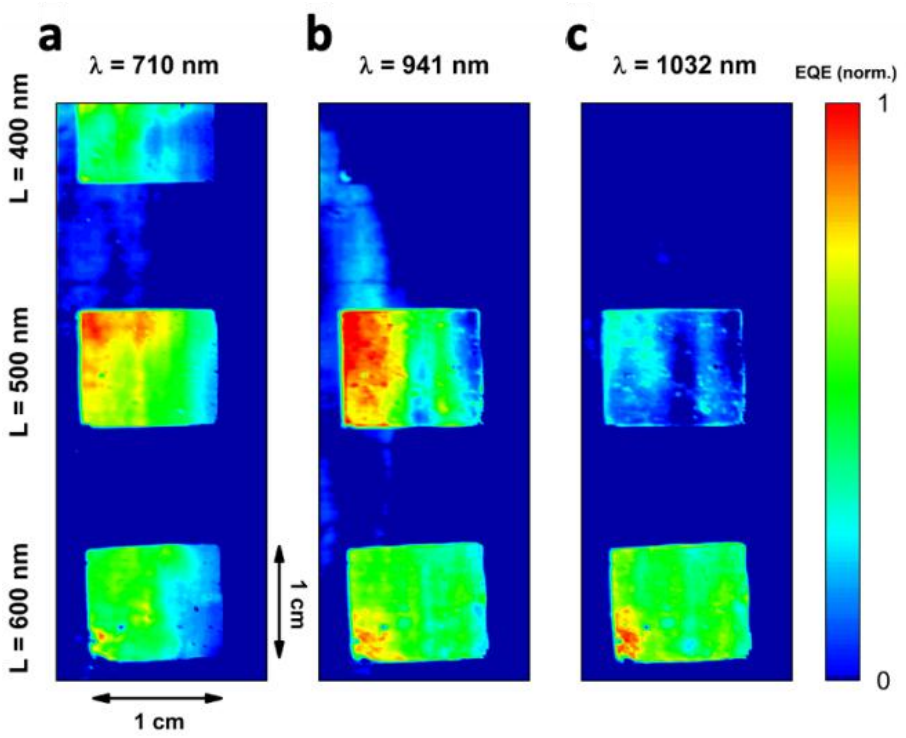

Figure 16. *Light beam induced photocurrent (LBIC) maps of a large area continuous back electrode photodetector, at 3 different excitation wavelengths: (**a**) 710 nm, (**b**) 941 nm and (**c**) 1032 nm, with 3 different nanostructured zones. From top to bottom: L =400, 500 and 600 nm.*

To sum up, in this section, we presented a new organic BHJ based photodetector architecture that is capable of detecting light at wavelengths significantly below the bandgap of its components. This was achieved by boosting the absorption of the long CTS absorption tail present in P3HT:$PC_{61}BM$ and PBTTT:$PC_{71}BM$ blends. Their CTS absorption was enhanced by incorporating a photonic architecture within the device via the nanostructuration of the active layer. Both the active layer and the patterning were carried out using roll-to-roll compatible and highly scalable techniques. Furthermore, the used polymers and small molecules are inexpensive and easy to produce, making them ideal for large scale production. The performance of the photodetectors was tested through several techniques, showing that our nanostructured OPDs are significantly superior than flat OPDs in at different wavelengths within a wide region of the NIR thanks to our strategy to enhance the CTS absorption

5.4. Enhanced Directional Light Extraction from Patterned Rare Earth Phosphor Films

5.4.1. Introduction to nanophosphors

Phosphors are the materials most commonly used in solid-state lighting.[241] They usually consist of inorganic matrices doped with rare-earth (RE) cations. RE phosphors offer high thermal and chemical stability and are used as color-converting materials along with blue or UV light-emitting diodes (LEDs) to obtain emissions that cover different ranges of the visible spectrum. This approach has allowed the development of artificial illumination, featuring lower cost and more efficient devices, and rendering better quality lighting for the last two decades. Apart from illumination, the field of use of LED-based devices is wide, from sensors to wireless communication, passing through human-centric lighting or horticulture industry.[242]

On this basis, directional and spectral control of the out-coupled light intensity are features of interest for many applications. Light out-coupling is a key point for every light-emitting system since light is generally generated in a medium with high refractive index, and thus a significant fraction of the emitted light, regardless of the internal efficiency of the emitter, will remain trapped in the emitting layer. This drastically affects the external quantum efficiency of the devices. Several out-coupling strategies have been developed in the last years to alleviate this drawback. Such control could in principle be achieved in solid state lighting by means of an adequate photonic design of the color converting layer. Optimized devices typically feature microlenses,[243–245] scattering layers,[246,247] surface roughening,[248] dielectric or even metallic periodic arrays[249–251] to aid the emitted light escape the bulk of the device. However, conventional phosphor coatings in the current LED lamps are usually thick, since RE cations present low absorption cross-sections, and exhibit large crystal size, giving rise to multiple scattering processes hence low transparency. As a result, directionality is nowadays attained by introducing classical optical elements, such as lenses or mirrors.

In this context, several groups have addressed the development of photon management strategies compatible with phosphor films that can take advantage of the control over the optical absorption and emission they offer, and, in particular, aiming at improving the out-coupling efficiency of color-converting layers. Specifically, different photonic structures have been proposed to improve the directional and spectral control over the phosphor luminescence.[249,252–258] Some of the preferred approaches consist in covering the phosphor

layer with a two-dimensional (2D) array of dielectric scatterers or nanoantennas, similar to those introduced in **chapter 1.3.2**. These enhance the coupling of emitted light to free-space, mostly applied to enhance the external efficiency in both organic[244,245] and inorganic[259–261] LEDs. From a technical perspective, the combination of such photonic architectures with phosphor-based devices is far from compatible with most traditional lithographies, as most of them include etching steps that would decrease the emission efficiency of the phosphor. Soft NIL, however, as introduced in **chapter 2.2**, offers a low-cost route in the wet-processing of 2D photonic structures fully compatible with high-throughput manufacturing.[2,3] In comparison with traditional photolithography, soft NIL allows surface patterning large areas employing a variety of materials and methods, with a very high reproducibility and without the limitation posed by optical diffraction.[87,236]

In this section we describe a straight forward and non-invasive procedure for attaining textured phosphor films displaying enhanced out-coupling properties. We use transparent films made of nanophosphors as starting materials, which allow a precise and efficient direct RWG patterning by soft NIL. Reliefs are designed to selectively maximize out-coupling of selected emitted wavelengths. Once these are transferred to the film, we study the resultant optical properties and the effect on the resulting photoluminescence. We start by studying the in-coupling of the light to the nanophosphor film, and later we study the following out-coupling of the emitted light. With the reciprocity principle, we analyze the effect of the imprinted diffraction grating on both the directionality and the enhancement of the emission. A full theoretical description of the field distribution inside de material by finite-difference time-domain method is also done to further describe the origin of the reported emission out-coupling enhancement. This work was done in collaboration with Prof. Hernán Míguez and Elena Cabello-Olmo of the Multifunctional optical materials group of the Institute of Materials Science of Seville (ICMS).

5.4.2. The device: Emitting nanophosphor films

5.4.2.1. Composition

The emissive nanophosphors used in this work were nanoparticles composed of a host lattice of gadolinium vanadate ($GdVO_4$) doped with rare earth cations of Eu^{3+}. The nanoparticles employed were nearly equiaxial in shape, with a mean lateral size of 35 nm, corroborated by transmission electron microscopies (TEM) (**Figure 17a**). The size of the nanophosphor

nanoparticles was essential as it is what defines the resolution of the final structure (**Figure 19e, g**). Bigger nanoparticles would lead to poorly defined structures and subsequently poor optical properties. It is important the fact that these nanoparticles, with the aid of an organic binder, can be easily dispersed in a solvent, in this case ethanol. This enabled to implement the solvent assisted soft NIL procedure detailed in **chapter 2.2.2.2**. The PL emission spectra of a thin film made of such nanophosphors exhibited the characteristic transition lines of Eu^{3+} corresponding to the de-excitation from the $^5D_0$ level to $^7F_1$,$^7F_2$, $^7F_3$ and $^7F_4$ when excited under UV light (**Figure 17b**). The photoexcitation was monitored at the most intense emission peak of Eu^{3+}, i.e. λ=619 nm, and featured a broadband in the UV (**Figure 17b**, grey line). The excitation of the emitting RE cation (Eu^{3+}) takes place via a transfer mechanism through the absorption band of the host lattice of $GdVO_4$. By this mechanism, it is possible to overcome the low absorption cross sections that the RE cations feature for 4f—>4f transitions. The $GdVO_4$ crystalline matrix is able to absorb most of the incoming light and transfer it to the RE cation, leading to much more efficient and brighter emissions.

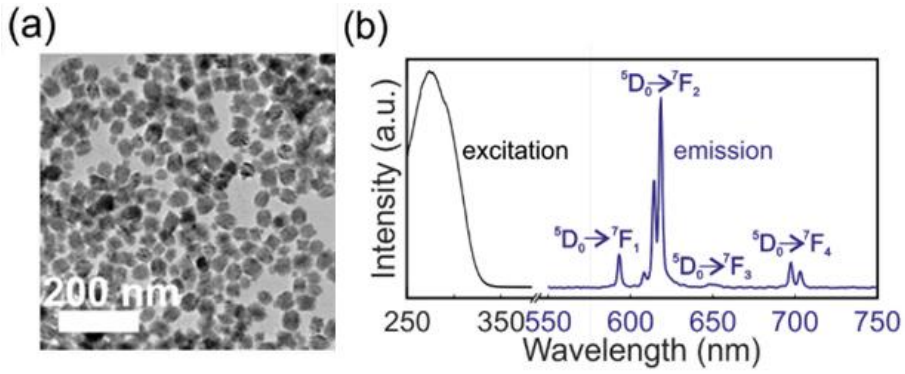

***Figure 17**. (**a**) TEM of the starting nanoparticles of GdVO4:Eu3+ for the nanophosphor paste. (**b**) Excitation (grey) and emission (blue) spectra of the synthetized nanoparticles.*

5.4.2.2. The light out-coupling scheme

Differently to the two previous sections of this **chapter 5**, this work is not devoted to confine the light into the material but to help the radiation escape. Nevertheless, one feature of RWG is that the same way it enables light coupling into a waveguide film, it also provides an efficient way to out-couple the guided light to the exterior; there is a reciprocal behavior. As described in **chapter 1.3.3**, one key characteristic of diffracted modes is their angular dispersion. This implies that each wavelength of the out-coupled light through a diffraction grating will be emitted at one specific direction. This enables the use of gratings as means to control the directivity of the emission (**Figure 18**).

To enhance the directional emission of the nanophosphor films, the Rayleigh-Woods Anomalies (RAs) of the designed RWG matched the spectral range with highest emission peaks. We primarily targeted to enhance the emission of the spectral range with most of emission of the rare earth cation Eu^{+3} (around 600 nm) at normal direction, perpendicular to de surface ($\vec{k}_{out,||}$= 0). As detailed in the introduction of this **chapter 5**, these RAs satisfy the following equation for the conservation of the wavevector parallel to the plane of the array:

$$\vec{k}_{out,||} = \vec{k}_{in,||} \pm \vec{G}(\mathrm{m_x}, \mathrm{m_y}) \tag{8}$$

$$\vec{k}_{out,||} = \frac{2\pi}{\lambda} sin\theta \tag{9}$$

$$\vec{k}_{in,||} = \mathrm{n}\frac{2\pi}{\lambda} \tag{10}$$

$$\vec{G}_{(\mathrm{m_x},\mathrm{m_y})} = \mathrm{m_{xy}}\frac{2\pi}{L} \tag{11}$$

With $\vec{k}_{out,||}$ and $\vec{k}_{in,||}$ being the parallel component of the out-coupled and emitted light wavevectors respectively, and $\vec{G}$ the reciprocal lattice vector, where *L* is the lattice constant of the square array and the pair of integers $(\mathrm{m_x}, \mathrm{m_y})$ defines the diffraction order, $m_{xy} = \sqrt{m_x^2 + m_y^2}$, θ the emission angle and n the refractive index.

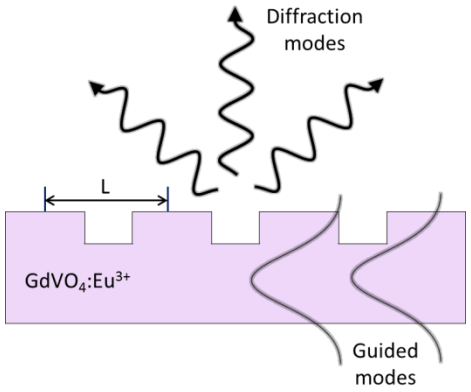

***Figure 18**. Schematic of the light out-coupling from guided modes through the diffraction modes of the nanophosphor resonant waveguide grating.*

Therefore, the preferred architecture was a square lattice array of holes with parameter L= 600 nm, whose first diffraction order into the air at 0° is at λ= 600 nm (<±1,0> and <0, ±1>). To ensure the correlation of the diffraction modes provided by the periodicity of the photonic

structure with the changes in the spontaneous emission of the nanophosphors, we also fabricated and studied samples with L= 400 and 500 nm. These lattice parameters also satisfy the relation in (**8**) for the targeted wavelengths but at non-normal directions. Therefore, these complementary structures will ensure that the obtained enhanced directional emission is due to the diffractive modes of the structured 2D photonic crystal.

5.4.3. Fabrication of the patterned nanophosphor films

To obtain the photonically enhanced nanophosphor substrates a three-step fabrication method was followed (**Figure 19**). Firstly, the $GdVO_4:Eu^{3+}$ nanophosphors were synthetized following a facile solvothermal method at the ICMS.[262] Secondly, in order to attain the surface relief patterns on the surface of the nanophosphor films, we prepared a viscous paste using the nanophosphors and ethyl cellulose as organic binder. The paste was later dispersed in ethanol 1:3 w/w (**Figure 19a**) and spun coated over flat, transparent, quartz substrates (**Figure 19b**). Immediately after the spin coating, prior to a complete drying of the film, the nanostructuration was done by using the solvent assisted method described in **chapter 2.2.2.2.**

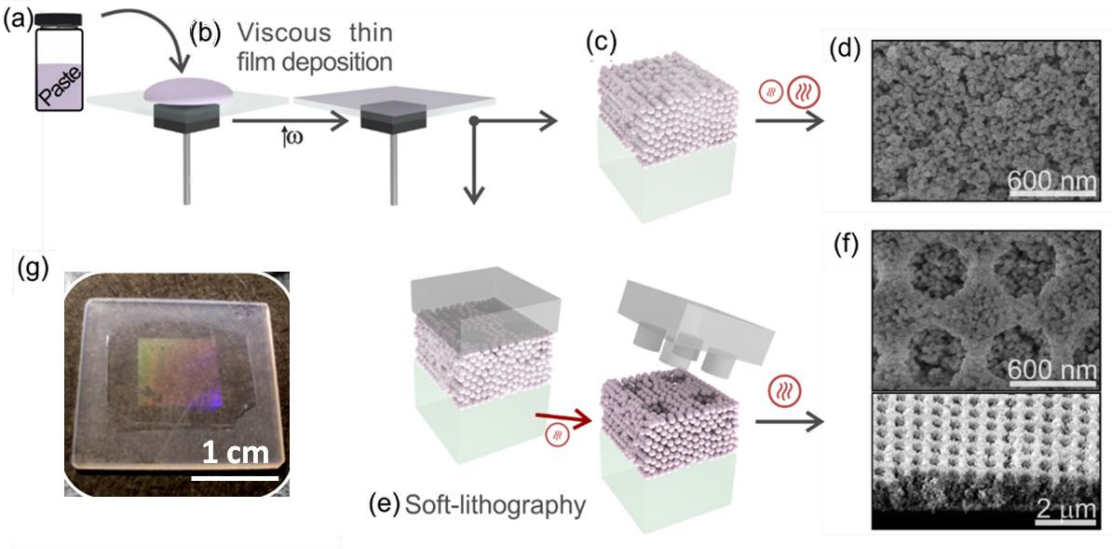

***Figure 19**. Schematic processing of patterned nanophosphor samples. (**a**) Ethanol dispersion of the nanophosphor paste. (**b**) Spin coating deposition of diluted paste over a quartz substrate. (**c**) and (**d**) Illustration and top view SEM image of the reference sample after heating. (**e**) Schematic illustration of the soft nanoimprinting lithography of the patterned sample with the PDMS mold. (**f**) Top and tilted view SEM images of the patterned samples with a lattice parameter L= 600 nm. (**g**) Picture taken from a sample. Notice that only the 1 cm x 1 cm central area of the sample is patterned.*

We pressed it with a pre-patterned hPDMS mold over a hot surface (80°C) until the solvent completely evaporated. This imprinted the mesoporous film with the negative nanostructure present in the hPDMS, in this case, a periodic array of holes (**Figure 19e, f, g**). Also flat unpatterned samples were prepared in the same conditions to be used as references (**Figure 19c, d**). Finally, a thermal annealing at 500°C was done and the structure of the samples was verified using scanning electron microscopy (**Figure 19d, f**). After this annealing, the planar films exhibited a photoluminescence quantum yield (PLQY) of 55%. The thermal treatment removes any organic impurities from the synthesis or the paste and determines the final emission properties (namely, PLQY and PL lifetime) of the phosphor layers, since it improves the crystallinity and eliminates quenching pathways caused by organic groups in the surface of the nanoparticles.

5.4.4. Optical characterization

In order to investigate the effect of the photonic structure in the spontaneous emission of the nanophosphors we made use of the reciprocity principle. We studied the behavior and angular features of the optical extinction of light impinging into the samples followed by one of the emitted light at the same wavelengths. In this way, applying the aforementioned reciprocity principle, we could establish a comparison between the results attained for the in-coupling of incoming waves of these wavelengths and the out-coupling efficiency of the waves when emitted from inside the samples.

The optical extinction as a function of the angle of incidence (θ_{in}) for the three samples fabricated, with L= 400, 500 and 600 nm, is shown in **Figure 20d-f**. The extinction is defined as 1-T_0, with T_0 being the zeroth-order transmission. For this purpose, the samples were mounted on a rotation stage and illuminated with a focused beam of unpolarized white light. The sample is rotated θ_{in} with respect to the surface normal along the *y=0* plane. At θ_{in} = 0°, for samples with a period of 400 nm, the maximum were found at λ = [412, 492] nm, while, for the larger pitches of 500 and 600 nm, the two maxima were detected at λ = [515, 595] nm and λ = [615, 700] nm, respectively. In a first approximation, we fitted the observed angular dispersion of the transmittance at θ_{in} = 0°, to that of estimated RAs for each lattice parameter. Following **eq.8** we identified the diffraction orders present in the experimental values (**Figure 20d-f**) as two sets of RAs for two different effective media (solid and dashed lines in **Figure 20g-i**). The high energy RAs (dashed lines) results correspond to the first diffraction orders (<±1,0> and <0, ±1>) into the air (n_{eff} =1.03). The lower energy RAs (solid lines) can be associated to <±1, ±1>

diffraction modes guided inside the nanophosphor structure, with the values of the effective index found around 1.7, namely n_{eff} = 1.73, 1.68 or 1.64 for L= 400, 500 and 600 nm, respectively. Slight variations in the hole size or depth for different imprints may bring small field intensity distribution variations, which resulted in the different effective refractive indices reported. Due to the good agreement achieved in all the three lattice parameters in the whole spectra and angles studied, not only in the first θ_{in} = 0° approximation, we certified that the extinction angular dispersion followed the behavior and was caused by the diffraction orders provided by the periodic structure.

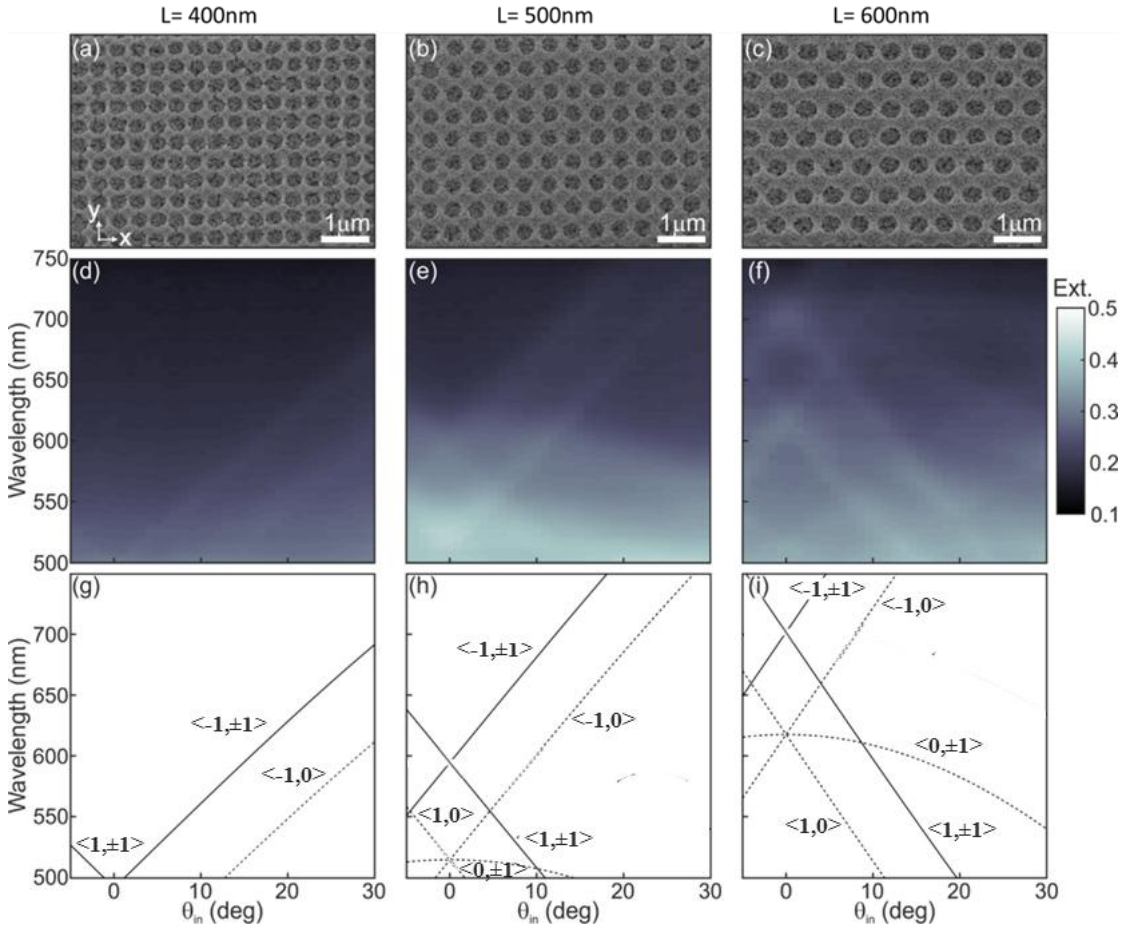

Figure 20. *(**a-c**) SEM images for different lattice parameter of the top view (L = 400, 500 and 600 nm respectively). (**d-f**) Extinction spectra as a function of the incident angle of the patterned samples. (**g-i**) Rayleigh anomalies curves calculated for the diffracted beams. Solid curves represent the diffraction associated to the higher effective refractive index and dashed lines represent the diffraction associated to the lower effective refractive index.*

To understand the behavior of the in-coupling channels generated by the diffraction grating, we did a more in detail study with FDTD method of the sample with L= 600 nm, and also for the flat reference sample (**Figure 21a, f**). The spatial distribution of the electric field intensity, $|E|^2$, and the extinction of an incoming plane electromagnetic wave impinging normally on the samples surface were calculated. Experimental and calculated extinctions showed good agreement for both flat and patterned devices (**Figure 21b, g**) ensuring the good homogeneity and quality of the pattern, with extinction maxima at λ_1=619 nm and λ_2 =696 nm. The first air reflection diffractive order (**Figure 20f, i**, dashed lines) related to the extinction peak of λ_1=619 nm (**Figure 21d**) presented a maximum of 4-fold enhancement of the electric field intensity. The peak related to the <±1, ±1> diffraction modes guided inside the nanophosphor structure at λ_2=696 nm also presented a maximum of 2.5 (**Figure 21e** and **Figure 20i**, dashed lines). In both wavelengths the patterned samples had higher concentrations of the electric field than their flat counterparts (**Figure 21i, j**).

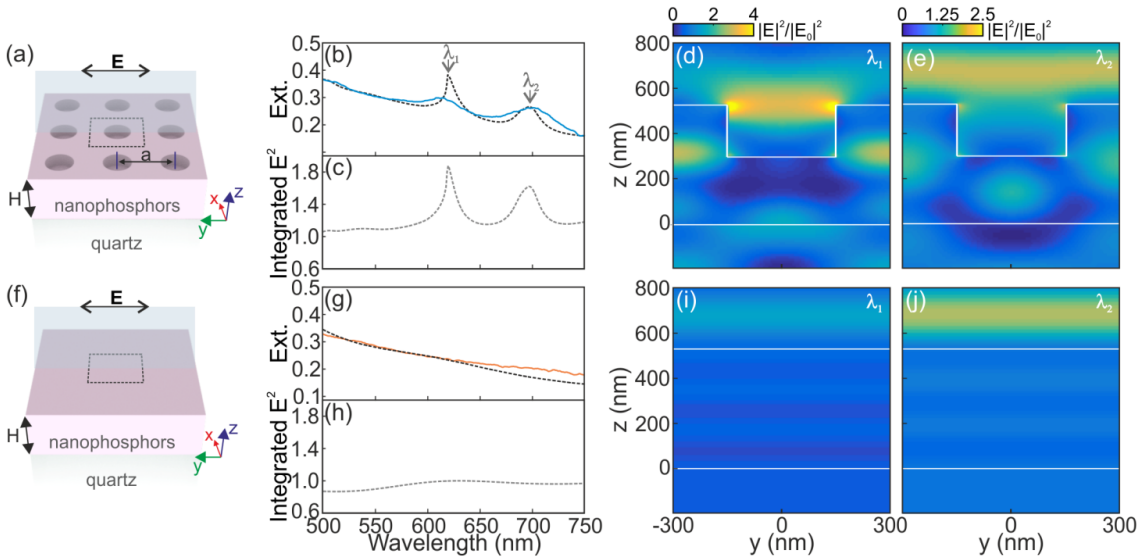

***Figure 21**. (**a**), (**f**) Illustrative schemes of the simulated structures. (**b-e**) FDTD calculations of the structure with the lattice parameter L= 600 nm and (**g-i**) the flat reference. (**b**), (**g**) Calculated (dashed lines) and experimental (solid lines) extinction. The spectral positions of the maxima in extinction of the patterned sample are tagged with arrows (λ_1= 619 nm and λ_2 = 696 nm). Electric field intensity profile along the plane X= 0 of the patterned (**d-e**) and flat (**e-j**) samples at the wavelengths λ_1 (**d**), (**i**) and λ_2 (**e**), (**j**). (**c**), (**h**) Integrated electric field intensity in the entire volume of the nanophosphors normalized to the maximum value for the reference.*

Also, in **Figures 21c** and **21h**, we plotted the result of integrating $|E|^2$ over the entire volume occupied by the nanophosphors. The maximum of the integrated $|E|^2$ inside the patterned sample was found at λ_1=619 nm with almost a 2-fold enhancement against the planar reference. In the λ_2 =696 nm resonance also presented a maximum of 1.6. So, applying the aforementioned reciprocity principle, both diffraction orders should present as an effective way to enhance the directional light out-coupling for a normal 0° emission, as the nanostructure provides the same efficiency for in-coupling than for out-coupling for a specific wavelength. However, a larger enhancement of the PL emission was expected in the wavelengths that interact with the first reflection diffraction order into the air, because of its higher electric field intensity values.

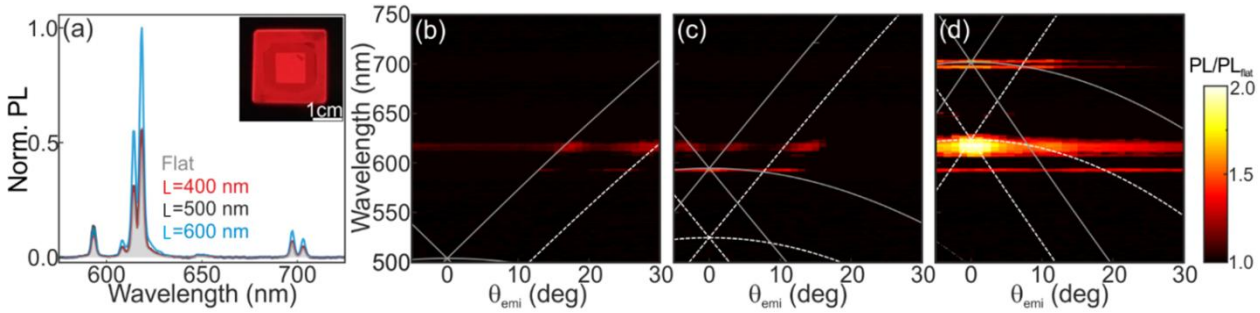

Figure 22. *(**a**) Normal direction emission of the reference (gray) and patterned samples: L= 400 nm (red), L= 500 nm (black) and L= 600 nm (blue). The inset shows a picture taken from a sample under the illumination of a UV lamp. Notice that only the 1 cmx1 cm central area of the sample is patterned. (**b-d**) PL enhancement as a function of the emission angle for the different lattice parameters (400, 500 and 600 nm respectively). Curves correspond to the Rayleigh anomalies calculated for the beams diffracted. Solid and dashed lines represent the diffraction curves corresponding to the lower and higher effective refractive indexes, respectively.*

Once we studied the in-coupling mechanisms of the light into the samples, we focused in the study of the out-coupling mechanism of the emitted light. To do so, we characterized the PL and its angular dependence. First, we mounted the sample in a double goniometer. The two angular degrees of freedom for the sample and the collection system allowed controlling both the excitation and the emission angles independently. The excitation source consisted of a 285 nm LED focused in the sample surface and fixed to be at 40° respect to the sample surface normal, while the detection system consisted of a mobile arm that rotates around the sample. The angular dispersion of the PL ratio between patterned and flat samples, together with the previously calculated diffraction orders present in the system are shown in **Figure 22b-d**

(diffraction orders in white lines)**.** For all three periodicities studied there was directional PL enhancement when a diffraction mode crossed through the emission peaks of the Eu^{3+} cation. As calculated, the largest enhancement was present in the L= 600 nm sample with a maximum 2-fold PL enhancement at λ = 619 nm at 0° (**Figure 22a**). This is where the brightest emission line of the Eu^{3+} coincides with the first reflection diffraction orders into the air. These results are in agreement with the results obtained in **Figures 20** and **21** when studying the light in-coupling for the same sample and the consequences predicted for out-coupling using the reciprocity principle. Samples with L= 400 nm and 500 nm also show PL enhancements of around 1.5 when the RAs and the PL emission peaks of the RE cation are spectrally matched.

To further clarify the origin of the enhanced directional emission, we measured the UV absorption of the samples. This showed that patterned devices presented similar absorptions than flat substrates (**Figure 23**). Therefore the emission was not derived from an enhancement in the absorption due to the structure.

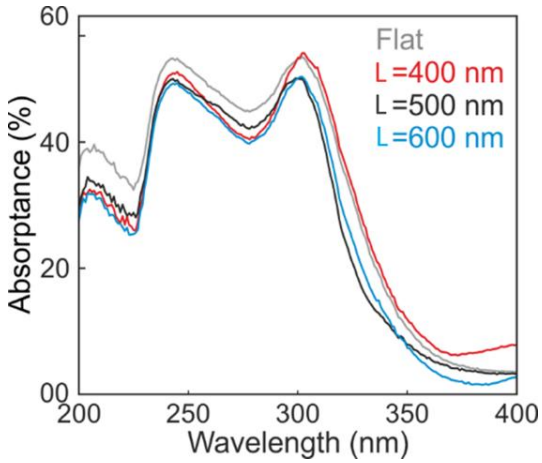

Figure 23. *Absorptance spectra of the reference (gray) and patterned samples: L=400nm (red), L=500nm (black) and L=600nm (blue).*

Further, we measured the PL decay dynamics by multichannel scaling. The analysis showed that the average lifetime of the Eu^{3+} transitions was similar to that of the flat sample (1.39 ± 0.02 ms). This confirms that i) our patterning process does not degrade the emission of the phosphor, and ii) the directional emission enhancement displayed in **Figure 22** is only due to the efficient funneling of the emitted light in particular directions. Consistently, the PLQY remained constant, within experimental error, with respect to the value attained for the reference samples. Flat films showed emitted-to-absorbed photon efficiencies of 55%, while the yields of patterned ones were 56%, 56% and 54% for the lattice parameters 400 nm, 500 nm and 600 nm, respectively. With this last experiment, we certified that was indeed our

designed photonic structure that provided, through the diffraction modes, with out-coupling channels that enhanced the extraction efficiency of the emitted photons.

To sum up, in this project we demonstrated that direct nanoimprinting of nanophosphor layers with 2D square arrays endows the patterned film with enhanced emission at selected wavelengths and directions. Our nanophosphors pastes produced transparent and moldable films that allowed the development of a rare-earth based photonic system that could eventually be put into practice to build more efficient and functional solid-state light emitting devices. Our approach fabricated with inexpensive procedures amenable of mass production also overcame the limitations imposed by the large crystal size of phosphor crystals employed in conventional color converting layers, resulting in high quality and large area photonic architectures.

5.5. Conclusions

In this chapter we successfully integrated diffractive gratings into optoelectronic devices, rendering them with enhanced optical properties. We demonstrated and provided the key guidelines on how these architectures can be implemented in three different type of devices: a solar cell, a photodetector, and an emissive substrate.

There has been always a first step consisting on a conscious pick of the materials used and where to implement the nanostructure. This will allow minimizing the possible detrimental consequences of the patterning. When patterning the solar cell, we chose to pattern the HTL/backelectrode interface. In this case, as in the HTL/backelectrode interface the charge separation has already been done, the recombination of the charges, the V_{oc} losses and Filling factor that may arise due to the defects produced by the structuring were minimized. As a key component of the project, we substituted the most common used HTL layer material (EDT) for a polymeric one, enabling an easy nanoimprinting with solvent assisted soft nanoimprint lithography. In the second section, when nanostructuring the near infrared organic photodetectors, as the filling factor and V_{oc} lose relevance, we were allowed to directly pattern the active layer, in this case by tNIL. The blend mixtures of the active layer were chosen to be inexpensive and easy to produce. In the last project we employed a host vanadate paste containing the emitting rare earth cations as the nanostructured material. We altered the original scheme of fabrication by dispersing it in ethanol prior to the spin coating. In this way we could achieve a non-invasive patterning via sNIL, avoiding possible etching procedures that may have affected the emission rates.

A second step was to design and choose which structures implement in each case. In here FDTD simulation methods and analytical study of the diffraction modes was done to spectrally match the Wood's anomalies and guided modes in the regions of interest. In the case of the CQD solar cell, as the refractive index of the PbS was around 2.5 we used squared arrays with a pitch of 500 nm to fit the diffractive modes around the same position of the excitonic absorptive peak of the QD, located near 1220 nm. Same procedure was carried with the organic photodetectors. As we wanted to demonstrate the feasibility to enhance the photodetection response thorough the entire region with charge transfer absorption, we fabricated devices with the three lattice parameters - 400, 500 and 600 nm-, whose Wood's anomalies fell in the CTA region, from 700 to 1100 nm. In both solar cells and photodetectors, we manage to guide the impinging light of targeted wavelengths into the active layer, maximizing the light-matter interaction and enhancing its absorption. In the third case, as we

want to enhance the out-coupling of the emitted light of the rare earth inside the structure, we must focus in the diffraction of the light to the air. Therefore, we fabricated devices with lattice parameter of L= 600 nm to spectrally match the diffraction mode to the air with the strongest emission line of the nanophosphor. We also fabricated structures with lattice parameters of L= 400 and 500 nm to study the angular dependence of the photoluminescence.

The resulting of the integration of the nanostructure revealed an improvement of the performance of each fabricated device.

- In the case of the CQD solar cells, we increased by a 23% its efficiency in the post silicon range. The IR PCE went from 1.03 to 1.27, setting a new record for this type of cells and spectral region. This was possible thanks to an improvement of the absorption in this range, rendering higher J_{sc}, with no deterioration of the V_{oc} and FF, which were maintained at 0.43V and 55% respectively.
- The nanostructuration in the organic blends enabled its use for photodetection in the NIR, as its EQE was consistently increased in the nanostructured devices. For instance, in the case of PBTTT:$PC_{70}BM$ blends with L= 500 nm, the peaks fell deeper into the NIR (850-920 nm), where a 5-fold increase on conversion efficiency could be seen at 907 nm, with EQE maximum values of 2%. We demonstrated the ability to fabricate spectrally selective organic NIR photodetectors in the whole region with CTA by a rational design of the structures, with no significant increase of the dark currents and non-linearities.
- We demonstrated a 2-fold directional emission enhancement monitored at the most intense emission peak of Eu^{3+}, i.e. λ=619 nm in fabricated devices with lattice parameter of L= 600 nm. We have proven that this PL increase was not due to an increase of absorption or faster emission rates, but as a consequence of a more efficient light out-coupling provided by the structure.

6. General conclusions

This thesis has been devoted to imagine, design, fabricate and characterize large scale photonic architectures to manipulate and enhance light-matter interaction. We have proven the feasibility of the application of periodic nanostructures in a seamless fashion to a wide range of devices through soft NIL. The conscious design of the fabricated structures rendered devices with enhanced optical properties. The main contributions to the field are given below:

- We have presented a strategy that achieves broadband optimal absorption in arbitrarily thin semiconductor materials for all energies above their bandgap. Following this scheme we fabricated samples reaching 81% of total integrated absorption (69% in the semiconductor) over a broad spectral range, from 400 nm to 1500 nm, in an 80 nm germanium photonic crystal built on a gold layer. This stems from the strong interplay between Brewster modes, sustained by judiciously nanostructured thin semiconductors on metal films, and photonic crystal modes. We demonstrate broadband near-unity absorption in Ge ultrathin films that extend from the visible to the Ge bandgap in the near infrared and robust against angle of incidence variation.

- We have designed and fabricated an all-dielectric metamaterial fabricated with a low cost and highly scalable technique: a combination of soft NIL and chemical vapor deposition. The resulting all-dielectric metasurface is composed of an array of silicon hemispheres on top of a high refractive index dielectric waveguide. This architecture supports strong Mie resonances that hybridize with quasi-guided modes and enhance the electromagnetic near-field of the metasurface. Such resonances can be engineered by the design parameters of the nanoimprinted structure. We demonstrated the potential of this platform for enhancing light emission by depositing a NIR dye on the surface for which an 8-fold amplified signal is measured correlated to the optical resonances sustained by the system.

- We have developed a new strategy to nanostructure metal back electrodes that enhance IR photon harvesting with minimal disruption on the fabrication process:

    - In one project we implemented a new hole transport layer and nanostructure it directly. First, we develop a materials set to replace conventional rigid HTLs in CQD devices with a moldable HTL that combines the mechanical and chemical

requisites for NIL with the optoelectronic properties to retain efficient charge extraction through an optically-thick layer. The new HTL is imprinted in a 2D periodic arrangement and conformally coated with MoO_3/Ag. This rendered the solar cell with resonant waveguide grating properties, greatly enhancing the light confinement in it at specific wavelengths. By nanoimpriting designed indentations into the back HTL, we constructed CQD devices that achieve a record photoelectric conversion efficiency of 86% at 1220 nm - a 22% higher PCE compared to the best previous reports.

  - In the second project we demonstrated solution processed organic photodetectors with improved NIR response thanks to a nanostructured active layer in the shape of a 2D resonant waveguide grating. The latter strongly increases the charge transfer state absorption, which is normally weak but broadband, increasing the optical path of light and resulting in remarkable photoresponse significantly below the band gap of the blend. 5-fold EQE enhancements are achieved. On top of that, by varying the lattice parameter of the photonic crystal structure, the spectral response of the photodetectors is tuned beyond 1000 nm.

- We developed a low-cost soft NIL procedure can be applied to red-emitting nanophosphors (GdVO4:Eu3+ nanocrystals) to tune their emission properties. A square array of nanoholes with different lattice parameters constructed on down-shifting nanophosphors rendered them with quasi guided modes that can be used for light out-coupling. This attained for a 2-fold directional enhancement of the emitted light at predesigned emission wavelengths in specific directions.

Final Remarks

This thesis is another demonstration of the impact that nanotechnology and the new nanofabrication techniques have, and will have, in the state of art optoelectronic devices. A correct design and fabrication of specific nanostructures it has become essential to maximize the efficiency of them. In this work, we have tried to shine a little light upon how to develop strategies to integrate such nanostructures in a seamless and scalable fashion, with several examples of the designs and applications that can be achieved.

7. Scientific contributions

7.1. Articles derived from this thesis

1. Molet P, Garcia-Pomar J L, Matricardi C, Garriga M, Alonso M I, Mihi A. *Ultrathin Semiconductor Superabsorbers from the Visible to the Near-Infrared*. **Advanced Materials**. 2018; 30: 1705876

2. Molet P, Gil-Herrera L K, Garcia-Pomar J L, et al. *Large area metasurfaces made with spherical silicon resonators*. **Nanophotonics**. 2020; 9: 943–951

3. Baek S, Molet P, Choi M, et al. *Nanostructured Back Reflectors for Efficient Colloidal Quantum-Dot Infrared Optoelectronics*. **Advanced Materials**. 2019; 1901745

4. Gibert-Roca M, Molet P, Mihi A, Campoy-Quiles M. *Near infrared organic photodetectors based on enhanced charge transfer state absorption by photonic architectures*. **Journal of Materials Chemistry C**. 2020; 8: 9688–9696

5. Cabello-Olmo E, Molet P, Mihi A, Lozano G, Míguez H. *Enhanced Directional Light Extraction from Patterned Rare-Earth Phosphor Films*. **Advanced Optical Materials**. 2021; 9: 2001611

6. Matricardi C, Garcia-Pomar J L, Molet P, et al. *High-Throughput Nanofabrication of Metasurfaces with Polarization-Dependent Response*. **Advanced Optical Materials**. 2020; *8*: 2000786

7. Molet P, Passarelli N et al. *Engineering Colloidal Meta-Molecules for Tunable Plasmonic Photonic Crystals* **Submitted**

8. Molet P, Torras M, Roig A, Mihi A. *Optical and photocatalytic properties of in-situ microwave-grown gold nanoparticles on nanostructured mesoporous TiO_2* **In preparation**

7.2. Conference presentations

1. *Ultrathin Semiconductor Superabsorbers from the Visible to the Near Infrared.* **ImagineNano**, *Bilbao*, 2018.

2. *Ultrathin Semiconductor Superabsorbers from the Visible to the Near Infrared.* **Schools on the Frontiers of Light**, *ICFO (Barcelona)*, 2018.

3. *Ultrathin Semiconductor Superabsorbers from the Visible to the Near Infrared.* **Matener**, *ICMAB (Barcelona)*, 2018.

4. *Nanostructured high dielectric semiconductor ultrathin films with enhanced broadband absorption in the visible and NIR regime.* **MRS Fall meeting**, *Boston*, 2018.

5. *Managing light with high index photonic architectures.* **Amolf Summerschool**, *Amsterdam*, 2019.

6. *Managing light with high index photonic architectures.* **META Spring**, *Lisbon*, 2019.

7. *Managing light with high index photonic architectures.* **JHPHD**, *ICMAB (Barcelona)*, 2019.

8. *High-Throughput Nanofabrication of Metasurfaces with Polarization-Dependent Response and application to quantum dot solar cells.* **Photonics Online Meetup**, *Online*, 2020.

9. *High-Throughput Nanofabrication of Metasurfaces with Polarization-Dependent Response and application to quantum dot solar cells.* **JHPHD** , *ICMAB (Barcelona)*, 2020.

10. *High-Throughput Nanofabrication of Metasurfaces with Polarization-Dependent Response and application to quantum dot solar cells.* **CEN**, *Online*, 2020.

8. References

[1] Mihi A, Beck F J, Lasanta T, Rath A K, Konstantatos G. Imprinted Electrodes for Enhanced Light Trapping in Solution Processed Solar Cells. Advanced Materials. 2014; *26*: 443–448

[2] Xia Y, Whitesides G M. Soft Lithography. Angewandte Chemie International Edition. 1998; *37*: 550–575

[3] Xia Y, Rogers J A, Paul K E, Whitesides G M. Unconventional Methods for Fabricating and Patterning Nanostructures. Chem. Rev. 1999; *99*: 1823–1848

[4] Qin D, Xia Y, Whitesides G M. Soft lithography for micro- and nanoscale patterning. Nature Protocols. 2010; *5*: 491–502

[5] Weiner J, Nunes F. Light-Matter Interaction. Light-Matter Interaction, Oxford University Press. , 2012;

[6] Lee S, Sun Y, Cao Y, Kang S H. Plasmonic nanostructure-based bioimaging and detection techniques at the single-cell level. TrAC - Trends in Analytical Chemistry. 2019; *117*: 58–68

[7] Xu Y, Bai P, Zhou X, et al. Optical Refractive Index Sensors with Plasmonic and Photonic Structures: Promising and Inconvenient Truth. Advanced Optical Materials. 2019; *7*: 1801433

[8] Li Y, Kovačič M, Westphalen J, et al. Tailor-made nanostructures bridging chaos and order for highly efficient white organic light-emitting diodes. Nature Communications. 2019; *10*: 1–11

[9] Liu Q, Romero-Gomez P, Mantilla-Perez P, Colodrero S, Toudert J, Martorell J. A Two-Resonance Tapping Cavity for an Optimal Light Trapping in Thin-Film Solar Cells. Advanced Energy Materials. 2017; *7*: 1700356

[10] Komar A, Paniagua-Domínguez R, Miroshnichenko A, et al. Dynamic Beam Switching by Liquid Crystal Tunable Dielectric Metasurfaces. ACS Photonics. 2018; *5*: 1742–1748

[11] Adato R, Guo J. Modification of dispersion, localization, and attenuation of thin metal stripe symmetric surface plasmon-polariton modes by thin dielectric layers. Journal of

Applied Physics. 2009; *105*: 034306

[12] Kayes B M, Nie H, Twist R, et al. 27.6% Conversion efficiency, a new record for single-junction solar cells under 1 sun illumination. in *Conf. Rec. IEEE Photovolt. Spec. Conf.*, 2011, pp. 04–08

[13] Andreani L C, Bozzola A, Kowalczewski P, Liscidini M, Redorici L. Silicon solar cells: toward the efficiency limits. Advances in Physics: X. 2019; *4*: 1548305

[14] Tang L, Kocabas S E, Latif S, et al. Nanometre-scale germanium photodetector enhanced by a near-infrared dipole antenna. Nature Photonics. 2008; *2*: 226–229

[15] Geum D M, Kim S H, Kim S K, et al. Monolithic integration of visible GaAs and near-infrared InGaAs for multicolor photodetectors by using high-throughput epitaxial lift-off toward high-resolution imaging systems. Scientific Reports. 2019; *9*: 1–12

[16] Novotny L, Van Hulst N. Antennas for light. Nature Photonics. 2011; *5*: 83–90

[17] Míguez H, Chomski E, García-Santamaría F, et al. Photonic Bandgap Engineering in Germanium Inverse Opals by Chemical Vapor Deposition. Advanced Materials. 2001; *13*: 1634–1637

[18] Staude I, Schilling J. Metamaterial-inspired silicon nanophotonics. Nature Photonics. 2017; *11*: 274–284

[19] Higashihara T, Ueda M. Recent progress in high refractive index polymers. Macromolecules. 2015; *48*: 1915–1929

[20] Liu J G, Ueda M. High refractive index polymers: Fundamental research and practical applications. Journal of Materials Chemistry. 2009; *19*: 8907–8919

[21] Pascual-San-José E, Rodríguez-Martínez X, Adel-Abdelaleim R, Stella M, Martínez-Ferrero E, Campoy-Quiles M. Blade coated P3HT:non-fullerene acceptor solar cells: A high-throughput parameter study with a focus on up-scalability. Journal of Materials Chemistry A. 2019; *7*: 20369–20382

[22] Gibert-Roca M, Molet P, Mihi A, Campoy-Quiles M. Near infrared organic photodetectors based on enhanced charge transfer state absorption by photonic architectures. Journal of Materials Chemistry C. 2020; *8*: 9688–9696

[23] Krogman K C, Druffel T, Sunkara M K. Anti-reflective optical coatings incorporating

nanoparticles. Nanotechnology. 2005; *16*: 338

[24] Perot A, Fabry C. On the Application of Interference Phenomena to the Solution of Various Problems of Spectroscopy and Metrology. The Astrophysical Journal. 1899; *9*: 87

[25] Gires F, Tournois P. An interferometer useful for pulse compression of a frequency modulated light pulse. C. R. Acad. Sci. Paris. 1964; *258*: 6112–6115

[26] Bitarafan M H, DeCorby R G. On-chip high-finesse fabry-perot microcavities for optical sensing and quantum information. Sensors (Switzerland). 2017; *17*: 1748

[27] Williams B S. Terahertz quantum-cascade lasers. Nature Photonics. 2007; *1*: 517–525

[28] Macleod H A. Thin-Film Optical Filters . Thin-Film Optical Filters , CRC Press. , 2018;

[29] Chang C C, Sirkis J. Multiplexed optical fiber sensors using a single Fabry-Perot resonator for phase modulation. Journal of Lightwave Technology. 1996; *14*: 1653–1663

[30] Konishi N, Suzuki T, Taira Y, Kato H, Kasuya T. High precision wavelength meter with Fabry-Perot optics. Applied Physics. 1981; *25*: 311–316

[31] Pisani M, Zucco M E. Compact imaging spectrometer combining Fourier transform spectroscopy with a Fabry-Perot interferometer. Optics Express. 2009; *17*: 8319

[32] Kitagawa K. Thin-film thickness profile measurement by three-wavelength interference color analysis. Applied Optics. 2013; *52*: 1998–2007

[33] Kats M a., Blanchard R, Genevet P, Capasso F. Nanometre optical coatings based on strong interference effects in highly absorbing media. Nature Materials. 2012; *12*: 20–24

[34] Wang K X, Yu Z, Liu V, Cui Y, Fan S. Absorption Enhancement in Ultrathin Crystalline Silicon Solar Cells with Antireflection and Light-Trapping Nanocone Gratings. Nano Letters. 2012; *12*: 1616–1619

[35] Tang Z, Ma Z, Sánchez-Díaz A, et al. Polymer:Fullerene Bimolecular Crystals for Near-Infrared Spectroscopic Photodetectors. Advanced Materials. 2017; *29*: 1–8

[36] Barish B C, Weiss R. LIGO and the Detection of Gravitational Waves. Physics Today.

1999; *52*: 44–50

[37] Kuznetsov A I, Miroshnichenko A E, Brongersma M L, Kivshar Y S, Luk'yanchuk B. Optically resonant dielectric nanostructures. Science. 2016; *354*: aag2472

[38] Yu Y F, Zhu A Y, Paniagua-Domínguez R, Fu Y H, Luk'yanchuk B, Kuznetsov A I. High-transmission dielectric metasurface with 2π phase control at visible wavelengths. Laser and Photonics Reviews. 2015; *9*: 412–418

[39] Decker M, Staude I, Falkner M, et al. High-Efficiency Dielectric Huygens' Surfaces. Advanced Optical Materials. 2015; *3*: 813–820

[40] Cubukcu E, Kort E A, Crozier K B, Capasso F. Plasmonic laser antenna. Applied Physics Letters. 2006; *89*: 093120

[41] Halas N J, Lal S, Chang W S, Link S, Nordlander P. Plasmons in strongly coupled metallic nanostructures. Chemical Reviews. 2011; *111*: 3913–3961

[42] Sigalas M M, Fattal D A, Williams R S, Wang S Y, Beausoleil R G. Electric field enhancement between two Si microdisks. Optics Express. 2007; *15*: 14711

[43] Hayashi S, Koh R, Ichiyama Y, Yamamoto K. Evidence for surface-enhanced Raman scattering on nonmetallic surfaces: Copper phthalocyanine molecules on GaP small particles. Physical Review Letters. 1988; *60*: 1085–1088

[44] Albella P, Poyli M A, Schmidt M K, et al. Low-loss electric and magnetic field-enhanced spectroscopy with subwavelength silicon dimers. Journal of Physical Chemistry C. 2013; *117*: 13573–13584

[45] Bakker R M, Permyakov D, Yu Y F, et al. Magnetic and Electric Hotspots with Silicon Nanodimers. Nano Letters. 2015; *15*: 2137–2142

[46] Bakker R M, Permyakov D, Yu Y F, et al. Magnetic and electric hotspots with silicon nanodimers. Nano Letters. 2015; *15*: 2137–2142

[47] Matricardi C, Hanske C, Garcia-Pomar J L, Langer J, Mihi A, Liz-Marzán L M. Gold Nanoparticle Plasmonic Superlattices as Surface-Enhanced Raman Spectroscopy Substrates. ACS Nano. 2018; *12*: 8531–8539

[48] Sortino L, Zotev P G, Mignuzzi S, et al. Enhanced light-matter interaction in an atomically thin semiconductor coupled with dielectric nano-antennas. Nature

Communications. 2019; *10*: 5119

[49] Rolly B, Stout B, Bonod N. Boosting the directivity of optical antennas with magnetic and electric dipolar resonant particles. Optics Express. 2012; *20*: 20376

[50] Murai S, Tokuda Y, Fujita K, Tanaka K. Tuning the wavelength of amplified spontaneous emission coupled to localized surface plasmon. Applied Physics Letters. 2012; *101*: 031117

[51] Rolly B, Bebey B, Bidault S, Stout B, Bonod N. Promoting magnetic dipolar transition in trivalent lanthanide ions with lossless Mie resonances. Physical Review B - Condensed Matter and Materials Physics. 2012; *85*: 245432

[52] Week 3 The quantum world: 3 Diffraction of waves - OpenLearn - Open University - MG_1. "Week 3 The quantum world: 3 Diffraction of waves - OpenLearn - Open University - MG_1," n.d.

[53] Diffraction Grating. "Diffraction Grating," can be found under http://hyperphysics.phy-astr.gsu.edu/hbase/phyopt/grating.html, n.d.

[54] 3.3: Diffraction Gratings - Physics LibreTexts. "3.3: Diffraction Gratings - Physics LibreTexts," can be found under https://phys.libretexts.org/Courses-/University_of_California_Davis/UCD%3A_Physics_9B__Waves_Sound_Optics_Thermodynamics_and_Fluids/03%3A_Physical_Optics/3.03%3A_Diffraction_Gratings, n.d.

[55] Wang X, Shi W, Yun H, Grist S, Jaeger N A F, Chrostowski L. Narrow-band waveguide Bragg gratings on SOI wafers with CMOS-compatible fabrication process. Optics Express. 2012; *20*: 15547

[56] Kneubühl F. Diffraction Grating Spectroscopy. Applied Optics. 1969; *8*: 505

[57] Massenot S. Volume diffraction gratings for optical telecommunications applications: design study for a spectral equalizer. Optical Engineering. 2004; *43*: 2658

[58] Mayer J, Gallinet B, Offermans T, Ferrini R. Diffractive nanostructures for enhanced light-harvesting in organic photovoltaic devices. Optics Express. 2016; *24*: A358

[59] Schimert T R, Barnes S L, Brouns A J, Case F C, Mitra P, Claiborne L T. Enhanced quantum well infrared photodetector with novel multiple quantum well grating structure. Cite as: Appl. Phys. Lett. 1996; *68*: 2846

[60] Wang Y, Aravind I, Cai Z, et al. Hot Electron Driven Photocatalysis on Plasmon-Resonant Grating Nanostructures. ACS Applied Materials and Interfaces. 2020; *12*: 17459–17465

[61] Ĺv̂que G, Martin O J F. Optimization of finite diffraction gratings for the excitation of surface plasmons. Journal of Applied Physics. 2006; *100*: 124301

[62] Wang S S, Moharam M G, Magnusson R, Bagby J S. Guided-mode resonances in planar dielectric-layer diffraction gratings. Journal of the Optical Society of America A. 1990; *7*: 1470

[63] Lee K K, Avniel Y, Johnson S G. Rigorous sufficient conditions for index-guided modes in microstructured dielectric waveguides. Optics Express. 2008; *16*: 9261

[64] Gambling W A. The rise and rise of optical fibers. IEEE Journal on Selected Topics in Quantum Electronics. 2000; *6*: 1084–1093

[65] Senior J M, Jamro M Y. Optical fiber communications: principles and practice. Optical Fiber Communications: Principles and Practice, Pearson Education. , 2009;

[66] Brongersma M L, Cui Y, Fan S. Light management for photovoltaics using high-index nanostructures. Nature materials. 2014; *13*: 451–60

[67] Maurel A, Félix S, Mercier J F, Ourir A, Djeffal Z E. Wood's anomalies for arrays of dielectric scatterers. Journal of the European Optical Society. 2014; *9*: 1–7

[68] Tiguntseva E, Chebykin A, Ishteev A, et al. Resonant silicon nanoparticles for enhancement of light absorption and photoluminescence from hybrid perovskite films and metasurfaces. Nanoscale. 2017; *9*: 12486–12493

[69] Le Ru E C, Etchegoin P G. Principles of surface-enhanced Raman spectroscopy and related plasmonic effects. Principles of Surface-Enhanced Raman Spectroscopy and Related Plasmonic Effects, Elsevier, Oxford. , 2009;

[70] Taliercio T, Ntsame Guilengui V, Cerutti L, et al. Light propagation with phase discontinuities: generalized laws of reflection and refraction. Appl. Phys. Lett. 2005; *5*: 122411

[71] Paniagua-Domínguez R, Yu Y F, Miroshnichenko A E, et al. Generalized Brewster effect in dielectric metasurfaces. Nature Communications. 2016; *7*: 10362

[72] Park J, Kang J-H, Vasudev A P, et al. Omnidirectional Near-Unity Absorption in an

Ultrathin Planar Semiconductor Layer on a Metal Substrate. ACS Photonics. 2014; *1*: 812–821

[73] Xiao C, Chen Z, Qin M, Zhang D, Fan L. SPPs characteristics of Ag/SiO2 sinusoidal nano-grating in SERS application. Optik. 2018; *168*: 650–659

[74] Gómez-Castaño M, Zheng H, García-Pomar J L, Vallée R, Mihi A, Ravaine S. Tunable index metamaterials made by bottom-up approaches. Nanoscale Advances. 2019; *1*: 1070–1076

[75] Westphalen M, Kreibig U, Rostalski J, Lüth H, Meissner D. Metal cluster enhanced organic solar cells. Solar Energy Materials and Solar Cells. 2000; *61*: 97–105

[76] Quail J C, Simon H J. Second-harmonic generation with phase-matched long-range and short-range surface plasmons. Journal of Applied Physics. 1984; *56*: 2589–2591

[77] Li J, Cushing S K, Zheng P, Meng F, Chu D, Wu N. Plasmon-induced photonic and energy-transfer enhancement of solar water splitting by a hematite nanorod array. Nature Communications. 2013; *4*: 2651

[78] Taliercio T, Guilengui V N, Cerutti L, Tournié E, Greffet J-J. Brewster “mode” in highly doped semiconductor layers: an all-optical technique to monitor doping concentration. Optics Express. 2014; *22*: 24294

[79] Capper P, Irvine S, Joyce T. Epitaxial crystal growth: methods and materials. in *Springer Handbooks*, Springer. , 2017, p. 1

[80] Wang W B, Chang N N, Codding T A, Girolami G S, Abelson J R. Superconformal chemical vapor deposition of thin films in deep features. Journal of Vacuum Science & Technology A: Vacuum, Surfaces, and Films. 2014; *32*: 051512

[81] Chou S Y, Krauss P R, Renstrom P J. Nanoimprint lithography. n.d.;

[82] Krauss P R, Chou S Y. Sub-10 nm imprint lithography and applications. in *Annu. Device Res. Conf. Dig.*, IEEE. , 1997, pp. 90–91

[83] Yu C C, Chen H L. Nanoimprint technology for patterning functional materials and its applications. Microelectronic Engineering. 2015; *132*: 98–119

[84] Jeong B, Han H, Kim H H, Choi W K, Park Y J, Park C. Polymer-Assisted Nanoimprinting for Environment- And Phase-Stable Perovskite Nanopatterns. ACS Nano. 2020; *14*:

1645–1655

[85] Jiang Y, Luo B, Cheng X. Enhanced thermal stability of thermoplastic polymer nanostructures for nanoimprint lithography. Materials. 2019; *12*: 545

[86] Schuster C, Reuther F, Kolander A, Gruetzner G. mr-NIL 6000LT - Epoxy-based curing resist for combined thermal and UV nanoimprint lithography below 50 °C. Microelectronic Engineering. 2009; *86*: 722–725

[87] Espinha A, Dore C, Matricardi C, Alonso M I, Goñi A R, Mihi A. Hydroxypropyl cellulose photonic architectures by soft nanoimprinting lithography. Nature Photonics. 2018; *12*: 343–348

[88] Gómez-Castaño M, Garcia-Pomar J L, Pérez L A, Shanmugathasan S, Ravaine S, Mihi A. Electrodeposited Negative Index Metamaterials with Visible and Near Infrared Response. Advanced Optical Materials. 2020; *8*: 2000865

[89] Chen X, Zhang L. Review in manufacturing methods of nanochannels of bio-nanofluidic chips. Sensors and Actuators, B: Chemical. 2018; *254*: 648–659

[90] Lochmann S, Grothe J, Eckhardt K, Leistenschneider D, Borchardt L, Kaskel S. Nanoimprint lithography of nanoporous carbon materials for micro-supercapacitor architectures. Nanoscale. 2018; *10*: 10109–10115

[91] Chou S Y, Krauss P R, Renstrom P J. Imprint of sub-25 nm vias and trenches in polymers. Applied Physics Letters. 1995; *67*: 3114

[92] Austin M D, Ge H, Wu W, et al. Fabrication of 5 nm linewidth and 14 nm pitch features by nanoimprint lithography. Applied Physics Letters. 2004; *84*: 5299–5301

[93] Odom T W, Love J C, Wolfe D B, Paul K E, Whitesides G M. Improved pattern transfer in soft lithography using composite stamps. Langmuir. 2002; *18*: 5314–5320

[94] Inglis D W. A method for reducing pressure-induced deformation in silicone microfluidics. Biomicrofluidics. 2010; *4*: 026504

[95] Johnson P B, Christy R W. Optical Constants of the Noble Metals. Physical Review B. 1972; *6*: 4370–4379

[96] König T A F, Ledin P A, Kerszulis J, et al. Electrically tunable plasmonic behavior of nanocube-polymer nanomaterials induced by a redox-active electrochromic polymer.

ACS Nano. 2014; *8*: 6182–6192

[97] Stelling C, Singh C R, Karg M, König T A F, Thelakkat M, Retsch M. Plasmonic nanomeshes: Their ambivalent role as transparent electrodes in organic solar cells. Scientific Reports. 2017; *7*: 1–13

[98] Siefke T, Kroker S, Pfeiffer K, et al. Materials Pushing the Application Limits of Wire Grid Polarizers further into the Deep Ultraviolet Spectral Range. Advanced Optical Materials. 2016; *4*: 1780–1786

[99] Pierce D T, Spicer W E. Electronic structure of amorphous Si from photoemission and optical studies. Physical Review B. 1972; *5*: 3017–3029

[100] Lajaunie L, Boucher F, Dessapt R, Moreau P. Strong anisotropic influence of local-field effects on the dielectric response of α-MoO3. Physical Review B - Condensed Matter and Materials Physics. 2013; *88*: 115141

[101] Green M A, Emery K, Hishikawa Y, et al. Solar cell efficiency tables (version 49). Progress in Photovoltaics: Research and Applications. 2017; *25*: 3–13

[102] Pizzini S. Advanced silicon materials for photovoltaic applications. Advanced Silicon Materials for Photovoltaic Applications, Wiley, Chichester. , 2012;

[103] Schiff E A, Schiff E A. Low-Mobility Solar Cells: a Device Physics Primer with Application to Amorphous Silicon. Solar Energy Materials & Solar Cells. 2003; *78*: 567–595

[104] Lee K, Lee J, Mazor B A, Forrest S R. Transforming the cost of solar-to-electrical energy conversion: Integrating thin-film GaAs solar cells with non-tracking mini-concentrators. Light: Science & Applications. 2015; *4*: e288

[105] John S. Why trap light? Nature Materials. 2012; *11*: 997–999

[106] Yablonovitch E. Statistical ray optics. Journal of the Optical Society of America. 1982; *72*: 899

[107] Yablonovitch E, Cody G D. Intensity enhancement in textured optical sheets for solar cells. IEEE Transactions on Electron Devices. 1982; *29*: 300–305

[108] Ingenito A, Isabella O, Zeman M. Experimental Demonstration of 4 n^2 Classical Absorption Limit in Nanotextured Ultrathin Solar Cells with Dielectric Omnidirectional Back Reflector. ACS Photonics. 2014; *1*: 270–278

[109] Rogers J A, Ahn J-H. Silicon nanomembranes : fundamental science and applications. Silicon Nanomembranes : Fundamental Science and Applications, Wiley-VCH, Weinheim. Weinheim, 2016;

[110] Chiechi R C, Havenith R W A, Hummelen J C, Koster L J A, Loi M A. Modern plastic solar cells: materials, mechanisms and modeling. Materials Today. 2013; *16*: 281–289

[111] Zheng Z, Ji H, Yu P, Wang Z. Recent Progress Towards Quantum Dot Solar Cells with Enhanced Optical Absorption. Nanoscale Research Letters. 2016; *11*: 266

[112] Carey G H, Abdelhady A L, Ning Z, Thon S M, Bakr O M, Sargent E H. Colloidal Quantum Dot Solar Cells. Chemical Reviews. 2015; *115*: 12732–12763

[113] Ochiai T, Sakoda K. Dispersion relation and optical transmittance of a hexagonal photonic crystal slab. Physical Review B. 2001; *63*: 125107

[114] Fan S, Joannopoulos J D. Analysis of guided resonances in photonic crystal slabs. Physical Review B. 2002; *65*: 235112

[115] Atwater H A, Polman A. Plasmonics for improved photovoltaic devices. Nature Materials. 2010; *9*: 205–213

[116] Tan H, Santbergen R, Smets A H M, Zeman M. Plasmonic Light Trapping in Thin-film Silicon Solar Cells with Improved Self-Assembled Silver Nanoparticles. Nano Letters. 2012; *12*: 4070–4076

[117] Zhao Q, Zhou J, Zhang F, Lippens D. Mie resonance-based dielectric metamaterials. Materials Today. 2009; *12*: 60–69

[118] Spinelli P, Verschuuren M A, Polman A, Polman A, Vahala K J. Broadband omnidirectional antireflection coating based on subwavelength surface Mie resonators. Nature Communications. 2012; *3*: 692

[119] Park J, Kim S J, Brongersma M L. Condition for unity absorption in an ultrathin and highly lossy film in a Gires-Tournois interferometer configuration. Optics Letters. 2015; *40*: 1960

[120] Yu Z, Raman A, Fan S. Fundamental limit of nanophotonic light trapping in solar cells. Proceedings of the National Academy of Sciences of the United States of America. 2010; *107*: 17491–6

[121] Munday J N, Callahan D M, Atwater H A. Light trapping beyond the 4 n^2 limit in thin waveguides. Applied Physics Letters. 2012; *100*: 121121

[122] Maier S A. Plasmonics : fundamentals and applications. Plasmonics : Fundamentals and Applications, Springer, New York. , 2007;

[123] Sun Z, Zuo X, Guan T, Chen W. Artificial TE-mode surface waves at metal surfaces mimicking surface plasmons. Optics Express. 2014; *22*: 4714

[124] Steenhoff V, Theuring M, Vehse M, von Maydell K, Agert C. Ultrathin Resonant-Cavity-Enhanced Solar Cells with Amorphous Germanium Absorbers. Advanced Optical Materials. 2015; *3*: 182–186

[125] Dotan H, Kfir O, Sharlin E, et al. Resonant light trapping in ultrathin films for water splitting. Nature Materials. 2012; *12*: 158–164

[126] Raether H. Surface Plasmons on Smooth and Rough Surfaces and on Gratings. Surface Plasmons on Smooth and Rough Surfaces and on Gratings, Springer Berlin Heidelberg. Berlin, Heidelberg, 1988;

[127] Dionne J A, Sweatlock L A, Atwater H A, Polman A. Planar metal plasmon waveguides: frequency-dependent dispersion, propagation, localization, and loss beyond the free electron model. Physical Review B. 2005; *72*: 075405

[128] García-Etxarri A, Gómez-Medina R, Froufe-Pérez L S, et al. Strong magnetic response of submicron Silicon particles in the infrared. Optics Express. 2011; *19*: 4815

[129] Odebo Länk N, Verre R, Johansson P, Käll M. Large-Scale Silicon Nanophotonic Metasurfaces with Polarization Independent Near-Perfect Absorption. Nano Letters. 2017; acs.nanolett.7b00416

[130] Ghobadi A, Ulusoy Ghobadi T G, Karadas F, Ozbay E. Semiconductor Thin Film Based Metasurfaces and Metamaterials for Photovoltaic and Photoelectrochemical Water Splitting Applications. Advanced Optical Materials. 2019; *7*: 1900028

[131] Krasnok A E, Miroshnichenko A E, Belov P A, Kivshar Y S. All-dielectric optical nanoantennas. Optics Express. 2012; *20*: 20599

[132] Rodriguez I, Shi L, Lu X, Korgel B A, Alvarez-Puebla R A, Meseguer F. Silicon nanoparticles as Raman scattering enhancers. Nanoscale. 2014; *6*: 5666–5670

[133] Albella P, Poyli M A, Schmidt M K, et al. Low-Loss Electric and Magnetic Field-Enhanced Spectroscopy with Subwavelength Silicon Dimers. The Journal of Physical Chemistry C. 2013; *117*: 13573–13584

[134] Deng F, Liu H, Panmai M, Lan S. Sharp bending and power distribution of a focused radially polarized beam by using silicon nanoparticle dimers. Optics Express. 2018; *26*: 20051

[135] Castellanos G W, Bai P, Gómez Rivas J. Lattice resonances in dielectric metasurfaces. Journal of Applied Physics. 2019; *125*: 213105

[136] Solomon M L, Hu J, Lawrence M, García-Etxarri A, Dionne J A. Enantiospecific Optical Enhancement of Chiral Sensing and Separation with Dielectric Metasurfaces. ACS Photonics. 2019; *6*: 43–49

[137] Babicheva V E, Moloney J V. Lattice effect on electric and magnetic resonance overlap in periodic array. Nanophotonics. 2018; *7*: 1663–1668

[138] Leung S-F, Gu L, Zhang Q, et al. Roll-to-roll fabrication of large scale and regular arrays of three-dimensional nanospikes for high efficiency and flexible photovoltaics. Scientific Reports. 2014; *4*: 094507

[139] Wood T, Naffouti M, Berthelot J, et al. All-Dielectric Color Filters Using SiGe-Based Mie Resonator Arrays. ACS Photonics. 2017; *4*: 873–883

[140] Epstein A, Eleftheriades G V. Huygens' metasurfaces via the equivalence principle: design and applications. Journal of the Optical Society of America B. 2016; *33*: A31

[141] Paniagua-Domínguez R, Yu Y F, Khaidarov E, et al. A Metalens with a Near-Unity Numerical Aperture. Nano Letters. 2018; *18*: 2124–2132

[142] Ibisate M, Golmayo D, López C. Silicon direct opals. Advanced Materials. 2009; *21*: 2899–2902

[143] Fenollosa R, Garín M, Meseguer F. Spherical silicon photonic microcavities: From amorphous to polycrystalline. Physical Review B. 2016; *93*: 235307

[144] Fu Y H, Kuznetsov A I, Miroshnichenko A E, Yu Y F, Luk'yanchuk B. Directional visible light scattering by silicon nanoparticles. Nature Communications. 2013; *4*: 1527

[145] Blanco A, Chomski E, Grabtchak S, et al. Large-scale synthesis of a silicon photonic

crystal with a complete three-dimensional bandgap near 1.5 micrometres. Nature. 2000; *405*: 437–440

[146] García-Santamaría F, Ibisate M, Rodríguez I, Meseguer F, López C. Photonic Band Engineering in Opals by Growth of Si/Ge Multilayer Shells. Advanced Materials. 2003; *15*: 788–792

[147] Ma C, Yan J, Huang Y, Yang G. Photoluminescence manipulation of WS 2 flakes by an individual Si nanoparticle. Materials Horizons. 2019; *6*: 97–106

[148] Garín M, Solà M, Julian A, Ortega P. Enabling silicon-on-silicon photonics with pedestalled Mie resonators. Nanoscale. 2018; *10*: 14406–14413

[149] Zywietz U, Evlyukhin A B, Reinhardt C, Chichkov B N. Laser printing of silicon nanoparticles with resonant optical electric and magnetic responses. Nature Communications. 2014; *5*: 3402

[150] Li X, Pyatenko A, Shimizu Y, Wang H, Koga K, Koshizaki N. Fabrication of Crystalline Silicon Spheres by Selective Laser Heating in Liquid Medium. Langmuir. 2011; *27*: 5076–5080

[151] Kuzmin P G, Shafeev G A, Bukin V V., et al. Silicon nanoparticles produced by femtosecond laser ablation in ethanol: Size control, structural characterization, and optical properties. Journal of Physical Chemistry C. 2010; *114*: 15266–15273

[152] Chaâbani W, Proust J, Movsesyan A, et al. Large-Scale and Low-Cost Fabrication of Silicon Mie Resonators. ACS Nano. 2019; *13*: 4199–4208

[153] Moitra P, Slovick B A, li W, et al. Large-Scale All-Dielectric Metamaterial Perfect Reflectors. ACS Photonics. 2015; *2*: 692–698

[154] Campione S, Basilio L I, Warne L K, Sinclair M B. Tailoring dielectric resonator geometries for directional scattering and Huygens' metasurfaces. Optics Express. 2015; *23*: 2293

[155] Molet P, Garcia-Pomar J L, Matricardi C, Garriga M, Alonso M I, Mihi A. Ultrathin Semiconductor Superabsorbers from the Visible to the Near-Infrared. Advanced Materials. 2018; *30*: 1705876

[156] Garcia-Pomar J L, Molet Bachs P, Mihi A. multipole decomposition of dielectric

nanoparticles in an array. “multipole decomposition of dielectric nanoparticles in an array,” can be found under https://zenodo.org/record/4009029, 2020

[157] Babicheva V E, Evlyukhin A B. Resonant Lattice Kerker Effect in Metasurfaces With Electric and Magnetic Optical Responses. Laser and Photonics Reviews. 2017; *11*: 1700132

[158] Wang D, Jiang H, Yang H, et al. Investigation on photoexcited dynamics of IR-140 dye in ethanol by femtosecond supercontinuum-probing technique. Journal of Optics A: Pure and Applied Optics. 2002; *4*: 155–159

[159] Yu Z, Li W, Hagen J A, et al. Photoluminescence and lasing from deoxyribonucleic acid (DNA) thin films doped with sulforhodamine. Applied Optics. 2007; *46*: 1507

[160] Zhou W, Dridi M, Suh J Y, et al. Lasing action in strongly coupled plasmonic nanocavity arrays. Nature Nanotechnology. 2013; *8*: 506–511

[161] Popov E, Mashev L, Maystre D. Theoretical study of the anomalies of coated dielectric gratings. Optica Acta. 1986; *33*: 607–619

[162] Giese J A, Yoon J W, Wenner B R, Allen J W, Allen M S, Magnusson R. Guided-mode resonant coherent light absorbers. Optics Letters. 2014; *39*: 486

[163] Tamir T. Integrated optics. Integrated Optics, 1979;

[164] Bhargava R. Infrared Spectroscopic Imaging: The Next Generation. Applied Spectroscopy, Vol. 66, Issue 10, pp. 1091-1120. 2012; *66*: 1091–1120

[165] Wood R W. XLII. On a remarkable case of uneven distribution of light in a diffraction grating spectrum . The London, Edinburgh, and Dublin Philosophical Magazine and Journal of Science. 1902; *4*: 396–402

[166] Lord Rayleigh B. On the dynamical theory of gratings. Proceedings of the Royal Society of London. Series A, Containing Papers of a Mathematical and Physical Character. 1907; *79*: 399–416

[167] Fano U. The Theory of Anomalous Diffraction Gratings and of Quasi-Stationary Waves on Metallic Surfaces (Sommerfeld’s Waves). Journal of the Optical Society of America. 1941; *31*: 213

[168] Hessel A, Oliner A A. A New Theory of Wood’s Anomalies on Optical Gratings. Applied

Optics. 1965; *4*: 1275

[169] Maystre D. Sur la diffraction d'une onde plane par un reseau metallique de conductivite finie. Optics Communications. 1972; *6*: 50–54

[170] Quaranta G, Basset G, Martin O J F, Gallinet B. Recent Advances in Resonant Waveguide Gratings. Laser & Photonics Reviews. 2018; *12*: 1800017

[171] Brundrett D L, Glytsis E N, Gaylord T K. Subwavelength transmission grating retarders for use at 106 µm. Applied Optics. 1996; *35*: 6195

[172] Forestiere C, Pasquale A J, Capretti A, et al. Genetically engineered plasmonic nanoarrays. Nano Letters. 2012; *12*: 2037–2044

[173] Imran M, Hashim R, Khalid N E A. An overview of particle swarm optimization variants. in *Procedia Eng.*, Elsevier Ltd. , 2013, pp. 491–496

[174] Dakss M L, Kuhn L, Heidrich P F, Scott B A. Grating coupler for efficient excitation of optical guided waves in thin films. Applied Physics Letters. 1970; *16*: 523–525

[175] Chen Y, Halir R, Molina-Fernández Í, Cheben P, He J-J. High-efficiency apodized-imaging chip-fiber grating coupler for silicon nitride waveguides. Optics Letters. 2016; *41*: 5059

[176] Ning T, Hyvärinen O, Pietarinen H, Kaplas T, Kauranen M, Genty G. Third-harmonic UV generation in silicon nitride nanostructures. Optics Express. 2013; *21*: 2012

[177] Lee S G, Kim S H, Kim K J, Kee C S. Polarization-independent electromagnetically induced transparency-like transmission in coupled guided-mode resonance structures. Applied Physics Letters. 2017; *110*: 111106

[178] Yoon J W, Lee K J, Magnusson R. Ultra-sparse dielectric nanowire grids as wideband reflectors and polarizers. Optics Express. 2015; *23*: 28849

[179] Streshinsky M, Shi R, Novack A, et al. A compact bi-wavelength polarization splitting grating coupler fabricated in a 220 nm SOI platform. Optics Express. 2013; *21*: 31019

[180] Qian L, Zhang D, Tao C, Hong R, Zhuang S. Tunable guided-mode resonant filter with wedged waveguide layer fabricated by masked ion beam etching. Optics Letters. 2016; *41*: 982

[181] SURYS. SURYS - Hologram Industries. http://surys.com. 2021;

[182] Lu C, Lipson R H. Interference lithography: a powerful tool for fabricating periodic structures. Laser & Photonics Reviews. 2010; *4*: 568–580

[183] Vieu C, Carcenac F, Pépin A, et al. Electron beam lithography: Resolution limits and applications. Applied Surface Science. 2000; *164*: 111–117

[184] Bader M A, Kappel C, Selle A, Ihlemann J, Ng M L, Herman P R. F2-laser-machined submicrometer gratings in thin dielectric films for resonant grating waveguide applications. Applied Optics. 2006; *45*: 6586–6590

[185] Karouta F. A practical approach to reactive ion etching. Journal of Physics D: Applied Physics. 2014; *47*: 233501

[186] Kagan C R, Lifshitz E, Sargent E H, Talapin D V. Building devices from colloidal quantum dots. Science. 2016; *353*: 6302

[187] García De Arquer F P, Armin A, Meredith P, Sargent E H. Solution-processed semiconductors for next-generation photodetectors. Nature Reviews Materials. 2017; *2*: 16100

[188] Baek S, Cho J, Kim J, et al. A Colloidal-Quantum-Dot-Based Self-Charging System via the Near-Infrared Band. Advanced Materials. 2018; *30*: 1707224

[189] Karani A, Yang L, Bai S, et al. Perovskite/Colloidal Quantum Dot Tandem Solar Cells: Theoretical Modeling and Monolithic Structure. ACS Energy Letters. 2018; *3*: 869–874

[190] Ip A H, Kiani A, Kramer I J, et al. Infrared Colloidal Quantum Dot Photovoltaics via Coupling Enhancement and Agglomeration Suppression. ACS Nano. 2015; *9*: 8833–8842

[191] Kim J, Ouellette O, Voznyy O, et al. Butylamine-Catalyzed Synthesis of Nanocrystal Inks Enables Efficient Infrared CQD Solar Cells. Advanced Materials. 2018; *30*: 1803830

[192] Ouellette O, Hossain N, Sutherland B R, et al. Optical Resonance Engineering for Infrared Colloidal Quantum Dot Photovoltaics. ACS Publications. 2016; *1*: 852–857

[193] Zhang X, Öberg V A, Du J, Liu J, Johansson E M J. Extremely lightweight and ultra-flexible infrared light-converting quantum dot solar cells with high power-per-weight output using a solution-processed bending durable silver nanowire-based electrode. Energy and Environmental Science. 2018; *11*: 354–364

[194] Baek S W, Ouellette O, Jo J W, et al. Infrared Cavity-Enhanced Colloidal Quantum Dot

Photovoltaics Employing Asymmetric Multilayer Electrodes. ACS Energy Letters. 2018; *3*: 2908–2913

[195] Kawawaki T, Wang H, Kubo T, et al. Efficiency Enhancement of PbS Quantum Dot/ZnO Nanowire Bulk-Heterojunction Solar Cells by Plasmonic Silver Nanocubes. ACS Publications. 2021; *10*: 45

[196] Baek S-W, Hoon Song J, Choi W, et al. A Resonance-Shifting Hybrid n-Type Layer for Boosting Near-Infrared Response in Highly Effi cient Colloidal Quantum Dots Solar Cells. Wiley Online Library. 2015; *27*: 8102–8108

[197] Baek S W, Noh J, Lee C H, Kim B, Seo M K, Lee J Y. Plasmonic forward scattering effect in organic solar cells: A powerful optical engineering method. Scientific Reports. 2013; *3*: 1–7

[198] Kim Y, Bicanic K, Tan H, et al. Nanoimprint-Transfer-Patterned Solids Enhance Light Absorption in Colloidal Quantum Dot Solar Cells. Nano Letters. 2017; *17*: 2349–2353

[199] Ferry V E, Polman A, Atwater H A. Modeling light trapping in nanostructured solar cells. ACS Nano. 2011; *5*: 10055–10064

[200] Deceglie M G, Ferry V E, Alivisatos A P, Atwater H A, Watson T J. Design of Nanostructured Solar Cells Using Coupled Optical and Electrical Modeling. ACS Publications. 2012; *12*: 2894–2900

[201] Li X, Choy W, Huo L, Xie F, … W S-A, 2012 undefined. Dual plasmonic nanostructures for high performance inverted organic solar cells. Wiley Online Library. 2012; *24*: 3046–3052

[202] Jeong S, Cho C, Kang H, et al. Nanoimprinting-induced nanomorphological transition in polymer solar cells: Enhanced electrical and optical performance. ACS Nano. 2015; *9*: 2773–2782

[203] Wang Y, Wang P, Zhou X, et al. Diffraction-Grated Perovskite Induced Highly Efficient Solar Cells through Nanophotonic Light Trapping. Wiley Online Library. 2018; *8*: 225

[204] Liu M, Voznyy O, Sabatini R, et al. Hybrid organic-inorganic inks flatten the energy landscape in colloidal quantum dot solids. Nature Materials. 2017; *16*: 258–263

[205] Chuang C H M, Brown P R, Bulović V, Bawendi M G. Improved performance and stability

in quantum dot solar cells through band alignment engineering. Nature Materials. 2014; *13*: 796–801

[206] Huo M M, Liang R, Xing Y D, et al. Side-chain effects on the solution-phase conformations and charge photogeneration dynamics of low-bandgap copolymers. Journal of Chemical Physics. 2013; *139*: 124904

[207] Mihailetchi V D, Wildeman J, Blom P W M. Space-charge limited photocurrent. Physical Review Letters. 2005; *94*: 52

[208] Azmi R, Sinaga S, Aqoma H, et al. Highly efficient air-stable colloidal quantum dot solar cells by improved surface trap passivation. Nano Energy. 2017; *39*: 86–94

[209] Feng K, Xu X, Li Z, et al. Low band gap benzothiophene - Thienothiophene copolymers with conjugated alkylthiothieyl and alkoxycarbonyl cyanovinyl side chains for photovoltaic applications. Chemical Communications. 2015; *51*: 6290–6292

[210] Bi Y, Pradhan S, Gupta S, Akgul M Z, Stavrinadis A, Konstantatos G. Infrared Solution-Processed Quantum Dot Solar Cells Reaching External Quantum Efficiency of 80% at 1.35 µm and Jsc in Excess of 34 mA cm-2. Advanced Materials. 2018; *30*: 1704928

[211] Choi J, Jo J W, de Arquer F P G, et al. Activated Electron-Transport Layers for Infrared Quantum Dot Optoelectronics. Advanced Materials. 2018; *30*: 1801720

[212] Gong X, Tong M, Xia Y, et al. High-detectivity polymer photodetectors with spectral response from 300 nm to 1450 nm. Science. 2009; *325*: 1665–1667

[213] Wang H, Kim D H. Perovskite-based photodetectors: Materials and devices. Chemical Society Reviews. 2017; *46*: 5204–5236

[214] Bruening R J. Spectral irradiance scales based on filtered absolute silicon photodetectors. Appl. Opt. 1987; *26*: 1051–1057

[215] Canfield L R, Vest R E, Woods T N, Korde R S. Silicon photodiodes with integrated thin-film filters for selective bandpasses in the extreme ultraviolet. in *Proc.SPIE*, 1994

[216] Søndergaard R R, Hösel M, Krebs F C. Roll-to-Roll fabrication of large area functional organic materials. Journal of Polymer Science, Part B: Polymer Physics. 2013; *51*: 16–34

[217] Brabec (Linz) C, Hauch (Erlangen) E. United States. United States. 2009; 7476278 B2

[218] Tong S, Yuan J, Zhang C, et al. Large-scale roll-to-roll printed, flexible and stable organic bulk heterojunction photodetector. npj Flexible Electronics. 2018; *2*: 1–8

[219] Yokota T, Zalar P, Kaltenbrunner M, et al. Ultraflexible organic photonic skin. Science Advances. 2016; *2*: 1–9

[220] Li Y. Molecular design of photovoltaic materials for polymer solar cells: Toward suitable electronic energy levels and broad absorption. Accounts of Chemical Research. 2012; *45*: 723–733

[221] Antognazza M R, Scherf U, Monti P, Lanzani G. Organic-based tristimuli colorimeter. Applied Physics Letters. 2007; *90*: 21–24

[222] Strobel N, Droseros N, Köntges W, et al. Color-Selective Printed Organic Photodiodes for Filterless Multichannel Visible Light Communication. Advanced Materials. 2020; *32*:

[223] Dou L, Liu Y, Hong Z, Li G, Yang Y. Low-Bandgap Near-IR Conjugated Polymers/Molecules for Organic Electronics. Chemical Reviews. 2015; *115*: 12633–12665

[224] Liu X, Lin Y, Liao Y, Wu J, Zheng Y. Recent advances in organic near-infrared photodiodes. Journal of Materials Chemistry C. 2018; *6*: 3499–3513

[225] Battaglia C, Hsu C M, Söderström K, et al. Light trapping in solar cells: Can periodic beat random? ACS Nano. 2012; *6*: 2790–2797

[226] Konstantatos G, Sargent E H. Nanostructured materials for photon detection. Nature Nanotechnology. 2010; *5*: 391–400

[227] Armin A, Jansen-Van Vuuren R D, Kopidakis N, Burn P L, Meredith P. Narrowband light detection via internal quantum efficiency manipulation of organic photodiodes. Nature Communications. 2015; *6*: 6343

[228] Hoke E T, Vandewal K, Bartelt J A, et al. Recombination in polymer:Fullerene solar cells with open-circuit voltages approaching and exceeding 1.0 V. Advanced Energy Materials. 2013; *3*: 220–230

[229] Vandewal K, Tvingstedt K, Gadisa A, Inganäs O, Manca J V. On the origin of the open-circuit voltage of polymer–fullerene solar cells. Nature Materials. 2009; *8*: 904–909

[230] Deibel C, Strobel T, Dyakonov V. Role of the Charge Transfer State in Organic Donor-

Acceptor Solar Cells. Advanced Materials. 2010; *22*: 4097–4111

[231] Panda P, Veldman D, Sweelssen J, Bastiaansen J J A M, Langeveld-Voss B M W, Meskers S C J. Charge transfer absorption for π-conjugated polymers and oligomers mixed with electron acceptors. Journal of Physical Chemistry B. 2007; *111*: 5076–5081

[232] Yang C M, Tsai P Y, Horng S F, et al. Infrared photocurrent response of charge-transfer exciton in polymer bulk heterojunction. Applied Physics Letters. 2008; *92*: 7–10

[233] Chalabi H, Schoen D, Brongersma M L. Hot-electron photodetection with a plasmonic nanostripe antenna. Nano Letters. 2014; *14*: 1374–1380

[234] Li S, Xue D, Xu W, et al. Improving the photo current of the [60]PCBM/P3HT photodetector device by using wavelength-matched photonic crystals. Journal of Materials Chemistry C. 2014; *2*: 1500–1504

[235] MacEdo A G, Zanetti F, Mikowski A, et al. Improving light harvesting in polymer photodetector devices through nanoindented metal mask films. Journal of Applied Physics. 2008; *104*: 033714

[236] Baek S, Molet P, Choi M, et al. Nanostructured Back Reflectors for Efficient Colloidal Quantum-Dot Infrared Optoelectronics. Advanced Materials. 2019; 1901745

[237] Shen P, Wang G, Kang B, Guo W, Shen L. High-Efficiency and High-Color-Rendering-Index Semitransparent Polymer Solar Cells Induced by Photonic Crystals and Surface Plasmon Resonance. ACS Applied Materials and Interfaces. 2018; *10*: 6513–6520

[238] Xu L, Aumaitre C, Kervella Y, et al. Increasing the Efficiency of Organic Dye-Sensitized Solar Cells over 10.3% Using Locally Ordered Inverse Opal Nanostructures in the Photoelectrode. Advanced Functional Materials. 2018; *28*: 1706291

[239] Mariano M, Kozyreff G, Gerling L G, et al. Intermittent chaos for ergodic light trapping in a photonic fiber plate. Light: Science and Applications. 2016; *5*: e16216–e16216

[240] Yablonovitch E. Photonic Crystals. Journal of Modern Optics. 1994; *41*: 173–194

[241] Pimputkar S, Speck J S, Denbaars S P, Nakamura S. Prospects for LED lighting. Nature Photonics. 2009; *3*: 180–182

[242] Pattison P M, Tsao J Y, Brainard G C, Bugbee B. LEDs for photons, physiology and food. Nature. 2018; *563*: 493–500

[243] Sun Y, Forrest S R. Organic light emitting devices with enhanced outcoupling via microlenses fabricated by imprint lithography. Journal of Applied Physics. 2006; *100*: 073106

[244] Wrzesniewski E, Eom S H, Cao W, et al. Enhancing light extraction in top-emitting organic light-emitting devices using molded transparent polymer microlens arrays. Small. 2012; *8*: 2647–2651

[245] Oh J Y, Kim J H, Seo Y K, et al. Down-conversion light outcoupling films using imprinted microlens arrays for white organic light-emitting diodes. Dyes and Pigments. 2017; *136*: 92–96

[246] Miranda-Muñoz J M, Lozano G, Míguez H. Design and Realization of a Novel Optically Disordered Material: A Demonstration of a Mie Glass. Advanced Optical Materials. 2017; *5*: 1700025

[247] Miranda-Muñoz J M, Geng D, Calvo M E, Lozano G, Míguez H. Flexible nanophosphor films doped with Mie resonators for enhanced out-coupling of the emission. Journal of Materials Chemistry C. 2019; *7*: 267–274

[248] Koo W H, Jeong S M, Araoka F, et al. Light extraction from organic light-emitting diodes enhanced by spontaneously formed buckles. Nature Photonics. 2010; *4*: 222–226

[249] Revaux A, Dantelle G, Decanini D, et al. Photonic crystal patterning of luminescent sol-gel films for light extraction. Nanotechnology. 2011; *22*: 365701–365701

[250] Wu S, Xia H, Xu J, Sun X, Liu X. Manipulating Luminescence of Light Emitters by Photonic Crystals. Advanced Materials. 2018; *30*: 1803362

[251] Lozano G, Louwers D J, Rodríguez S R K, et al. Plasmonics for solid-state lighting: Enhanced excitation and directional emission of highly efficient light sources. Light: Science and Applications. 2013; *2*: e66–e66

[252] Sánchez-Sobrado O, Calvo M E, Núñez N, Ocaña M, Lozano G, Míguez H. Environmentally responsive nanoparticle-based luminescent optical resonators. Nanoscale. 2010; *2*: 936–941

[253] Devys L, Dantelle G, Revaux A, et al. Extraction Length Determination in Patterned Luminescent Sol-Gel Films. Advanced Optical Materials. 2014; *2*: 81–87

[254] Gorsky S, Zhang R, Gok A, et al. Directional light emission enhancement from LED-phosphor converters using dielectric Vogel spiral arrays. APL Photonics. 2018; *3*: 126103

[255] Hoang N V, Pereira A, Nguyen H S, et al. Giant Enhancement of Luminescence Down-Shifting by a Doubly Resonant Rare-Earth-Doped Photonic Metastructure. ACS Photonics. 2017; *4*: 1705–1712

[256] Geng D, Lozano G, Calvo M E, et al. Photonic Tuning of the Emission Color of Nanophosphor Films Processed at High Temperature. Advanced Optical Materials. 2017; *5*: 1700099

[257] Geng D, Cabello-Olmo E, Lozano G, Míguez H. Photonic structuring improves the colour purity of rare-earth nanophosphors. Materials Horizons. 2018; *5*: 661–667

[258] Geng D, Cabello-Olmo E, Lozano G, Míguez H. Tamm Plasmons Directionally Enhance Rare-Earth Nanophosphor Emission. ACS Photonics. 2019; *6*: 634–641

[259] Wierer J J, David A, Megens M M. III-nitride photonic-crystal light-emitting diodes with high extraction efficiency. Nature Photonics. 2009; *3*: 163–169

[260] Khaidarov E, Liu Z, Paniagua-Domínguez R, et al. Light-Emitting Diodes: Control of LED Emission with Functional Dielectric Metasurfaces (Laser Photonics Rev. 14(1)/2020). Laser & Photonics Reviews. 2020; *14*: 2070010

[261] Lee Y C, Chen H L, Lu C Y, Wu H Sen, Chou Y F, Chen S H. Using nanoimprint lithography to improve the light extraction efficiency and color rendering of dichromatic white light-emitting diodes. Nanoscale. 2015; *7*: 16312–16320

[262] Nuñez N O, Rivera S, Alcantara D, De la Fuente J M, García-Sevillano J, Ocaña M. Surface modified Eu: GdVO4 nanocrystals for optical and MRI imaging. Journal of the Chemical Society. Dalton Transactions. 2013; *42*: 10725–10734

UAB
Universitat Autònoma
de Barcelona

ICMAB